

REPORT DOCUMENTATION PAGE

AFRL-SR-AR-TR-03-

Public reporting burden for this collection of information is estimated to average 1 hour per response, including the time for reviewing instructions, searching existing data sources, gathering the data needed, and completing and reviewing this collection of information. Send comments regarding this burden estimate or any other aspect of this collection of information, including suggestions for reducing this burden to Department of Defense, Washington Headquarters Services, Directorate for Information Operations and Reports (0704-4302). Respondents should be aware that notwithstanding any other provision of law, no person shall be subject to any penalty for failing to comply with a collection of information if it does not display a valid OMB control number. PLEASE DO NOT RETURN YOUR FORM TO THE ABOVE ADDRESS.

1. REPORT DATE (DD-MM-YYYY) 10-01-2003	2. REPORT TYPE Final Technical Report	3. DATES COVERED (From - To) 5/01/00 - 10/31/02
4. TITLE AND SUBTITLE (U) Statistical Interpretation of Power Spectral Densities Measured by Picosecond Time-Resolved Laser-Induced Fluorescence in Turbulent Nonpremixed Flames		5a. CONTRACT NUMBER
		5b. GRANT NUMBER F49620-00-1-0017
		5c. PROGRAM ELEMENT NUMBER 61102F
		5d. PROJECT NUMBER 2308
		5e. TASK NUMBER BV
6. AUTHOR(S) Normand M. Laurendeau, Galen B. King, and Jay P. Gore		5f. WORK UNIT NUMBER
		8. PERFORMING ORGANIZATION REPORT NUMBER
		7. PERFORMING ORGANIZATION NAME(S) AND ADDRESS(ES) School of Mechanical Engineering Purdue University West Lafayette, IN 47907-1288
9. SPONSORING / MONITORING AGENCY NAME(S) AND ADDRESS(ES) AFOSR/NA 4015 Wilson Boulevard Room 713 Arlington, VA 22203-1954		10. SPONSOR/MONITOR'S ACRONYM(S)
		11. SPONSOR/MONITOR'S REPORT NUMBER(S)

12. DISTRIBUTION / AVAILABILITY STATEMENT
Approved for public release; distribution is unlimited.

20030305 085

13. SUPPLEMENTARY NOTES

14. ABSTRACT
Picosecond time-resolved laser-induced fluorescence (PITLIF) has been applied to time-series measurements of OH, CH, and number density in turbulent nonpremixed flames with the intention of better understanding scalar fluctuation rates. Power spectral densities and autocorrelation functions were computed from the time series and then used to calculate integral time scales for many axial and radial locations in seven jet diffusion flames. The OH autocorrelation functions were found to collapse when normalized by their integral time scales. A stochastic model based on the laminar flamelet concept was developed to predict these integral time scales. Improvements over a prior version of this model and a more systematic application to H₂/CH₄/N₂ flames permitted a reasonable prediction of the experimental trends. CH autocorrelation functions were also found to be self-similar except at locations close to the jet centerline or for Reynolds numbers approaching blowoff. Assumptions required for the time-series simulations were assessed via time-series measurements of total number density in the same flames, and the required input data were extracted by using time-averaged measurements from other research groups. Additional OH measurements in an H₂/N₂ jet flame provided the first direct comparison to integral time scales predicted from large-eddy simulations (LES). The predicted temporal scales were found to be a factor of two lower than the scalar measurements, but the LES predictions reproduced the correct shape for the OH power spectral density.

15. SUBJECT TERMS
Turbulent Nonpremixed Flames, Power Spectral Density, Scalar Time Series, Picosecond Time-Resolved Laser-Induced Fluorescence

16. SECURITY CLASSIFICATION OF:			17. LIMITATION OF ABSTRACT UL	18. NUMBER OF PAGES 91	19a. NAME OF RESPONSIBLE PERSON Julian M. Tishkoff
a. REPORT Unclassified	b. ABSTRACT Unclassified	c. THIS PAGE Unclassified			19b. TELEPHONE NUMBER (include area code) (703) 696-8478

1. Research Objectives

Quantitative measurements of radical concentrations in flames are required for an understanding of important interactions between fluid mixing and chemical reactions (Drake and Pitz, 1985). Laser-induced fluorescence (LIF) possesses both the spatial and temporal resolution necessary for monitoring radical concentrations in reacting flows (Barlow and Carter, 1994), but usually suffers from an inverse dependence on the local quenching rate coefficient. Although laser-saturated fluorescence (LSF) permits measurements of species concentrations without recourse to quenching calculations (Reisel *et al.*, 1997), the LSF technique requires large laser powers, which forces the laser repetition rate to be on the order of 10 Hz. This repetition rate can provide mean concentrations and probability density functions (PDFs), but is clearly too slow to resolve species fluctuations in turbulent flames. High repetition rate lasers, on the other hand, can be utilized for measuring turbulent species fluctuations but the quenching rate coefficient must be obtained within sampling times on the order of the Kolmogorov temporal scale.

Measurements of minor-species concentrations in turbulent flames are of interest owing to their importance in pollutant chemistry and to their use as markers of instantaneous flame structure. Hydroxyl (OH) and methylidyne (CH) measurements have been reported by many researchers in a wide variety of flames; however, most of these studies have employed high-power, low-repetition-rate, pulsed lasers. With such instrumentation, two sequential measurements are further apart in time than most correlations arising from turbulent fluctuations. Thus, the measurements are temporally independent from one shot to the next and yield only single-time statistics, including the mean, variance, and probability density function (PDF).

Time-scale information can be provided by scalar time series when repetition rates are sufficiently fast to resolve turbulent fluctuations. The optical technique employed in this research investigation, picosecond time-resolved laser-induced fluorescence (PITLIF), operates by monitoring the LIF signal using a novel four-bin, integrated photon-counting procedure. Quenching data can be recovered from the time-resolved bins and used to correct the total fluorescence signal, yielding a temporal record of quenching-independent fluctuations in species number density. From this temporal record, both power spectral densities (PSDs) and PDFs can be computed that correspond to local concentrations in the flame. The PSDs and PDFs can then be used for validation of theoretical turbulence and combustion models. The PITLIF approach has previously been demonstrated, in particular, for concentrations of CH (Renfro *et al.*, 1996) and OH (Renfro *et al.*, 1999a).

Based on this background, the primary goal of the current research project was to apply PITLIF to the measurement, interpretation, and modeling of OH and CH concentrations in turbulent nonpremixed $H_2/CH_4/N_2$ flames. Proper interpretation and modeling of these reactive scalars was aided by a stochastic simulation completed under the present program. Taken together, these measurements and simulations indicate that the laminar flamelet approximation can be used to predict scalar fluctuation rates in nonpremixed flames. An additional turbulent H_2/N_2 diffusion flame was also investigated in collaboration with researchers from Technische Universität Darmstadt. The PITLIF measurements in this flame have provided the first direct comparison to time-scale predictions from large-eddy simulations (LES). The predicted time scales are too slow by a factor of two as compared to the measurements, but other statistics such as the PSD shape are well predicted by LES. Future work is planned to exploit such comparisons for improved model development.

2. Background

2.1 Theory and Practice for PITLIF

Rate Equations

The basic PITLIF procedure for producing a quenching-independent measurement of concentration can be understood by applying the radiative rate equations to a simple two-level model. A laser pulse first excites molecules from the ground level to an excited electronic level. The initial population is as-

sumed to be entirely in the ground level before excitation and the width of the laser pulse, Δt , is assumed to be short compared to the quenching time. For sufficiently low laser power, the number density in the excited level immediately following the laser pulse, N_2^o (cm^{-3}), is given by

$$N_2^o = N_1^o \bar{W}_{12} \Delta t, \quad (1)$$

where N_1^o is the initial number density of the species of interest and \bar{W}_{12} is the average rate coefficient for stimulated absorption (s^{-1}), as computed from an integration over the exact laser pulse shape. Subsequent to the laser pulse, the population of the excited level decays to the ground level. In the absence of laser irradiation, absorption and stimulated emission can be neglected so that during the decay the number density within the excited level is given by

$$N_2(t) = N_1^o \bar{W}_{12} \Delta t \exp(-t/\tau_{\text{fl}}), \quad (2)$$

where τ_{fl} is the excited-state (or fluorescence) lifetime (s). This excited-state lifetime is given in terms of the rate coefficient for spontaneous emission, A_{21} , and that for quenching, Q_{21} , by

$$\tau_{\text{fl}} = (A_{21} + Q_{21})^{-1}. \quad (3)$$

The temporal fluorescence signal depends linearly on both the number density in the excited level and the collection volume, V_c (cm^3). Hence, the temporally resolved fluorescence decay is given by

$$S(t) = \bar{W}_{12} \Delta t A_{21} V_c N_1^o \exp(-t/\tau_{\text{fl}}), \quad (4)$$

where $S(t)$ represents the output of the PITLIF instrument in photons/second. While temporal analysis of $S(t)$ yields the fluorescence lifetime, integration gives

$$S_f = \int_0^{\infty} S(t) dt = \bar{W}_{12} \Delta t A_{21} V_c \tau_{\text{fl}} N_1^o, \quad (5)$$

which corresponds to the integrated fluorescence signal. All terms in Eq. (5) can be determined through calibration except τ_{fl} and N_1^o . For a two-level system, the excited-state lifetime can be determined from the decay represented by Eq. (4). Equation (5) can then be used to determine the initial number density corrected for electronic quenching. For a multilevel system, the total number density can be obtained from N_1^o by using the appropriate Boltzmann fraction. In either case, the integrated fluorescence signal is proportional to the concentration of target molecules in the flame.

Experimental Setup and Procedure

A diagram of the laser system, including the burner, is shown in Fig. 1. In general, the Spectra Physics Tsunami, regeneratively mode-locked, Ti:Sapphire laser was pumped by a 20-W, Spectra Physics argon-ion, multi-mode laser and provided a pulse repetition rate of 80 MHz. For OH measurements, the resulting IR beam had a temporal pulse width of 18 ps and was frequency tripled to ~ 309 nm in a CSK SuperTripler. The output beam was recollimated by two UV lenses and focused by a 22.9-cm focal length, 5.1-cm diameter UV lens to form the probe volume above the burner assembly. For the tripled beam, the beam diameter (e^{-2}) was measured at the probe volume to be ~ 71 μm . The laser power was 18-24 mW which resulted in an average probe volume irradiance of $\sim 3.5 \times 10^5$ mW/cm^2 . The $Q_1(8)$ transition of the (0,0) vibronic band (309.33 nm) of OH was chosen for excitation. This line displays an approximately $\pm 5\%$ Boltzmann fraction variation over the relevant temperature range of 1500-2250 K. For CH measurements, the IR beam had a temporal pulse width of 1.5 ps, was instead frequency doubled to 430.6 nm, and was focused to a spot size of 140 μm . The narrower temporal width resulted in a broader spectral width; thus, the laser excited ~ 10 Q-branch transitions in the (0,0) X-A vibronic band. This multi-line excitation scheme provided a temperature sensitivity of $\pm 3\%$ at 1500-2500 K.

The OH or CH fluorescence was collected at a 90-degree angle from the incident laser beam by using two 14.1-cm focal-length, 10.2-cm diameter UV lenses with a magnification of 4.1. This permitted collection of approximately 1/15 of all fluorescence photons emitted from the probe volume. The wavelength of the measured fluorescence was selected by use of a 0.25-m monochromator. An adjustable slit at the entrance to the monochromator permitted the probe volume in the flame to be limited along the beam path. The beam diameter itself defined the other two probe-volume dimensions,

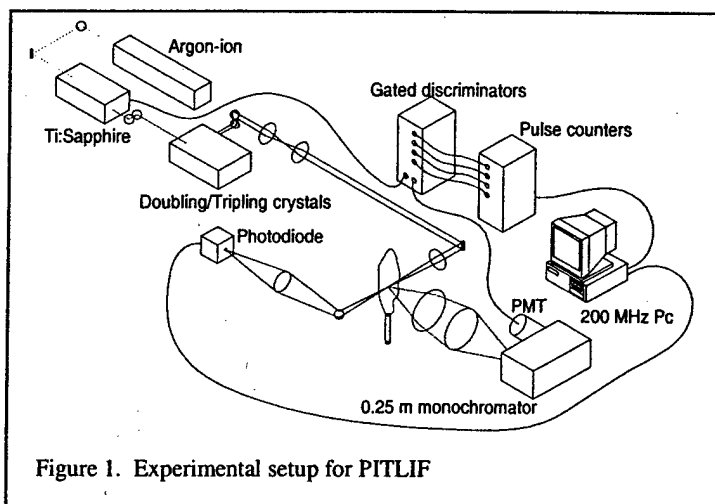


Figure 1. Experimental setup for PITLIF

although black tape on the monochromator was used to limit some flame-emission in the axial direction. These probe-volume settings were varied throughout the measurements to control the total signal level. For most measurements, the spectral window was set at a total bandwidth of 10 nm centered at 309 nm for OH or 431 nm for CH. A Hamamatsu HS5321 PMT detected the fluorescence at the exit plane of the monochromator. The PMT was biased at -2450 V to increase the single-photon pulse height for subsequent leading-edge discrimination. This PMT has a risetime of 700 ps and a transit time spread of 160 ps. Figure 2 shows representative fluorescence decays with fluorescence lifetimes (τ_f) of 1.5 and 4.0 ns, along with three areas D_2 , D_3 , and D_4 that represent three of the four measurements of the gated, photon-counting system. The remaining measurement, D_1 , which is not shown, is ungated and measures all photons; thus D_1 represents the total integrated fluorescence signal under either curve in Fig. 2.

The detailed wire schematic for the gated, photon-counting system is described by Pack *et al.* (1998). Briefly, the system consists of two LeCroy model 4608C, eight-channel discriminators connected to four EG&G Ortec logic-pulse counting boards. Several channels on the first discriminator are used to convert each PMT pulse into four logic (NIM) pulses. The second discriminator gates three of the four NIM pulses (D_2 - D_4) from the first discriminator using a photodiode output from the Ti:Sapphire cavity. Separate cable delays for each of the three PMT inputs to the second discriminator ensure that each gate passes the appropriate portion of the fluorescence decay. The ungated PMT-NIM pulse from the first discriminator and the three outputs from the gated discriminator are separately counted by the four EG&G pulse counters shown schematically in Fig. 1. These comprise the measured bins D_2 - D_4 of Fig. 2 and the integrated measurement D_1 . The four photon-counting boards each have an 8192 channel memory and can be sampled simultaneously. Each channel acquires counts over many thousands of laser pulses as set in software. The maximum sampling rate (channel advance rate) for the boards is 500 kHz, well above that needed for turbulence studies.

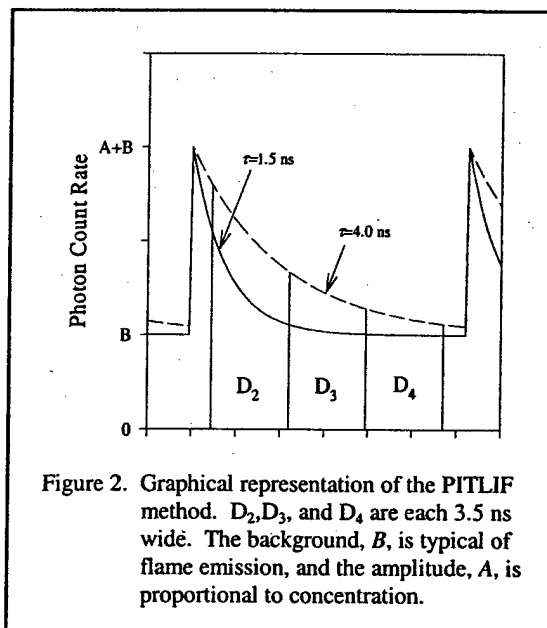


Figure 2. Graphical representation of the PITLIF method. D_2 , D_3 , and D_4 are each 3.5 ns wide. The background, B , is typical of flame emission, and the amplitude, A , is proportional to concentration.

The fluorescence lifetime, τ_f , and the flame-emission background, B , can be found from the gated counts using the expressions (Pack *et al.*, 1998)

$$\tau_n = \frac{\Delta t}{\ln[(D_2 - D_3)/(D_3 - D_4)]} \quad (6)$$

$$B = \frac{D_2 C^2 - D_4}{\Delta t (C^2 - 1)}, \quad (7)$$

where Δt is the width of each integrated bin (3.5 ns) and $C = \exp(-\Delta t/\tau_n)$. Following Eq. (4), the concentration of the excited state immediately following the laser pulse is proportional to the amplitude of the exponential decay, A , shown in Fig. 2, and can be determined from

$$A = \frac{D_2 - D_4}{\exp(-t_0/\tau_n)(1 - C^2)(1 - C)\tau_n}, \quad (8)$$

where t_0 is the delay between the laser pulse and the start of bin D_2 . This amplitude is also directly proportional to the concentration of the ground state, following Eq. (1), which in turn is directly proportional to the total number density of the molecule of interest multiplied by a temperature-dependent Boltzmann fraction. Since the excitation wavelength can be chosen to experimentally minimize the variation of the Boltzmann fraction with temperature, A in Eq. (8) can usually be taken as proportional to the species number density.

The applicability of PITLIF was first demonstrated for quantitative hydroxyl measurements in laminar premixed and opposed non-premixed flames at sampling rates below 500 Hz (Pack *et al.*, 1998). However, at the higher sampling rates needed for turbulent flames, corrections owing to photon pulse-pileup are required for Eqs. (6-8). The requisite procedure was developed by Renfro *et al.* (1999b), and has been shown to provide reliable fluorescence decay amplitudes, lifetimes, and backgrounds at data collection rates up to 35 million photoelectrons per second. For the Ti:Sapphire laser system, this collection rate represents an average of almost one detected photon per two laser pulses.

The correction procedure accounting for photon pulse-pileup is based on the following scenario. Upon receiving an analog pulse which meets the threshold criterion, the discriminator begins to output a NIM logic pulse (0 to -0.8 V, typically less than 5 ns duration, with ~1 ns rise and fall times). However, if a second acceptable analog pulse arrives during the time required to complete the NIM pulse output, the discriminator is unable to respond (or is dead) and the measured count rate will be lower than the actual incoming pulse rate. For the LeCroy discriminators, the dual-pulse resolution (DPR) is 6.5 ns based on our measurements. Fortunately, the output pulse rate is directly related to the input pulse rate; hence, a one-to-one relationship can be derived such that the measured output rate can be used to infer the actual input rate.

The resulting iterative procedure, termed "saturate-and-compare," is similar to convolute-and-compare routines that are commonly used to evaluate instrumentation response functions for accurate

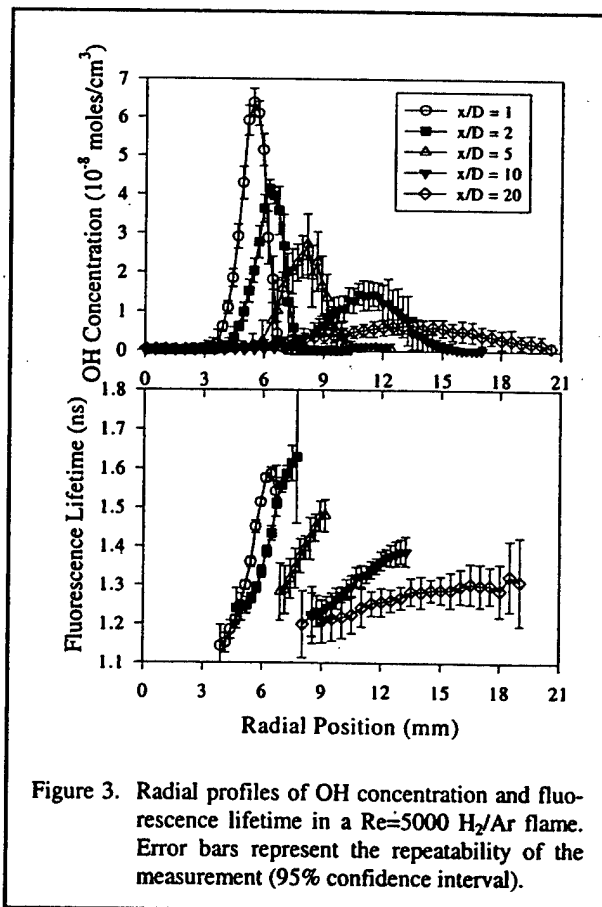


Figure 3. Radial profiles of OH concentration and fluorescence lifetime in a $Re=5000$ H_2/Ar flame. Error bars represent the repeatability of the measurement (95% confidence interval).

determinations of fluorescence lifetimes (Renfro *et al.*, 1999b). The general procedure is as follows: (1) assume values for the decay parameters (τ_f , B , and A); (2) simulate a perfect decay; (3) saturate the decay based on the observed behavior of the PITLEIF system; (4) compute the simulated bin counts, D_2 - D_4 ; and (5) compare the simulated and measured counts, eventually converging to the correct decay parameters. While the full mathematical procedure is described by Renfro *et al.* (1999b), the general scheme is based on simply fitting measured photoelectron count rates to a saturated exponential array to represent the fluorescence decay.

2.2 Previous PITLEIF Time-Series Measurements

The first quantitative time-series measurements in turbulent flames were obtained with previous AFOSR support for a series of H_2 /Ar/air jet diffusion flames (Renfro *et al.*, 1999a). Time-series measurements of OH concentrations were made at five axial locations in five Ar-diluted, H_2 /air nonpremixed flames ($[Ar]/[H_2]=0.282$). The Reynolds numbers based on room-temperature exit conditions for the 5.5-mm diameter burner were 2800, 5000, 9000, 13,000, and 17,000. At each height, measurements were made at many radial positions across the peak [OH] location. These fluorescence and lifetime time-series measurements were taken at a sampling rate of 4 kHz.

Figure 3 shows the measured radial profiles of [OH] and fluorescence lifetime in the $Re=5000$, H_2 /Ar diffusion flame. In these flames, the lifetime is determined almost exclusively by the local temperature and water concentration. The lifetime changes from the air side to the fuel side of the [OH] peak low in the flame are due mostly to changes in water concentration across the OH peak. Higher in the flame, little change occurs in the lifetime over the spatial range where substantial OH is found. At these downstream locations, the temperature and water concentration change more gradually with distance from the flame centerline, leading to the observed lifetime trends. For the mean [OH] measurements, the lifetime correction is significant as the average lifetime at $x/D=2$ is 12% higher than that at $x/D=20$ and the maximum lifetime in the flame is 43% higher than the minimum lifetime.

Figure 4 shows a comparison of concentration PSDs (corrected for lifetime) to uncorrected fluorescence PSDs in the $Re=13,000$ H_2 /Ar flame. There is no difference in the concentration and fluorescence PSDs, indicating that the lifetime measurements are relatively unimportant to accurate frequency information from the concentration fluctuations. Each measurement location in every H_2 /Ar flame was examined and each showed a similar comparison as that of Fig. 4. This independence can arise if the statistical weight of the lifetime fluctuations is small, so that concentration fluctuations dominate the fluorescence time series. For OH measurements, the local gradient of the lifetime profile (Fig. 3) is much less than that of the concentration profile. Thus, as fluctuations cause the probe volume to sample different portions of the radial [OH] distribution, the concentration time series will contain more intense fluctuations than the lifetime time series. The measured fluorescence time series will then reflect these stronger concentration fluctuations. At each location for which this comparison has been verified, the fluorescence PSD can be interpreted directly as a concentration PSD with significant improvements in signal-to-noise ratios and usable bandwidth in the PSD (Renfro *et al.*, 1999).

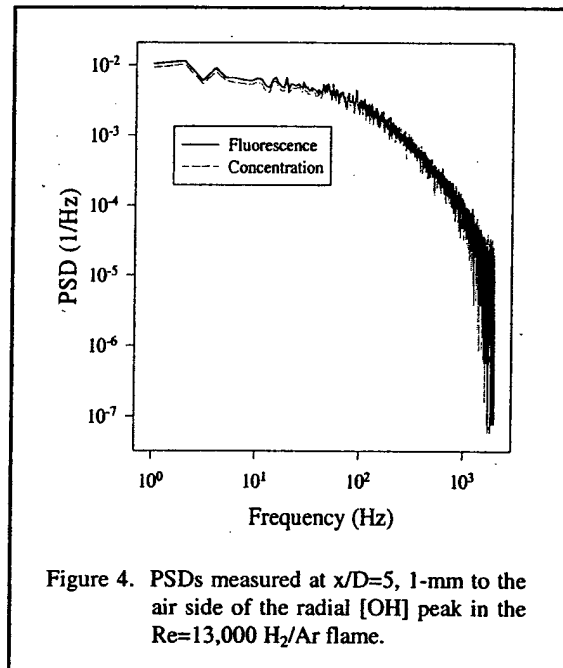


Figure 4. PSDs measured at $x/D=5$, 1-mm to the air side of the radial [OH] peak in the $Re=13,000$ H_2 /Ar flame.

Figure 5 shows the measured PSDs as a function of Reynolds number in each of the $H_2/Ar/air$ flames. The relative energy in the PSDs at low frequencies decreases as the Reynolds number increases. Likewise, the relative energy at high frequencies increases and the high-frequency slope becomes less steep. This evolution versus Reynolds number is apparent at each axial height and radial location. The variation in the PSDs can be characterized by computing the integral time scale of each spectrum. An initial examination of this variation indicated that the OH time scales varied as approximately $1/Re$ (Renfro *et al.*, 2000a). However, with only five flames, the actual dependence on Re could not be determined accurately. The most important observation from these initial measurements is that the PSDs collapse to a single curve when normalized by the local integral time scale, as shown in Fig. 6. This collapse indicates that the variation in shape of the PSD in Fig. 5 is an artifact of only the change in integral time scale (fluctuation rate) as a function of Re . Integral time scale variations were also observed for OH as a function of radial and axial positions within each jet flame, but a thorough characterization or understanding of these variations was not completed owing to the limited range of measurements.

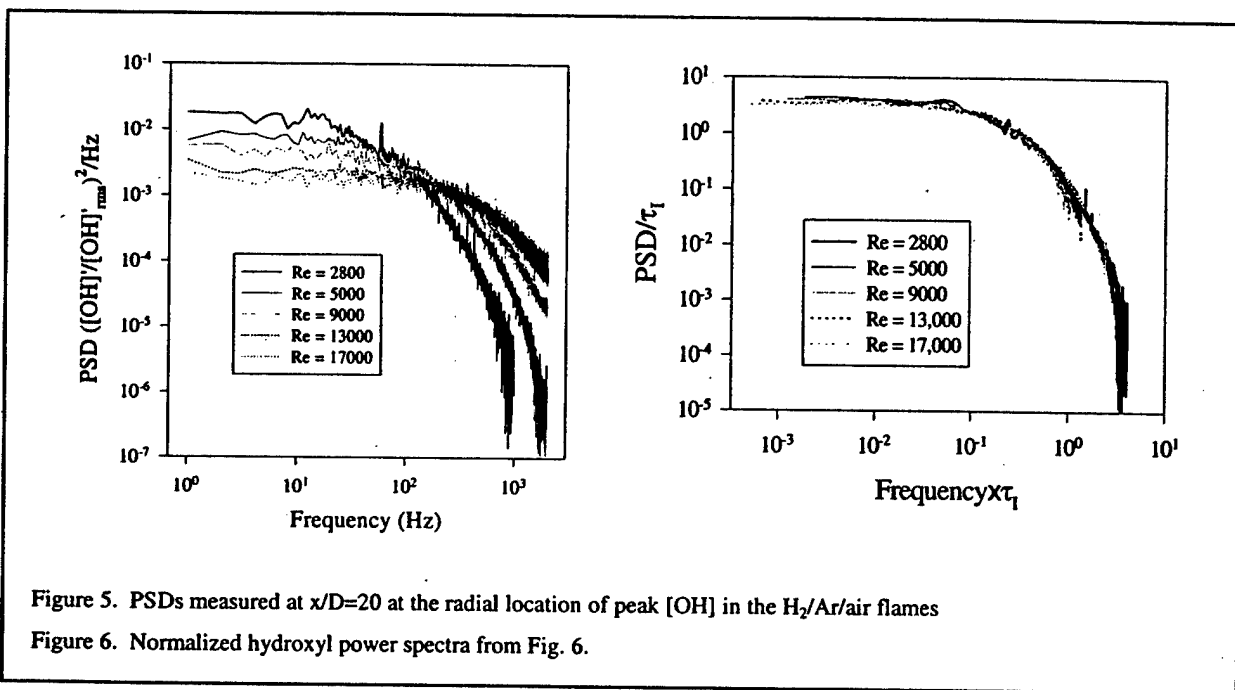


Figure 5. PSDs measured at $x/D=20$ at the radial location of peak [OH] in the $H_2/Ar/air$ flames

Figure 6. Normalized hydroxyl power spectra from Fig. 6.

3. Research Accomplishments

As summarized in Section 2, previous work for AFOSR has produced a working PITLIF instrument and provided the first application of PITLIF to turbulent flames. The following observations can be made from these initial measurements:

- (1) Fluorescence lifetime fluctuations are an insignificant portion of the total fluorescence signal. Hence, the fluorescence statistics can be taken to represent species concentration statistics with negligible error but improved signal-to-noise ratios.
- (2) Variations in the autocorrelation functions and PSDs throughout the flame studies are well characterized by the integral time scale.
- (3) Significant variations in the PSD, integral time scale, and PDF are observed as a function of Reynolds number, axial height, and radial location within each jet flame. However, a physical interpretation for these variations is incomplete owing to the limited data set available.

Based on these observations, the objectives of the present research program were to apply PITLIF to multiple species in a large set of nonpremixed jet flames and to provide a clearer physical understanding of the accompanying scalar fluctuations. The specific jet flames were chosen to take advantage of a

large available database of major-species concentration, mixture fraction, velocity and temperature. The analysis and interpretation of the PTLIF measurements was thus guided by comparisons among the measured species and by simplified time-series simulations developed with an improved use of known mixture-fraction statistics.

3.1 Time-Series Measurements of OH and CH in Turbulent Nonpremixed Flames

Detailed OH and CH measurements were made in seven jet diffusion flames with a fuel composition of 33.2% H₂, 22.1% CH₄, and 44.7% N₂ (by volume). The fuel issued from a circular nozzle into still air with cold-flow Reynolds numbers ranging from 2800 to 15,200. Two burners were examined having diameters of 3.4 and 7.8 mm. The seven flames studied are designated A1-A5 and D1-D2, as shown in Table 1. Radial profiles of time-averaged [OH] were obtained at $x/D=1, 2, 5, 10, 20, 40,$ and 60 in each 3.4-mm flame and at $x/D=1, 2, 5, 10,$ and 20 for each 7.8-mm flame. Radial profiles of time-averaged [CH] were only obtained at $x/D=1, 2, 5,$ and 10 in both the 3.4-mm and 7.8-mm burners owing to the reduced fluorescence signal. These concentration profiles, including the CH and OH profile widths and peak values, are available in Renfro *et al.* (2000b) and Renfro *et al.* (2000c), respectively. At each height, time-series measurements were also obtained for three radial locations near the [CH] and [OH] peaks at sampling rates of 10-40 kHz, as given in Table 1. Fifty time series of 4096 points each were collected to obtain clean statistics at each measurement location. PDFs, PSDs, autocorrelation functions, and integral time scales were computed from these time series, including corrections for any measured contribution of shot noise (Renfro *et al.*, 1999a).

Table 1. Burner diameter (D), average velocity (\bar{V}), cold-flow Reynolds number, and time-series sampling rate (SR) for H₂/CH₄/N₂ jet diffusion flames.

Flame	D (mm)	\bar{V} (m/s)	Re	OH SR (Hz)	CH SR (Hz)
A1	3.4	16.3	2800	10,000	10,000
A2	3.4	29.0	5000	12,500	20,000
A3	3.4	52.3	9000	20,000	20,000
A4	3.4	75.5	13,000	27,027	30,303
A5	3.4	88.3	15,200	31,250	40,000
D1	7.8	22.8	9000	10,000	20,000
D2	7.8	38.5	15,200	20,000	30,303

Sample OH time series for flames A1, A3, and A5 are shown in Fig. 7 (Renfro *et al.*, 2000c). These measurements represent the first 20 ms of data collected at the radial location of peak [OH] at $x/D=20$. A range of fluctuation time scales is present at each location in the flow, and the fluctuation rates depend strongly on Re. In each flame, the OH concentration often becomes zero as the OH layer fluctuates completely away from the fixed laser beam. These intermittent periods are typically longer in flame A1 than in flame A5. Likewise, periods for which measurable OH exists in the probe volume ([OH]>0) display a longer duration at lower Re.

The fluctuation rate variations are quantifiable in terms of autocorrelation functions, ρ_{OH} , which are plotted for the radial location of peak [OH] in Fig. 8a at two heights in each of the seven flames. The autocorrelation functions for flames at higher Reynolds numbers decay much faster than for those at lower Re. This result is a manifestation of the faster fluctuations observed at greater Re in the time traces of Fig. 7, and represents the same information as apparent from the PSDs of OH in Fig. 5. Figure 8(b) shows the autocorrelation functions of Fig. 8(a) normalized by their respective integral time scales, as obtained via integration of ρ_{OH} (Renfro *et al.*, 2000a). The normalized autocorrelation functions collapse to essentially a single curve. Since the PSD and autocorrelation function constitute a Fourier transform pair, this collapse is observed equally in the frequency domain, as shown by the H₂/Ar/air measurements of Fig. 6. This demonstrated collapse of two-time statistics implies that the distribution of fluctuation rates is independent of location within the flow. Hence, the integral time scale is a good representation of temporal variations in [OH].

CH autocorrelation functions measured on the air-side of the [CH] peak are also nearly exponential and similarly depend strongly on Re (Renfro *et al.*, 2000b). Therefore, normalization by the integral time scale again successfully collapses the statistics. However, the shapes of the autocorrelation func-

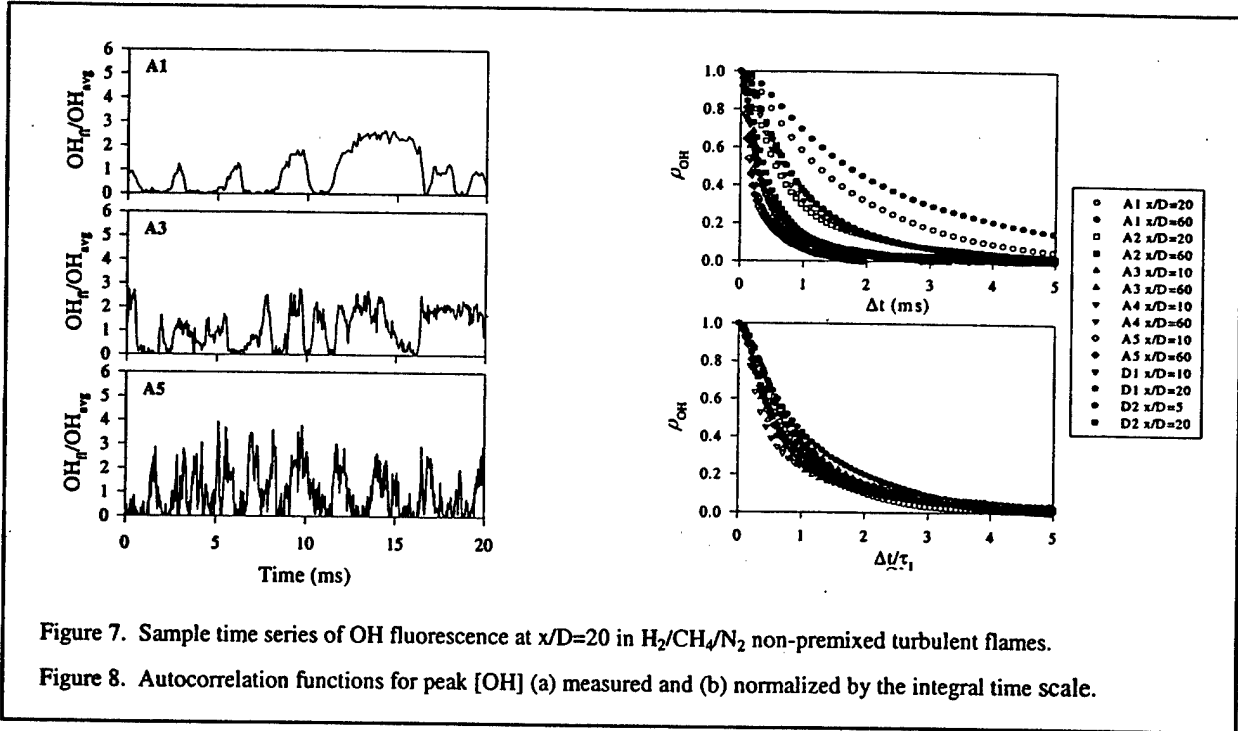


Figure 7. Sample time series of OH fluorescence at $x/D=20$ in $H_2/CH_4/N_2$ non-premixed turbulent flames.

Figure 8. Autocorrelation functions for peak [OH] (a) measured and (b) normalized by the integral time scale.

tions on the fuel-side are notably different from those on the air-side. Figure 9 shows CH autocorrelation functions about 0.1 mm to the fuel-side of the [CH] peak at $x/D=5$ for each of the flames from the 3.4-mm burner. Measurements at the [CH] peak essentially replicate these fuel-side measurements. For small time delays (high frequencies), the fuel-side CH autocorrelation functions are nearly exponential; however, a significant positive correlation exists for very large time delays (low frequencies). This difference in autocorrelation functions for large time delays can be equivalently observed as a low-frequency difference in slope for the associated PSDs (Renfro *et al.*, 2000b).

The CH autocorrelation functions on the fuel side are indicative of fluctuations with a second and longer time scale as compared to those on the air side. Since the CH time series are highly intermittent

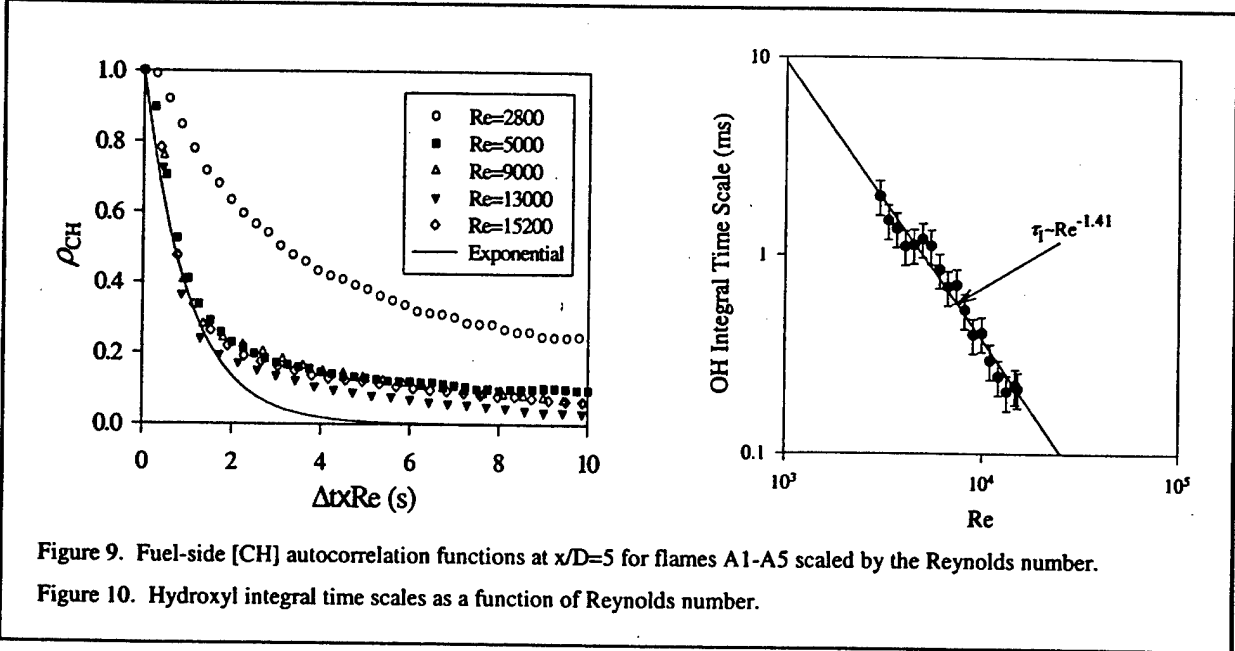


Figure 9. Fuel-side [CH] autocorrelation functions at $x/D=5$ for flames A1-A5 scaled by the Reynolds number.

Figure 10. Hydroxyl integral time scales as a function of Reynolds number.

(much more so than for OH), the corresponding autocorrelation functions are quite sensitive to the rates of flame-front fluctuations across the fixed laser beam. However, this observation also applies to the OH measurements, for which we observe no such extended autocorrelation functions. The difference may be related to the fact that the CH radical exists farther into the fuel stream than does OH (Renfro *et al.*, 2000b; Renfro *et al.*, 2000c), and thus lies closer to the shear layer and the associated region of intense mixture-fraction fluctuations.

The self-similarity of the OH and CH PSDs and their autocorrelation functions is only valid sufficiently far downstream of the jet exit. Note that data for $x/D=1$ and $x/D=2$ (and for larger heights at lower Re) are not included in Fig. 8. At $x/D=2$, the CH and OH fluctuations remain correlated for long periods of time ($\Delta t > 50$ ms), especially when compared to the downstream data which become uncorrelated for $\Delta t > 10$ ms even at the lowest Re (Renfro *et al.*, 2000c). Hence, the fluctuations at $x/D=2$ are much slower (lower frequencies) than those incorporated into Fig. 8. This same trend is apparent in the CH measurements of Fig. 9 at Re=2800. These features are consistent with images of the reaction zone in the near field of jet diffusion flames, which often display highly laminarized flame sheets (Clemens and Paul, 1995).

Because of the statistical collapse of most of the PSDs, the task of describing fluctuations throughout the various jet flames is reduced to describing only the integral time scales. Simple eddy-turn-over time scaling predicts an integral time scale variation of

$$\tau_i \sim \left(\frac{1}{\text{Re}} \right) \left(\frac{x}{D} \right)^2 \left(1 + (0.644r/r_{1/2})^2 \right)^2 \quad (9)$$

(Renfro *et al.*, 2000c). To examine Eq. (9) in more detail, a series of OH measurements at $r/x=0.075$ and $x/D=20$ was obtained in 18 flames at Re=2980-15,200. The resulting integral time scales are shown in Fig. 10, where $\tau_i \sim \text{Re}^{-1.41 \pm 0.15}$ at the 95% confidence interval. For other OH and CH data (Renfro *et al.*, 2000a; Renfro *et al.*, 2000b), the integral time scale also appears to decrease faster than $\text{Re}^{-1.0}$, although in many cases the uncertainty does not preclude the relationship of Eq. (9). This stronger dependence on Re may arise because the virtual origin (and its dependence on Re) has been neglected, as an asymptotic approach toward $\text{Re}^{-1.0}$ is observed with increasing height in the flames.

If all of the OH data from flames A1-A5 are normalized to account for the observed dependence on Reynolds number, the results are found to be consistent with the radial scaling of Eq. (9). However, only three radial measurements were initially obtained at each axial height. As a more stringent test, a series of integral time scale measurements were made at 12 radial locations for axial heights of $x/D=10, 20, 40,$ and 60 in Flame A3. These measurements (Renfro *et al.*, 2000c) show a much more complicated profile shape than predicted by Eq. (9). Moreover, the axial scaling of the OH time scales is much closer to $x^{0.5}$ than to x^2 . Therefore, simple eddy-turn-over-time scaling does not appear to be sufficient for the integral time scales of reactive scalars. Such features can be explained more thoroughly through the development of time-series simulations.

3.2 Analysis of Radical Statistics Using an Assumed-PSD Model

In this section, a stochastic assumed-PSD model developed during the previous AFOSR work, and refined during the present grant period, is discussed as a method for understanding radical statistics in turbulent nonpremixed flames (Renfro *et al.*, 2002). This assumed-PSD model is analogous to assumed-autocorrelation models, as developed, for example, by Faeth *et al.* (1991), Kounalakis *et al.* (1991), and Sivathanu *et al.* (1991). Mixture fraction time series are simulated by assuming a normalized PSD shape and forcing a random time series to reproduce this statistic. Previous efforts employed a flat PSD shape up to a knee frequency of 100 Hz and a power-law region with a slope of -2.0 above this frequency (Renfro *et al.*, 1999c). This shape is similar to those observed for velocity, temperature and hydroxyl in turbulent nonpremixed flames. The value of the PSD at each frequency is related to the amplitude of the time-series fluctuations at that frequency. Using this approach, no specification was required for the in-

tegral time scale and the PDF remained Gaussian for all simulations.

The revised approach was to assume values for certain critical mixture-fraction (Z) statistics and to construct a realistic time series replicating all of these statistics. The PDF, PSD, and integral time scale were chosen as the important statistics since considerable information is available about their shapes. With this approach, a synthetic Z time series has the correct frequency content and the correct range of instantaneous values. A simulated mixture fraction time series was constructed using

$$Z(t_i) = \bar{Z} + \mathcal{S}^{-1} \left\{ \sqrt{Z^2 \tau_{1,z} PSD_z(f_i \tau_{1,z})} \times e^{i\phi(f_i)} \right\}, \quad (10)$$

where the mean and rms values are taken from curve fits to the data of Meier *et al.* (2000) in similar flames, and the PSD shape is computed from an exponential autocorrelation function (which is similar to the observed OH PSDs). The phase spectrum is computed randomly and the integral time scale for mixture fraction, $\tau_{1,z}$, is computed from the jet momentum half-width divided by the local velocity (taken from the data of Schneider *et al.*, 2000). This simulated time series inherently produces a near Gaussian PDF; thus, the time series of Eq. (10) must be mapped to the chosen PDF_z . This map affects the shape of the PSD; thus, an iterative procedure was developed to simultaneously specify both the PDF and PSD shapes for Z . For comparison to OH and CH data, the synthetic Z time series were mapped by using a one dimensional flamelet state relationship, constructed using OPPDIF (Lutz *et al.*, 1996) with GRI-2.11 chemistry (Bowman *et al.*, 1995). The resulting scalar time series could then be used to compute the mean, rms, PSD, PDF, and τ_1 for OH, CH, or number density. More complete details of this simulation are available from Renfro *et al.* (2002).

Sample simulated time series for Z and OH are shown in Fig. 11, as simulated for $r/x=0.1$ at $x/D=20$ in flame A3. An exponential autocorrelation function and a Beta PDF are used for all of these simulations. Two reference lines on the Z time series show the limits ($Z=0.06-0.20$) beyond which negli-

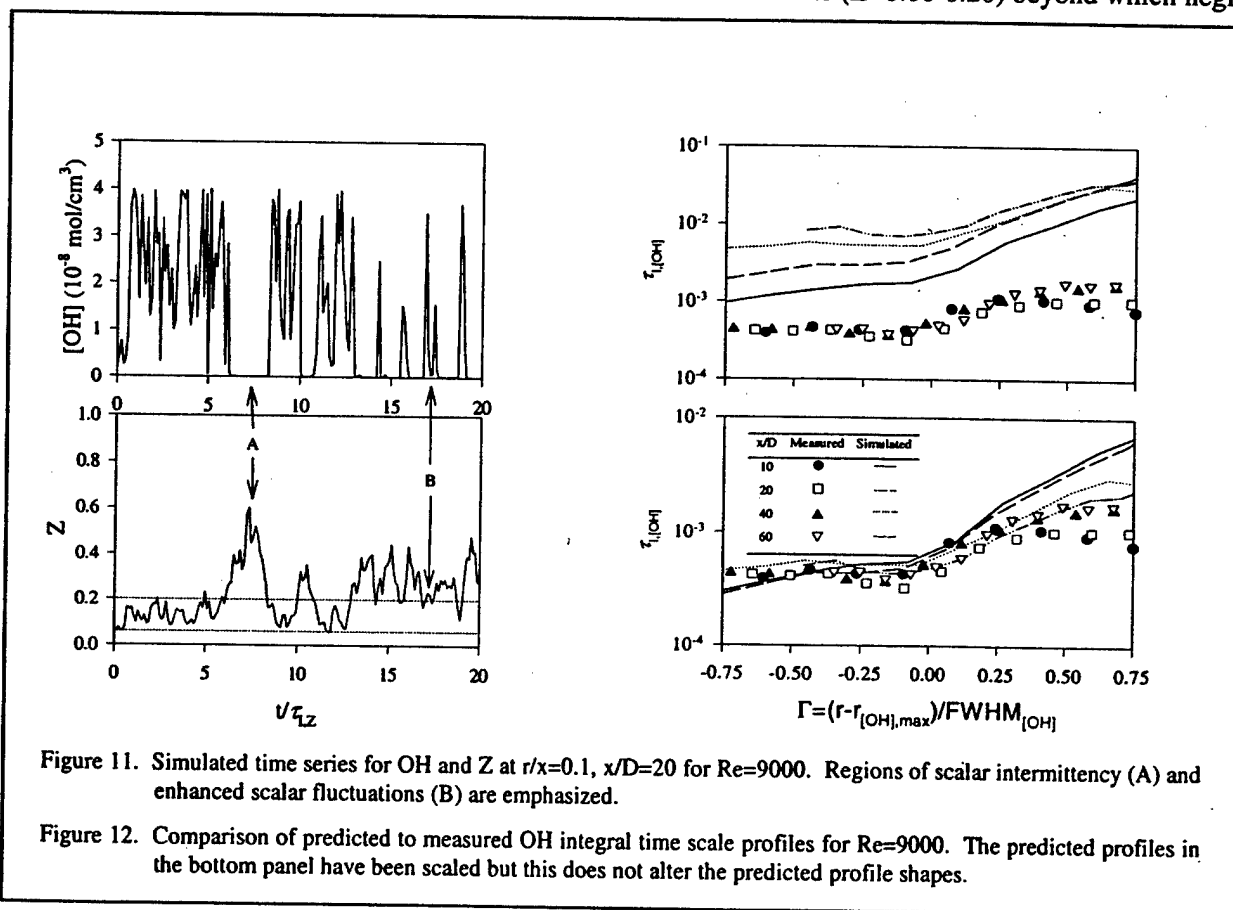


Figure 11. Simulated time series for OH and Z at $r/x=0.1$, $x/D=20$ for $Re=9000$. Regions of scalar intermittency (A) and enhanced scalar fluctuations (B) are emphasized.

Figure 12. Comparison of predicted to measured OH integral time scale profiles for $Re=9000$. The predicted profiles in the bottom panel have been scaled but this does not alter the predicted profile shapes.

gible OH exists, based on the OH state relationship. This limited range causes several important differences between the Z and OH time series. For example, the Z time series contains fluctuations outside the range $Z=0.06-0.20$ that are completely nonexistent in the scalar time series (region A). In contrast, region B shows a location where very small deviations in Z are amplified in the OH time series because they occur near the edge of the OH distribution. Hence, the spectral content of the OH distribution differs considerably from that of the Z distribution. As a result, the integral time scale will generally be much less for a more narrowly distributed scalar such as OH.

Figure 12 shows a comparison of measured and simulated OH integral time scales at each of four axial heights for flame A3. The simulations in the top graph employed convective scaling via Eq. (9) to determine the mixture fraction time scales. Quantitative agreement between the simulations and measurements cannot be achieved because there is no basis for an *a priori* selection of the proportionality constant in this scaling relationship. However, since the simulated time scales depend linearly on the input time scales for mixture fraction (as discussed by Renfro *et al.*, 2002), the shapes of the profiles are a true test of the predictions. This feature is accentuated in the bottom graph of Fig. 12, where the profiles have been divided by a constant to improve quantitative agreement with no effect on the profile shapes. In general, the simulation does a good job of replicating the shape of the radial τ_i profiles. The nearly flat time-scale profile for $\Gamma < 0$ (fuel-side of the OH peak) is surprising since the Z time scales decrease by a factor of two or more over this same range. Nevertheless, the laminar-flamelet approximation captures this experimental trend with reasonable accuracy. However, the simulation does not capture the axial change in time scales. The measurements show that the integral time scales at the [OH] peak and on the fuel-side of the peak are invariant with axial height, whereas the simulation follows typical convective scaling as observed in the top graph of Fig. 12.

Since the simulation effectively predicts the radial profile of the OH time scale in normalized coordinates, a reasonable extension of this technique is to extrapolate mixture-fraction temporal statistics from measured OH data. An estimate for the mixture-fraction time scale was determined by dividing the measured OH and CH time scales by the predicted ratio, $\tau_i/\tau_{i,Z}$, at each measured data point. The extrapolated mixture-fraction time scales are shown in Fig. 13 for heights $x/D=20, 40,$ and 60 . For comparison, the OH and CH data are accompanied by similar total number density (ND) measurements, as obtained via Rayleigh scattering (Lakshmanarao, 1999).

The number density and hydroxyl estimates for the Z time scales are independent estimates, and at each height the two calculations are nearly identical (with the exception of one point at $x/D=40$). A similar independent estimate taken from the CH data is displayed for $x/D=20$, and this value is also close to the other calculations (CH data could not be collected at large x/D). A comparison of the three estimates for $\tau_{i,Z}$ cannot be made at all locations because of errors caused by entrainment of particles from room air for the Rayleigh scattering technique (Lakshmanarao, 1999), and because the PSDs for CH at some locations are not represented by a single time scale (Renfro *et al.*, 2000b).

For flame A3, the number density is well described by the laminar flamelet approximation, so the

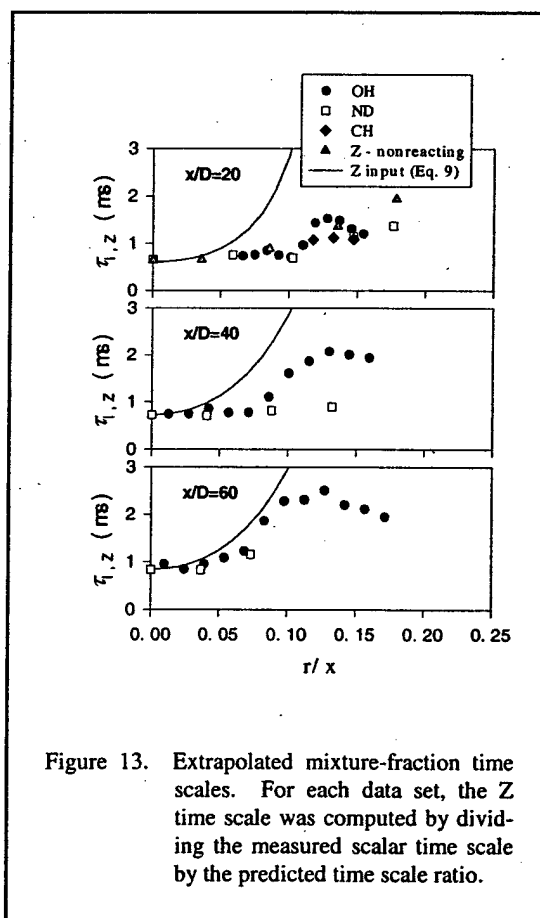


Figure 13. Extrapolated mixture-fraction time scales. For each data set, the Z time scale was computed by dividing the measured scalar time scale by the predicted time scale ratio.

above simulation should yield the true Z time scale. Figure 13 also shows the convective time scales when using the measured velocity profile. Notice that the extrapolated mixture fraction profile is much shallower. Moreover, there is almost no discernable change of $\tau_{1,Z}$ with x/D for these conditions. Hence, we find that for jets with heat release, the time scale cannot be simply computed as the jet width divided by local velocity.

3.3 Application of PITLIF to LES Validation

Many turbulence models do not recover information that can be directly compared to PITLIF data. For example, traditional Reynolds-averaged models purposefully filter all temporal fluctuations to provide a tractable calculation. The utility of PITLIF data for improving these models is problematic. On the other hand, newer models can provide predictions of time-correlation statistics. In particular, large-eddy simulations filter fluctuations below a certain temporal and spatial scale but directly model large-scale fluctuations. As the PSD is dominated by large-scale phenomena, its shape can be predicted by LES. Hence, a direct comparison between LES predictions and PITLIF measurements offers a unique opportunity to assess the limiting assumptions regarding sub-grid-scale models for LES and to provide new insights into interpreting PITLIF data.

For this purpose, additional OH time series were obtained in the so-called "H3" turbulent diffusion flame discussed by Meier *et al.* (1996). Briefly, the H3 configuration employs an 8-mm diameter fuel-jet surrounded by a contoured air co-flow to provide a uniform velocity inlet condition. The flame of interest burns a 50% H_2 , 50% N_2 (by volume) mixture at a Reynolds number of 10,000. Previous experimental work at TU-Darmstadt and DLR-Stuttgart has examined the velocity (Pfuderer *et al.*, 1996), major-species, OH, and NO concentrations (Meier *et al.*, 1996; Neuber *et al.*, 1998) throughout this flame and also for other similar flames with different Reynolds numbers or nitrogen-dilution levels. However, before our measurements, no reactive-scalar, time-scale statistics existed for these flames. On the other hand, LES has been applied to the H3 flame by Janicka (2000).

Radial profiles of time-averaged [OH] were obtained at $x/D=10-40$ in the H3 flame by using a sampling rate of 10 Hz and an averaging time of five seconds. At each of four heights, time-series measurements were obtained at a sampling rate of 12 kHz. Fifty time series of 4096 points each were collected to obtain clean statistics at all measurement locations. Time-series measurements were also obtained at the burner centerline for an axial range $x/D = 20-40$. PDFs, PSDs, autocorrelation functions, and integral time scales were computed from these time series in the same manner as reported by Renfro *et al.* (2000c).

In general, the following results were obtained from these experiments.

- The time-averaged OH concentrations are nearly Gaussian functions of the radial coordinate. The only parameters necessary to specify the full profile shape are the peak OH concentration, the radial location corresponding to the peak concentration, and the profile FWHM. This behavior is identical to that of our previous work in $H_2/CH_4/N_2$ flames (Renfro *et al.*, 2000c).
- The autocorrelation functions (or the PSDs) collapse to a single curve for most measurement locations when appropriately normalized by the integral time scale. This result implies that the relative distribution of OH time scales at a single point in the flame is independent of Reynolds number, axial height, or radial location. The scalar fluctuations are thus accurately characterized by just the integral time scale. These collapsed statistics are consistent with our previous OH measurements in H_2/Ar (Renfro *et al.*, 1999b) and $H_2/CH_4/N_2$ (Renfro *et al.*, 2000c) flames. A typical comparison for these autocorrelation functions is shown in Fig. 14.
- Hydroxyl measurements along the jet centerline display a slowly decreasing integral time scale with a minimum at $x/D = 34$, followed by a sharp increase farther downstream. Our previous measurements in non-premixed flames did not contain a sufficient number of axial heights or locations above the flame tip to observe this trend. Thus, we do not know presently if this feature is universal to non-premixed flames or is an artifact of this particular fuel and geometry.

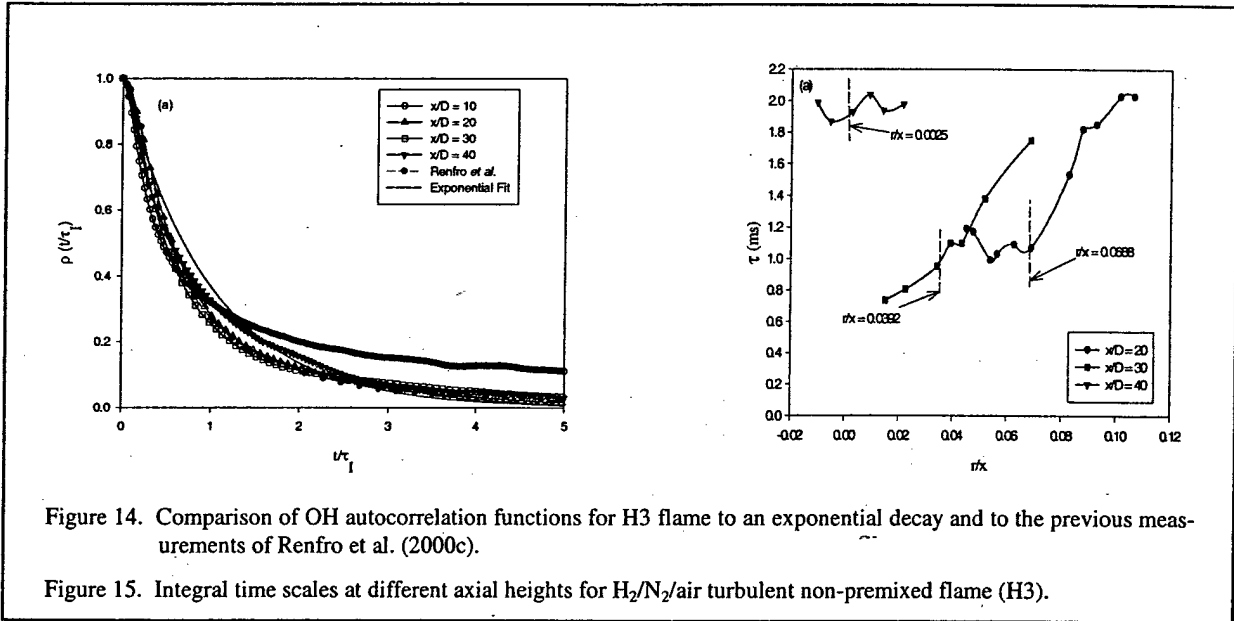


Figure 14. Comparison of OH autocorrelation functions for H3 flame to an exponential decay and to the previous measurements of Renfro *et al.* (2000c).

Figure 15. Integral time scales at different axial heights for H_2/N_2 /air turbulent non-premixed flame (H3).

The most important and unique result from this study concerns the behavior of the measured integral time scales for the hydroxyl radical. Figure 15 shows integral time scales as a function of radial location (r/x) for three different axial heights in the H3 flame. For these heights, the time scales range from 0.7 to 2.1 ms. The dashed vertical lines in Fig. 15 mark the peak OH locations at the corresponding heights. The integral time scales at peak locations for $x/D=20$ and $x/D=30$ are almost equal, and those for $x/D=40$ are almost twice as large. The OH time scales in similar $H_2/CH_4/N_2$ flames were previously observed to be constant within the jet; that is, below the flame tip and on the fuel side of the reaction layer (Renfro *et al.*, 2000c). The same trend is observed here for $x/D=20$ and $x/D=30$, where the integral time scales on the fuel side are nearly constant until the peak OH location and increase rapidly towards the air-side into the mixing layer. At $x/D=40$, the peak OH concentration occurs at the jet centerline and is past the flame tip, which had previously not been examined by PITLIF measurements.

An LES investigation of flame H3 was performed by Kempf *et al.* (2002) using a laminar flamelet model. Based on our time-series simulations, this model is expected to be reasonable for OH time-scale predictions. Moreover, our measured PDFs of OH strongly support this formulation. Figure 16 shows PDFs measured in the H3 flame at various radial and axial locations. For a fixed axial location, the distribution of instantaneous OH values is nearly the same, with the only difference being the frequency of

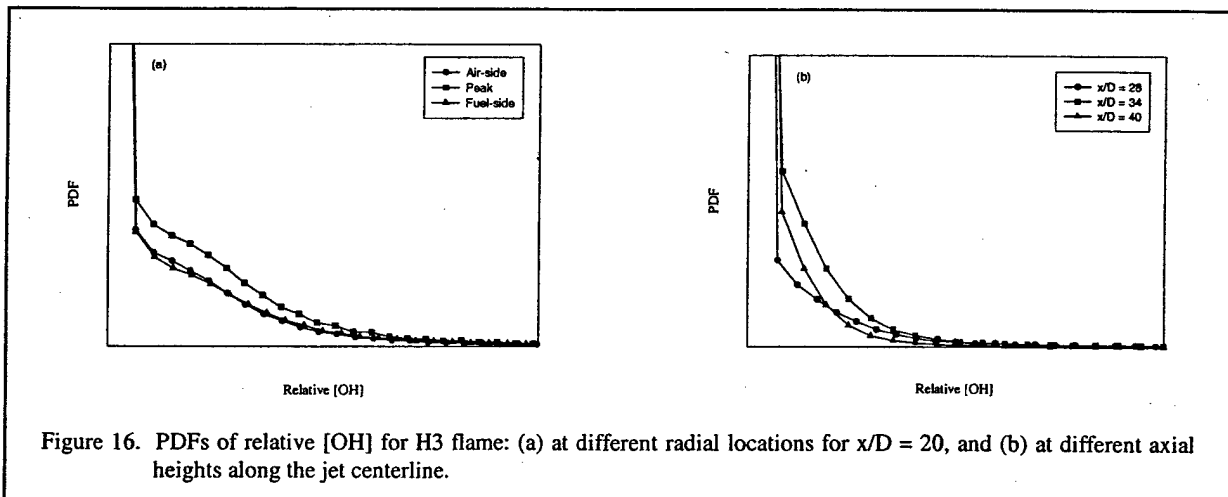


Figure 16. PDFs of relative [OH] for H3 flame: (a) at different radial locations for $x/D = 20$, and (b) at different axial heights along the jet centerline.

[OH] fluctuations. This result implies that for different radial positions, the flame sheet that fluctuates past the probe volume is the same and only its fluctuation frequency is dissimilar (Renfro *et al.*, 2000c). For different axial locations, the distribution of OH values within the flame can vary as shown in Fig. 16. Hence, the laminar flamelet approximation accurately describes OH distributions at a fixed height, but varying state relationships may be required as a function of x/D . This complication can be expected to impact the prediction of mean [OH] but not OH time scales (Renfro *et al.*, 2002).

A representative time series predicted by LES is shown in Fig. 17. The simulation displays the same type of intermittent behavior observed in the measured time series (e.g., Fig. 7). These predicted time series were processed to compute OH integral time scales using the same program as for the PITLIF measurements. Figure 18 shows the predicted OH PSDs along the jet centerline for flame H3. The LES results correctly predict a collapse of the power spectra when normalized by their integral time scales. More importantly, the predicted and measured PSD shapes compare very well, as shown in Fig. 19. There is considerably more scatter in the LES power spectrum since the total time for the simulation is only 140 ms, compared to approximately 50 seconds of measured PITLIF data. Low-frequencies are therefore noisy in the simulation. The comparison still shows excellent agreement, indicating that LES predicts the correct distribution of large-scale fluctuations as determined by the intermittent OH concentrations.

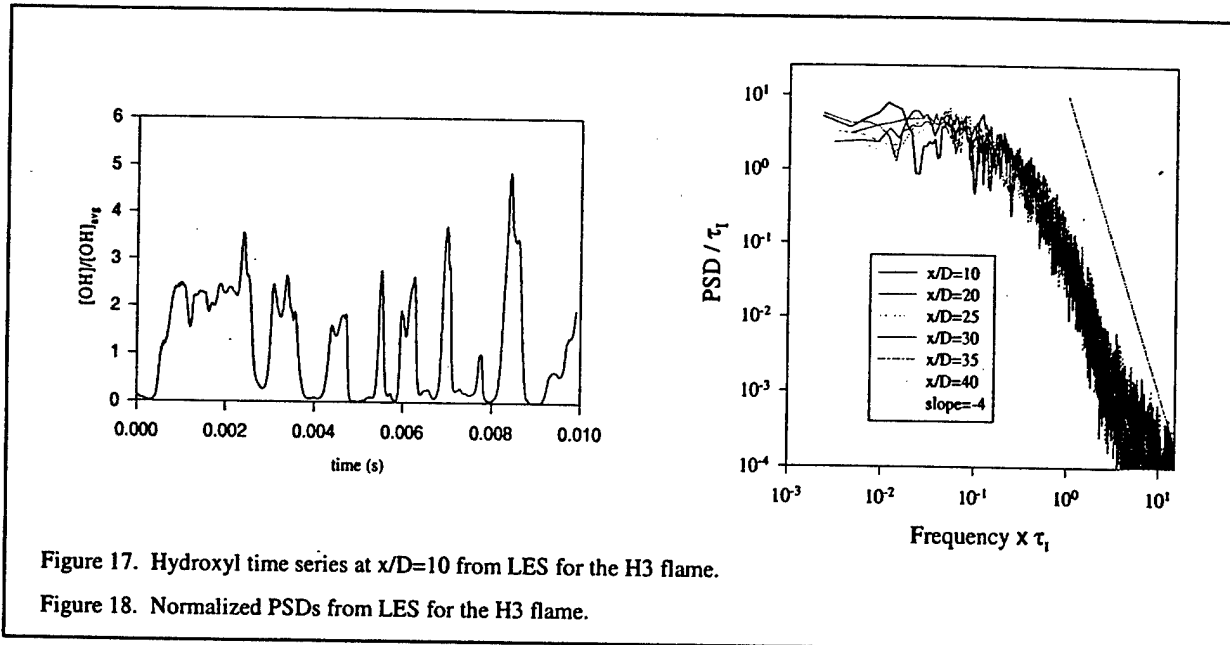


Figure 17. Hydroxyl time series at $x/D=10$ from LES for the H3 flame.

Figure 18. Normalized PSDs from LES for the H3 flame.

Figure 20 shows the OH integral time scales from both PITLIF and LES as a function of axial height along the jet centerline. The measured τ_i values range from 0.8 to 1.7 ms and dip to a minimum at $x/D = 34$. This axial location corresponds to the peak in mean [OH] concentration. The time scales, τ_i , are nearly constant in the $x/D = 20-25$ range (consistent with previous measurements), decrease somewhat until $x/D = 34$, and then increase rapidly to significantly higher values farther downstream of the flame tip. The drop in OH integral time scale up to $x/D=34$ is particularly surprising since the velocity on the jet centerline is decreasing over this same range. In our measurements for flame A3, we observed that the time-scale was nearly invariant with axial height (Renfro *et al.*, 2000c), but we did not previously include measurements beyond the flame tip. Since our OH measurements at heights below the flame tip are essentially conditioned on the presence of a flame, the trends in Fig. 20 could be a result of velocities conditioned on the stoichiometric mixture fraction. Han and Mungal (2000) have shown that the stoichiometric velocity (measured as the velocity at the CH contour) is nearly independent of axial height up to the flame tip in non-premixed flames.

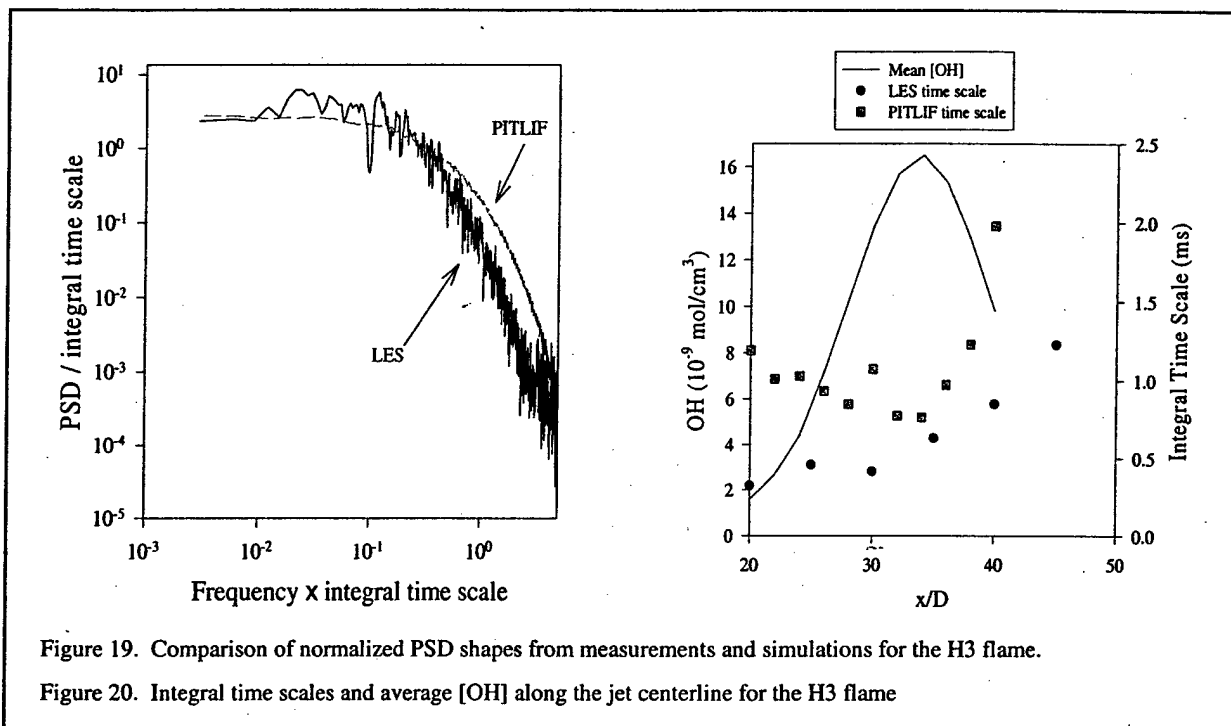


Figure 19. Comparison of normalized PSD shapes from measurements and simulations for the H3 flame.

Figure 20. Integral time scales and average [OH] along the jet centerline for the H3 flame

In the simulation, the time scales are also nearly constant below the flame tip, and increase substantially above the flame tip. However, the simulations do not show a local minimum. The measured minimum at $x/D=34$ is similar to the trend observed in the τ_1 radial profiles. In particular, we have demonstrated that the peak [OH] location, either radially or axially, results in a local decrease in the integral time scale for OH owing to its narrow distribution in mixture-fraction space (Renfro *et al.*, 2002). Essentially, small mixture-fraction fluctuations that cross the stoichiometric value will sample both sides of the OH profile. Thus a small sinusoidal fluctuation in Z can become a large fluctuation with twice the frequency for OH. This issue was discussed by Renfro *et al.* (2002) with respect to simple stochastic simulations of simultaneous Z and OH time series.

3.4 PITLIF Measurements in Premixed Flames

Measurements were also made in premixed turbulent flames to assess the effects of reaction zone width on PITLIF statistics. In particular, PITLIF has been employed to study turbulent premixed combustion in the thickened preheat regime (Peters, 1999). Previous investigations for non-premixed flames have provided solid evidence for the existence of wrinkled flamelets (Renfro *et al.*, 2000c). Therefore, the objective here was to determine whether PITLIF time-series measurements could distinguish between flamelet and possible non-flamelet regimes, as hypothesized to exist under some conditions for turbulent premixed flames.

The thickened preheat regime (Peters, 1999) occurs when small energetic eddies penetrate and broaden the preheat zone, but dissipate before they can affect the thin inner reaction zone because of the increased viscosity of the higher temperature gases. This eddy penetration into the preheat zone results in increased transport of heat and radicals from the reaction zone to the unburned reactants. Recent experimental evidence supports the existence of a thickened preheat regime. Chen *et al.* (1996), for example, provide two-dimensional Rayleigh scattering images for a set of turbulent stoichiometric methane-air jet flames. From their images, locations near the flame front are observed where the distance between temperature iso-contours expands within the preheat zone. This result can be explained by small yet energetic eddies entering into and broadening the preheat zone, as hypothesized for the thickened preheat regime. Similarly, Chen and Mansour (1999) present simultaneous two-dimensional temperature and OH

measurements (via laser-induced predissociative fluorescence and planar saturated LIF, respectively) in premixed methane-air Bunsen flames. At low turbulence intensities, large temperature and OH gradients are typically present, consistent with a wrinkled flamelet concept. However, as the turbulence intensity rises, locations having reduced temperature gradients are observed, thus again suggesting movement toward a thickened preheat zone.

The thickness of the CH layer in a flame is much thinner than that of OH, and can thus be used as a more stringent test for the indication of an instantaneous reaction zone. Mansour *et al.* (1998) have reported simultaneous two-dimensional temperature and CH images in the same flames studied by Chen *et al.* (1996), and have also extracted line profiles from their images to more directly compare temperature and CH information. Their results indicate behavior similar to that found for their previous temperature/OH imaging measurements (Chen and Mansour, 1999). In particular, locations exist containing steep temperature gradients and large CH peaks, corresponding to a wrinkled flamelet. However, locations also exist having smaller temperature gradients, thus providing additional evidence for the existence of a thickened preheat zone ahead of the inner reaction layer. Reduced CH and even the absence of CH are also observed in high strain-rate flames, specifically at locations for which the temperature gradient indicates localized extinction.

The burner used for our turbulent premixed CH₄/air flames is identical to that used by Prasad *et al.* (1999). The premixed fuel/air mixture exits from a 15-mm, inner-diameter tube that is surrounded by a 100-mm diameter air co-flow tube. A hydrogen diffusion flame is used as an annular pilot for the flames, with the hydrogen issuing from 90 ports, each 0.2-mm in diameter, placed at a mean burner diameter of 20 mm. The time series were obtained for six premixed methane-air flames at three equivalence ratios (0.6, 0.7, and 0.8) and two Reynolds numbers (8700 and 17,400) based on cold flow properties at the jet exit. The hydrogen pilot flow rates used in this investigation were 2 mg/s and 3.5 mg/s for the Re=8700 and Re=17,400 flames, respectively. On average, the pilot accounted for 6 to 8% of the total flame heat release. Time series were obtained at five or more radial locations along each mean profile by sampling 4096 data points at 16 kHz and 32 kHz for the Re=8700 and Re=17,400 flames, respectively. Fifty consecutive time series were taken at each location permitting autocorrelation functions and power spectral densities (PSDs) to be averaged, thus resulting in cleaner statistics.

Typical OH fluorescence time series, obtained in the Re=8700, $\Phi=0.8$ premixed turbulent flame at $x=60$ mm, are shown in Fig. 21. On the air side (AS) of the mean [OH] profile, an intermittent behavior occurs similar to that found in non-premixed flames (Renfro *et al.*, 2000c). However, at the location of [OH]_{max}, the OH time series displays little or no intermittency. This is a surprising result as the turbulence alone might be expected to move the reaction zone responsible for producing OH sufficiently far from the probe volume so as to observe intermittency in the measured time series. Nonetheless, this is clearly not the case at [OH]_{max} locations below the flame tip. The resulting change in the fluorescence time-series, as compared to those generally found for non-premixed flames (Renfro *et al.*, 2000c), indicates a reaction zone differing from the typical wrinkled flamelet model. Towards the centerline of the burner, into the reactant side (RS) of the mean [OH] profile, we again observe intermittent behavior. However, the time scales at which OH fluctuations occur are quite different on the reactant as compared to the air side, as is apparent from Fig. 21. In general, the fluctuations at the peak and reactant side of the mean [OH] profiles are much faster than those observed on the air side, consistent with the mean velocity profiles (Prasad *et al.*, 1999).

The faster fluctuations on the reactant side of the OH radial profile are also apparent by computing OH integral time scales from their respective autocorrelation functions. The results are shown in Fig. 22 for three Re=17,400 flames at $\Phi=0.6-0.8$. The integral time scales low in the flame rise sharply from the reactant side to the air side of [OH]_{max}. In particular, τ_i values increase radially by a factor of ~10 in all flames at $x=20$ mm, with the relative increase becoming smaller farther from the jet exit. This rapid increase in τ_i has been observed previously in non-premixed flames, but was limited to a factor of three at all heights (Renfro *et al.*, 2000c). From the velocity profiles in the $\Phi=0.8$ flames (Prasad *et al.*, 1999),

mean axial velocities drop by approximately a factor of eight across the radial locations where OH data were collected at $x=20$ mm. Hence, the fluctuation rates of OH lower in the flames may be strongly influenced by mean convective velocities across the reaction zone.

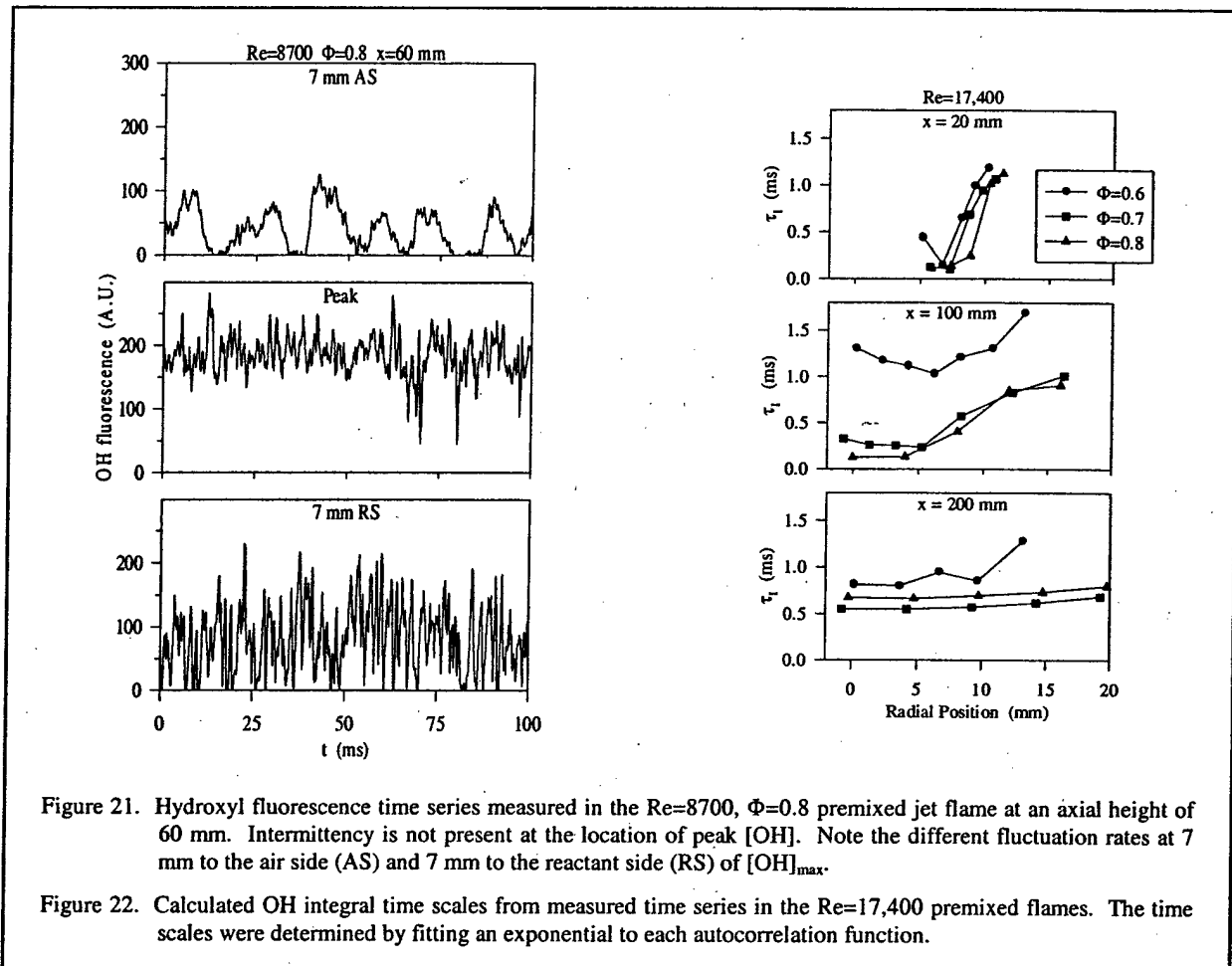


Figure 21. Hydroxyl fluorescence time series measured in the $Re=8700$, $\Phi=0.8$ premixed jet flame at an axial height of 60 mm. Intermittency is not present at the location of peak [OH]. Note the different fluctuation rates at 7 mm to the air side (AS) and 7 mm to the reactant side (RS) of $[OH]_{max}$.

Figure 22. Calculated OH integral time scales from measured time series in the $Re=17,400$ premixed flames. The time scales were determined by fitting an exponential to each autocorrelation function.

The OH integral time scales are nearly constant across the entire width of the flow at downstream locations ($x \geq 150$ mm) above the mean flame brush. For the $\Phi=0.8$ flames, the velocities at the greatest radial locations where OH data were taken are roughly 50% of the corresponding centerline velocities (Prasad *et al.*, 1999); thus, traditional turbulent scaling based on a mean convective velocity does not directly apply to OH integral time scales at $x \geq 150$ mm. This departure was also found to be the case by Renfro *et al.* (2002) for non-premixed turbulent flames, where the OH time scales differed from those of mixture fraction because of scalar intermittency. For axial locations beyond the flame tip, mean equivalence ratio plots (Prasad *et al.*, 1999) show that air entrainment has reached the jet centerline. Consequently, the only reactions relevant to OH are slower three-body recombination reactions. Barlow *et al.* (1990) have estimated a time scale for these reactions on the order of 3 ms, which is comparable to the integral time scale at these locations. Hence, the finding that these integral time scales are independent of mean convective velocity may be a result of opposing effects between turbulent convection and turbulence-chemistry interactions for three-body OH destruction reactions. The measurements might also be affected by scalar intermittency, as with our non-premixed flames, and thus may require consideration of appropriate relationships between velocity and OH.

4. Conclusions

The PITLIF technique has been applied to detailed measurements in hydrogen-based jet flames with large variations in Reynolds number, burner diameter, and axial and radial measurement location. These measurements confirm that scalar fluctuation statistics, such as the PSD, are self similar when normalized by the integral time scale. The normalized autocorrelation function is found to be nearly exponential, but the variation in integral time scale cannot be explained by using simple eddy-turn-over time scaling. In particular, the time scales show a variation with Reynolds number that is stronger than $1/Re$, the time scales are nearly invariant for fuel-side locations below the flame tip, and the time scales show a local minimum in regions of high scalar gradients. With the exception of this Re dependence, each of these trends can be described by a simple stochastic simulation. The simulation is based on a laminar flamelet approximation, which is supported by the measured PDFs. Scalar intermittency causes local minimums in the measured integral time scales; however, the variation in time scales among scalars is accurately described based on the state relationship widths. Constant fluctuation rates with axial height can also be understood based on conditional velocities measured in similar flames. The Reynolds number variation may arise from a shift in the virtual origin of the jets with Re , but no conclusive explanation is presently available.

Measurements in premixed flames, where the flamelet approximation may not be applicable, show significant differences in the structure of the measured PITLIF statistics. The PITLIF technique is clearly capable of distinguishing between thin and thick reaction zones, and may be useful for future examination of alternate burning modes. In the nonpremixed case, the PITLIF instrument is a useful tool for understanding the effects of heat release on turbulent fluctuation rates, and can provide new data for improved model validation.

In fact, an initial attempt to use PITLIF for the validation of large-eddy simulations (LES) was completed in a standard hydrogen/nitrogen flame. The LES comparison was conducted in collaboration with researchers from Technische Universität Darmstadt. The PSDs predicted by LES are remarkably similar to the PITLIF measurements, thus confirming the capability of LES in capturing the large-scale behavior of a turbulent jet flame. However, LES underpredicts the time scales by a factor of two. This result has implications for sub-grid scale mixing models, but future work will be required to determine a procedure for improving such models. Of equal importance, LES uses a computational time step that is based on the predicted fluctuation rates. Since these rates are too fast, LES calculations are inherently over-resolved. Hence, improvements to the model will allow not only better predictions for the physics of nonpremixed flames, but will also permit simulations to be performed at less computational expense. These comparisons are the subject of ongoing collaborative research with Technische Universität Darmstadt.

5. Personnel and Significant Collaborations

Professors Normand M. Laurendeau, Galen B. King, and Jay P. Gore have been the co-principal investigators for this research program. Dr. Michael W. Renfro was a visiting assistant professor. Mr. Walter A. Guttenfelder and Mr. Amit Chaturvedy were M.S. students working on the project.

A collaborative PITLIF program has recently been developed with the Air Force Research Laboratory (AFRL). The lead AFRL investigator is Dr. James Gord; other participating AFRL researchers include Sukesh Roy, Terry Meyer and Michael Brown. This new program was defined following a seminar and an extended visit with AFRL researchers at Wright-Patterson AFB in June, 2002. A two-week visit is planned by selected AFRL personnel to learn the operating fundamentals of the PITLIF technique in January, 2003. An advanced PITLIF facility will then be designed and built at AFRL during the summer of 2003 under the direction of Prof. Galen King. This new PITLIF facility will be used to explore turbulence-chemistry interactions in a variety of turbulent flames at Wright-Patterson AFB. Initial OH experiments will be conducted by using repeatable vortices produced by an existing Rolon burner at AFRL.

6. Related Publications and Presentations

6.1 Refereed Journals

- Renfro, M. W., Gore, J. P., and Laurendeau, N. M. (2002). Scalar time-series simulations for turbulent nonpremixed flames. *Combustion and Flame*, v. 129, 120-135.
- Renfro, M. W., Chaturvedy, A., and Laurendeau, N. M. (2001). Semi-quantitative measurements of CH concentration in atmospheric-pressure counterflow diffusion flames using picosecond laser-induced fluorescence. *Combustion Science and Technology*, v. 169, 25-43.
- Lakshmanarao, A., Renfro, M. W., King, G. B., and Laurendeau, N. M. (2001). Acetone as a tracer for mixture fraction time-series measurements in turbulent non-reacting jets. *Experiments in Fluids*, v. 30, 595-596.
- Renfro, M. W., Guttenfelder, W. A., King, G. B., and Laurendeau, N. M. (2000). Scalar time-series measurements in turbulent $\text{CH}_4/\text{H}_2/\text{N}_2$ nonpremixed flames: OH. *Combustion and Flame*, v. 123, 389-401.
- Renfro, M. W., Gore, J. P., King, G. B., and Laurendeau, N. M. (2000). Self-similarity of hydroxyl-concentration temporal statistics in turbulent nonpremixed jet flames. *AIAA Journal*, v. 38, 1230-1236.
- Renfro, M. W., King, G. B., and Laurendeau, N. M. (2000). Scalar time-series measurements in turbulent $\text{CH}_4/\text{H}_2/\text{N}_2$ nonpremixed flames: CH. *Combustion and Flame*, v. 122, 139-150.

6.2 Conference Proceedings and Presentations

- Renfro, M. W., Venkatesan, K. K., and Laurendeau, N. M. (2002). Cross-sections for CH quenching by N_2 and H_2O from 1740 to 2160 K. Presented at the Twenty-Ninth International Symposium on Combustion, The Combustion Institute, Sapporo, Japan.
- Renfro, M. W., Venkatesan, K., and Laurendeau, N. M. (2002). Cross-sections for CH quenching by N_2 and H_2O from 1740 to 2160 K. Proceedings of the Central States Section Meeting, The Combustion Institute, Knoxville, TN.
- Guttenfelder, W. A., Renfro, M. W., King, G. B., and Laurendeau, N. M. (2002). Hydroxyl time-series measurements in turbulent non-premixed swirling flames. Proceedings of the Central States Section Meeting, The Combustion Institute, Knoxville, TN.
- Chaturvedy, A., Renfro, M. W., and Laurendeau, N. M. (2002). Measurements of OH time series in turbulent non-premixed jet flames. Proceedings of the Central States Section Meeting, The Combustion Institute, Knoxville, TN.
- Renfro, M. W., Guttenfelder, W. A., King, G. B., and Laurendeau, N. M. (2001). Gated photon counting for measurements of scalar-fluctuation time-scales in turbulent flames. Presented at the Annual Meeting, The Optical Society of America, Long Beach, CA.
- Renfro, M. W., Chaturvedy, A., and Laurendeau, N. M. (2001). Semi-quantitative measurements of CH concentration at atmospheric pressure. Proceedings of the Second Joint U.S. Section Meeting, The Combustion Institute, Oakland, CA.
- Renfro, M. W., Gore, J. P., and Laurendeau, N. M. (2001). A technique for simulating realistic time series for scalars using a laminar-flamelet construction. Proceedings of the Second Joint U.S. Section Meeting, The Combustion Institute, Oakland, CA.
- Guttenfelder, W. A., Renfro, M. W., King, G. B., and Laurendeau, N. M. (2001). Time-series measurements of OH in turbulent lean premixed methane/air jet flames. Proceedings of the Second Joint U.S. Section Meeting, The Combustion Institute, Oakland, CA.

6.3 Conference Posters

- Renfro, M. W., Chaturvedy, A., King, G. B., Laurendeau, N. M., Kempf, A., Dreizler, A., Sadiki, A., and Janicka, J. (2002). Comparison of measured and predicted scalar time scale in flame H3. Poster Presentation, Sixth International Workshop on Turbulent Nonpremixed Flames, Sapporo, Japan.

- Renfro, M. W., Chaturvedy, A., and Laurendeau, N. M. (2001). Semi-quantitative measurements of CH concentration at atmospheric pressure. Poster Presentation, Gordon Research Conference on Laser Diagnostics in Combustion, South Hadley, MA.
- Guttenfelder, W. A., Renfro, M. W., King, G. B., and Laurendeau, N. M. (2001). OH time-series measurements in turbulent lean premixed methane/air jet flames and nonpremixed swirling flames. Poster Presentation, Gordon Research Conference on Laser Diagnostics in Combustion, South Hadley, MA.
- Renfro, M. W., Gore, J. P., and Laurendeau, N. M. (2000). Hydroxyl time-series simulations for turbulent nonpremixed flames. Poster Presentation, Twenty-Eighth International Symposium on Combustion, Edinburgh, Scotland.
- Renfro, M. W., King, G. B., and Laurendeau, N. M. (2000). Time-series measurements of scalars in $H_2/CH_4/N_2$ jet flames. Poster Presentation, Fifth International Workshop on Turbulent Nonpremixed Flames, Delft, The Netherlands.

7. References

- Barlow, R.S. and Carter, C.D. (1994), *Combust. Flame* **97**, 261.
- Barlow, R.S., Dibble, R.W., Chen, J.Y., and Lucht, R.P. (1990), *Combust. Flame* **82**, 235.
- Bergmann, V., Meier, W., Wolff, D., and Stricker, W. (1998), *Appl. Phys. B* **66**, 489.
- Bowman, C.T., Hanson, R.K., Davidson, D.F., Gardiner Jr., W.C., Lissianski, V., Smith, G.P., Golden, D.M., Frenklach, M., and Goldenburg, M., http://www.me.berkeley.edu/gri_mech/ (1995).
- Chen, Y.-C. and Mansour, M.S. (1999), *Exp. in Fluids* **26**, 277.
- Chen, Y.-C., Peters, N., Schneemann, G.A., Wruck, N., Renz, U., and Mansour, M.S. (1996), *Combust. Flame* **107**, 223.
- Clemens, N. T. and Paul, P. H., *Combust. Flame* **102**:271 (1995).
- Dibble, R.W., and Hollenbach, R.E. (1981), *Proc. Combust. Inst.* **18**, 1489.
- Drake, M.C. and Pitz, R.W. (1985), *Exp. Fluids* **3**, 283.
- Faeth, G.M., Kounalakis, M.E., and Sivathanu, Y.R. (1991), *Chem. and Int. Lab. Sys.* **10**, 199.
- Han, D. and Mungal, M. G. (2000), *Proc. Combust. Inst.* **28**, 261.
- Janicka, J. and Dreizler, A. (2001). Private Communication, TU-Darmstadt.
- Kempf, A., Dreizler, A., Sadiki, A., and Janicka, J. (2002). Private Communication, TU-Darmstadt.
- Kounalakis, M.E., Gore, J.P., and Faeth, G.M. (1991), *J. Heat Trans.* **113**, 437.
- Lakshmanarao, A., M.S. Thesis, Purdue University, West Lafayette, IN, 1999.
- Lutz, A.E., Kee, R.J., and Grcar, J.F. (1996), Sandia National Laboratory, SAND96-8243.
- Mansour, M.S., Peters, N., and Chen, Y.-C. (1998), *Proc. Combust. Inst.* **27**, 767.
- Meier, W., Barlow, R. S., Chen, Y.-L. and Chen, J.-Y., *Combust. Flame* **123**:326-343 (2000), see also <http://www.st.dlr.de/EN-CV/flamedat/intro.htm>
- Meier, W., Prucker, S., Cao, M.H., Stricker, W. (1996), *Combust. Sci. Tech.* **118**, 293.
- Namer, I. and Schefer, R.W. (1985), *Exp. Fluids* **3**, 1.
- Neuber, A., Krieger, G., Tacke, M., Hassel, E., and Janicka, J. (1998), *Combust. Flame* **113**, 198.
- Pack, S.D., Renfro, M.W., King, G.B., and Laurendeau N.M. (1998), *Opt. Lett.* **23**, 1215.
- Pack, S.D., Renfro, M.W., King, G.B., and Laurendeau, N.M. (1999), *Combust. Sci. Technol.* **140**, 405.
- Peters, N. (1986), *Proc. Combust. Inst.* **21**, 1231.
- Pfuderer, D.G., Neuber, A.A., Früchtel, G., Hassel, E.P., and Janicka, J. (1996), *Combust. Flame* **106**, 301.
- Prasad, R.O.S., Paul, R.N., Sivathanu, Y.R., and Gore, J.P. (1999), *Combust. Flame* **117**, 514.
- Reisel, J.R., Carter, C.D., and Laurendeau, N.M. (1997), *Energy and Fuels* **11**, 1092.
- Renfro, M. W., Gore, J. P., King, G. B., and Laurendeau, N. M. (2000a), *AIAA J.* **38**, 1230.
- Renfro, M. W., Guttenfelder, W. A., King, G. B., and Laurendeau, N. M. (2000c), *Combust. Flame* **123**, 389.
- Renfro, M. W., King, G. B., and Laurendeau, N. M. (2000b), *Combust. Flame* **122**, 139.

- Renfro, M. W., Klassen, M. S., King, G. B., and Laurendeau, N. M. (1996), *Opt. Lett.* **22**, 175.
- Renfro, M.W., King, G.B., and Laurendeau, N.M. (1999a), *Appl. Opt.* **38**, 4596.
- Renfro, M.W., Pack, S.D., King, G.B., and Laurendeau, N.M. (1999b), *Appl. Phys. B* **69**, 137.
- Renfro, M.W., Sivathanu, Y.R., Gore, J.P., King, G.B., and Laurendeau, N.M. (1999c), *Proc. Combust. Inst.* **27**, 1015.
- Renfro, M.W., Gore, J.P., and Laurendeau, N.M. (2002), *Combust. Flame* **129**, 120.
- Schneider, C., Dreizler, A., and Janicka, J., Personal Communication (2000).
- Sivathanum Y.R., Gore, J.P., and Dolinar, J. (1991), *Combust. Sci. Technol.* **76**, 45.

SEMI-QUANTITATIVE MEASUREMENTS OF CH CONCENTRATION IN ATMOSPHERIC-PRESSURE COUNTERFLOW DIFFUSION FLAMES USING PICOSECOND LASER-INDUCED FLUORESCENCE

MICHAEL W. RENFRO,* AMIT CHATURVEDY, AND
NORMAND M. LAURENDEAU

Flame Diagnostics Laboratory, School of Mechanical
Engineering, Purdue University, West Lafayette,
Indiana, USA

Measurements of relative CH concentrations and absolute fluorescence lifetimes are reported in atmospheric pressure, laminar, counterflow diffusion flames using picosecond laser-induced fluorescence combined with a novel photon-counting technique. Three fuels consisting of nitrogen-diluted methane, ethane, or acetylene were used with global strain rates varying from 20 s^{-1} to 60 s^{-1} . The concentrations were normalized by a measurement in one of the methane flames. The resulting (CH) ratios are corrected for quenching effects and are quantitative with uncertainties of typically $\pm 7\%$ (95% confidence interval). The results were compared to predictions from OPPDIF using two chemical mechanisms, GRI-2.11 and GRI-3.0. Both mechanisms correctly predict the relative CH concentrations between the ethane and methane flames but overpredict those between the acetylene and methane flame. Predictions of fluorescence lifetimes were computed from the OPPDIF species and temperature profiles using species-dependent quenching cross sections from the literature. The predicted fluorescence lifetimes are larger than the measurements by 10–15% in the methane and acetylene flames and by 50% in the ethane flames.

Keywords: Picosecond laser-induced fluorescence; fluorescence lifetimes; CH concentrations; counterflow diffusion flames

*E-mail: renfro@ecn.purdue.edu

INTRODUCTION

Accurate predictions of emissions from advanced low-NO_x combustors require an increasingly accurate description of the formation of NO through various chemical mechanisms. At lower temperatures, formation of NO via the CH-initiated "prompt" mechanism can dominate total NO production. Therefore, the ability to predict CH concentrations becomes very important to the goal of designing combustors with overall reduced pollutant emissions. However, considerably less information is available for CH concentrations than for other flame species such as OH and NO because of (1) lower concentrations and, hence, lower signal levels (by as much as three orders of magnitude), (2) interferences from soot precursors in the visible wavelengths associated with the first CH electronic transition, and (3) the difficulty of quantifying the CH measurement. In particular, quantifying a CH laser-induced fluorescence (LIF) signal requires consideration of both the electronic quenching rate coefficient and a proper procedure for signal calibration.

Despite these difficulties, several quantitative measurements of CH have recently been reported in the literature. Most of these studies focus on low-pressure flames for which the fluorescence lifetime is long compared to typical Q-switched laser pulses (e.g., Luque and Crosley, 1996; Berg et al., 2000). Calibration is typically performed by comparison to laser Rayleigh scattering signals (Salmon and Laurendeau, 1985). In atmospheric pressure flames, the CH lifetime is of the order of 2–5 ns and cannot be directly measured using a Q-switched laser. Instead, picosecond excitation must be used (e.g., Renfro et al., 2000). Unfortunately, with a typical ps laser, the duty cycle is much larger than that for a Q-switched laser (by at least four orders of magnitude) such that gated detection is significantly less effective at recovering accurate Rayleigh scattering signals from background noise. Thus, while the quenching dependence can be removed, an absolute calibration is elusive.

Absolute CH measurements have also been made using direct absorption (Joklik et al., 1986; Woiki et al., 1998) or cavity ring down spectroscopy (Derzya et al., 1999; Mercier et al., 1999) at atmospheric pressure. However, the limited spatial resolution from these line-of-sight measurements can be unacceptable in many applications. Presently, a robust technique is not available for measuring quantitative, spatially resolved, CH concentrations in atmospheric-pressure flames.

If fluorescence lifetimes can be modeled with reasonable confidence, then LIF with Q-switched lasers can be used with the quenching dependence numerically removed (e.g., Luque et al., 2000). Nevertheless, this calculation depends on the accuracy of species- and temperature-dependent quenching cross sections, which are usually measured at very low pressures.

Tamura et al. (1998) provide a thorough discussion of the range of cross-section data available for CH. In summary, measurements have been made for the most important colliders up to temperatures of only 1400 K (Garland and Crosley, 1986). Unlike for OH and NO, the dominant quenching partner at very high temperatures appears to be either N₂ or CO₂. Unfortunately, measurements of the temperature dependence of the CH/N₂ cross section only extend to 950 K (Heinrich and Stuhl, 1995), where a sharp T^{3.4} dependence is observed. Tamura et al. refit this data, including available cross sections at 1300 K, and found a T^{2.9} dependence, but significant uncertainty still exists at actual flame temperatures. In addition, quenching cross sections for some species, such as H₂O, have not even been examined above 500 K. Clearly, significant work is needed to further refine the existing correlations for controlling CH cross sections.

The purpose of the present paper is to report measurements of relative CH concentrations in eight counterflow nonpremixed flames at atmospheric pressure. The LIF signal has been corrected for the effects of quenching by direct measurement of the fluorescence lifetimes; however, an absolute calibration has not been performed. The concentration measurements are normalized by the peak value in one of the methane flames such that the concentration ratios are fully quantitative. These ratios have been predicted for the eight test flames using a one-dimensional numerical code and two comprehensive kinetic mechanisms. Based on the predictions of major-species concentrations and temperature, a modeled value for the fluorescence lifetime is computed using species-dependent quenching cross sections. These lifetime and concentration ratio predictions are compared to the quantitative measurements. To our knowledge, this study represents the first comparison of directly measured and modeled lifetimes for CH in atmospheric pressure flames. A full error analysis is invoked to estimate the statistical significance of the comparisons such that suggestions for improvements to the model can be made even without an absolute concentration calibration. In addition, the novel use of a gated photon

counting procedure is examined for improved measurements of quenching independent concentrations.

EXPERIMENTAL PROCEDURE

The experimental setup for ps-LIF of CH is shown in Figure 1 and is essentially the same as that used by Renfro et al. (2000). A continuous-wave, multi-mode, argon-ion laser was used to pump a mode-locked Ti:Sapphire laser at 18 W. The output of the Ti:Sapphire laser consisted of 18-ps pulses (FWHM) with a repetition rate of 80 MHz and an average power of 2.6 W. These IR pulses were frequency doubled using an angle-tuned BBO crystal such that the output had a wavelength of 430.55–430.75 nm with an average power of 350 mW. At these wavelengths, approximately 10 Q-branch rotational transitions in the $X^2\Pi - A^2\Delta(0,0)$ vibronic band of CH are excited in the flame. This wavelength range is selected to minimize the variation of the Boltzmann fraction as a function of temperature. Simulation of the absorption spectra versus temperature, using a code developed by Seitzman (1991), shows an absorption coefficient variation of only $\pm 3\%$ at 1500–2500 K. The resulting fluorescence in the X-A (0,0) band was collected perpendicular to the laser path using two 50.8-mm diameter lenses with a solid collection angle of $f/3$ and a magnification of 1.1. The fluorescence was

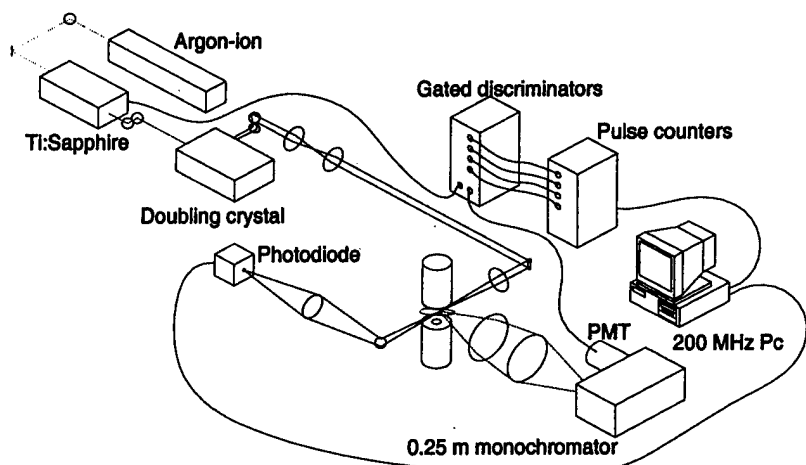


Figure 1. Experimental setup for ps-LIF.

focused onto the entrance slit of a 0.25-m monochromator. Based on the entrance and exit slit settings and the focused laser beam diameter ($\sim 100 \mu\text{m}$), the probe volume in the flame was $0.1 \times 0.1 \times 0.9 \text{ mm}^3$ and the spectral detection window was 425–435 nm. The longest dimension of the probe volume was aligned radially across the counterflow flame (for which no substantial gradients were present), so that the 100- μm beam waist best defined the spatial resolution. A Hamamatsu HS5321 PMT biased at -2350 V detected the filtered fluorescence. The resulting electronic pulses from the PMT (each corresponding to a single detected photon) were discriminated and counted using a four-channel gated photon counting system (Pack et al., 1998b).

The arrangement of the gated photon counting system is shown in Figure 2. Three channels (D_2 , D_3 , and D_4) count only the photons that occur in the temporal range indicated relative to the laser pulse (at 0 ns). The photon counts in each bin were averaged over 8×10^6 laser pulses (100 ms) for each reported measurement. Following Pack et al. (1998b) and Renfro et al. (1999), the fluorescence lifetime and species concentration can be calculated from these average photon counts as

$$\tau = \frac{\Delta t}{\ln \left\{ \frac{D_2 - D_3}{D_3 - D_4} \right\}} \quad (1)$$

$$A = \frac{D_2 - D_4}{\exp(-t_0/\tau)(1 - C^2)(1 - C)\tau} = \frac{D_2 - D_3}{\exp(-t_0/\tau)(1 - C)^2\tau}, \quad (2)$$

where τ is the fluorescence lifetime, Δt is the width of each gated bin (3.5 ns), A is proportional to the CH concentration, and $C = \exp(-\Delta t/\tau)$. Eq. (2) is slightly different than that derived by Pack et al., as they compute the amplitude of the fluorescence decay at the beginning of bin D_2 , which may not be proportional to the CH concentration if a delay, t_0 , exists between the laser pulse and the first gated bin. In our present system, this delay is about $t_0 = 0.9 \text{ ns}$ (Renfro et al.). Other than this additional t_0 term, Eq. (2) is algebraically identical to that of Pack et al.

Measurements were made in eight counterflow, laminar diffusion flames. The same counterflow burner was previously used by Ravikrishna and Laurendeau (2000) to measure NO concentrations in diluted ethane and methane flames. The burner consists of two opposed 24.1-mm diameter jets with a separation distance of 20 mm, as shown in

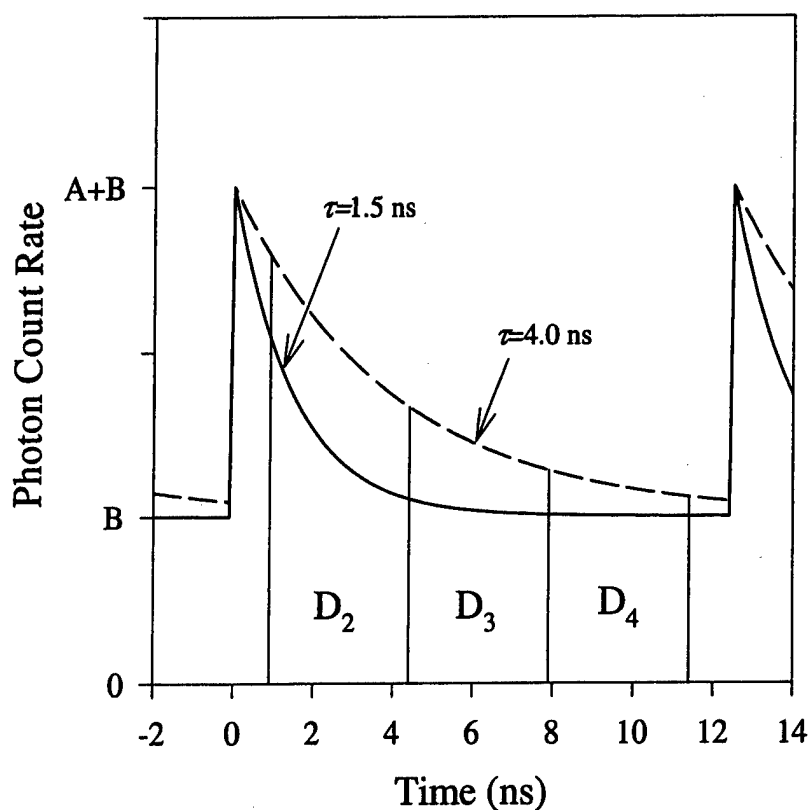


Figure 2. Arrangement of gated bins for the gated photon counting system.

Figure 3. The top burner is water cooled and the bottom burner contains an annular nitrogen jet to shield the flame from disturbances. The boundary conditions for the eight flames studied are given in Table 1. In each case, sufficient nitrogen dilution was used to avoid both soot formation and the resulting interferences that can plague CH LIF (Carter et al., 1998). The two methane flames with the lowest strain rates (CH4-20 and CH4-35), as well as the three ethane flames, are identical to those studied by Ravikrishna and Laurendeau (2000). Uncertainties for the measured flow rates and the computed strain rates are also given in Table 1.

Measurements of τ and A for CH were made along the centerline of each flame. At each location, the results were averaged over 50 separate

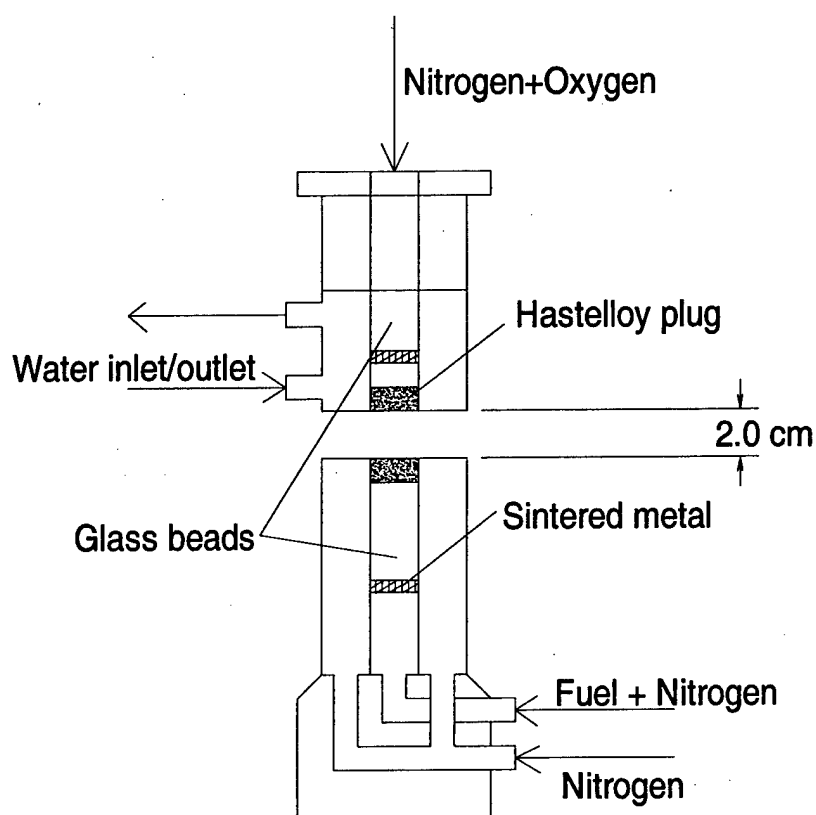


Figure 3. Schematic of opposed-flow burner used for the present nonpremixed flame measurements.

100-ms measurements. We have not calibrated the resulting data and instead report these concentrations relative to the peak CH concentration in flame CH4-20. These concentration ratios are quantitative (having been corrected for fluorescence lifetime variations and laser power fluctuations) but the absolute concentrations are unknown.

NUMERICAL PROCEDURE

Each of the eight test flames was simulated using OPPDIF (Lutz et al., 1996) with two chemical mechanisms: GRI-Mech 2.11 (Bowman et al., 1995) and GRI-Mech 3.0 (Smith et al., 1999). The boundary conditions

Table 1. Flow conditions for the eight test flames

Flame	Experimental boundary conditions					Numerical boundary conditions [§]			
	Fuel [†] (plus N ₂)	Oxidizer [†] (plus N ₂)	U _f [*] (cm/s)	U _{ox} [*] (cm/s)	S [#] (s ⁻¹)	Fuel (plus N ₂)	U _f (cm/s)	U _{ox} (cm/s)	S (s ⁻¹)
CH4-20	25.0±1.1% CH ₄	21.2±1.2% O ₂	21.6	20.7	21.1	25% CH ₄	21.536	20.818	21.2
CH4-35	25.1±1.1% CH ₄	20.9±1.2% O ₂	37.6	34.7	36.2	25% CH ₄	37.721	34.696	36.2
CH4-50	25.0±1.1% CH ₄	21.0±1.2% O ₂	50.0	50.0	50.0	25% CH ₄	50.000	50.000	50.0
CH4-60	25.0±1.1% CH ₄	21.0±1.2% O ₂	60.0	60.0	60.0	25% CH ₄	60.000	60.000	60.0
C2H6-20	14.4±1.2% C ₂ H ₆	21.2±1.2% O ₂	20.2	20.7	20.5	14.5% C ₂ H ₆	19.593	20.818	20.2
C2H6-35	14.5±1.2% C ₂ H ₆	20.9±1.2% O ₂	35.3	34.7	35.0	14.4% C ₂ H ₆	35.367	34.696	35.0
C2H6-48	14.5±1.2% C ₂ H ₆	20.3±1.2% O ₂	44.4	53.0	48.7	14.5% C ₂ H ₆	44.631	52.044	48.3
C2H2-35	7.0±1.3% C ₂ H ₂	20.9±1.2% O ₂	37.5	34.7	36.1	7% C ₂ H ₂	37.721	34.696	36.2

[†]Composition uncertainty is based on the uncertainty in the volumetric flow rates (1.4%, 95% confidence interval).

^{*}The velocities were computed from measured volumetric flow rates assuming a plug-flow velocity profile.

[#]The global strain rate, computed as $S = (U_f + U_{ox})/H$, has an uncertainty of 3% (95% confidence interval) based on the flow rate uncertainties.

[§]All calculations were performed for a 2-cm separation distance (H) with air (79.0% N₂, 21.0% O₂) as the counterflow oxidizer.

for these simulations are included in Table 1. As with the measurements, the predicted concentrations were normalized by the predicted peak concentration in flame CH4-20 (0.84×10^{-11} mol/cm³ for GRI-3.0, and 0.58×10^{-11} mol/cm³ for GRI-2.11). The predicted peak CH concentrations using GRI-3.0 averaged 0.77×10^{-11} , 1.13×10^{-11} , and 1.48×10^{-11} mol/cm³ for the methane, ethane, and acetylene flames, respectively. For each flame, predictions using GRI-2.11 were approximately 25% lower than those from GRI-3.0. Fluorescence lifetimes at each point were predicted using the simulated temperature and major-species concentrations along with the quenching cross sections of

Tamura et al. (1998). Quenching was considered for each of the following colliders: N₂, O₂, CO, CO₂, CH₄, H₂, H, H₂O, and OH. These predictions are discussed with the results.

RESULTS

The peak relative CH concentration in each flame (A/A_{cal}) as well as the CH fluorescence lifetime at the same axial location are reported in Table 2. The uncertainties include the propagation of measured error in bin counts through Eqs. (1) and (2) and the repeatability of the calibration flame measurement (CH4-20). For some locations, the uncertainty in the fluorescence lifetime is large compared to our previously reported OH measurements in similar laminar flames (Pack et al., 1998a). The uncertainty in the fluorescence lifetime results from a small difference in the value $D_3 - D_4$ required in the denominator of Eq. (1). For OH measurements, the typical signal-to-background ratio ($SBR = [D_2 - D_4]/D_4$) is three. This SBR is defined based on our observation that D_4 is mostly flame emission background. For the CH measurements, the best SBR is about 0.3, which causes the reduced numeric value of $D_3 - D_4$. The lower SBR occurs because the CH concentration is so much lower than that for OH and because of the strong chemiluminescence from CH*. It is important to note that the SBR is not the same as the signal-to-noise ratio (SNR), as the noise in the measurement comes primarily from shot noise and not from fluctuations in flame emission. The maximum total photon count for CH is

Table 2. Measured peak CH concentration ratios and fluorescence lifetimes

Flame	A/A_{cal}	Uncertainty ¹ (%)	τ (ns)	Uncertainty ¹ (%)	$D_2 - D_3$	Uncertainty ¹ (%)
CH4-20	1	—	3.40	4.4	1	—
CH4-35	1.32	7.6	3.27	5.0	1.26	5.4
CH4-50	1.15	26.4	3.27	22.6	1.16	7.3
CH4-60	0.97	52.1	3.39	44.9	0.98	9.7
C2H6-20	1.47	9.8	3.16	7.4	1.48	5.6
C2H6-35	1.91	12.5	2.51	10.4	1.73	5.9
C2H6-48	1.77	23.4	2.78	20.6	1.60	7.9
C2H2-35	0.61	40.3	5.10	32.8	0.62	7.7

¹All uncertainties are reported at 95% confidence interval.

about $5 \times 10^6/s$ compared to $\sim 25 \times 10^6/s$ for OH; thus, while the resulting noise for CH is about twice that for OH, the photon count is still relatively large, and reasonably accurate measurements of the bin counts can still be made. For example, at the peak (CH) location in the $S = 20 \text{ s}^{-1}$ methane flame, the relative standard deviation of $D_2 - D_4$ is only 3%, giving an SNR greater than 30.

Equation 2, as compared to the original derivation of Pack et al. (1998b), shows that the concentration will be proportional to $D_2 - D_4$ or $D_2 - D_3$ if the denominator is nearly constant. Figure 4 shows simulations of $A/(D_2 - D_4)$ and $A/(D_2 - D_3)$ as functions of the fluorescence

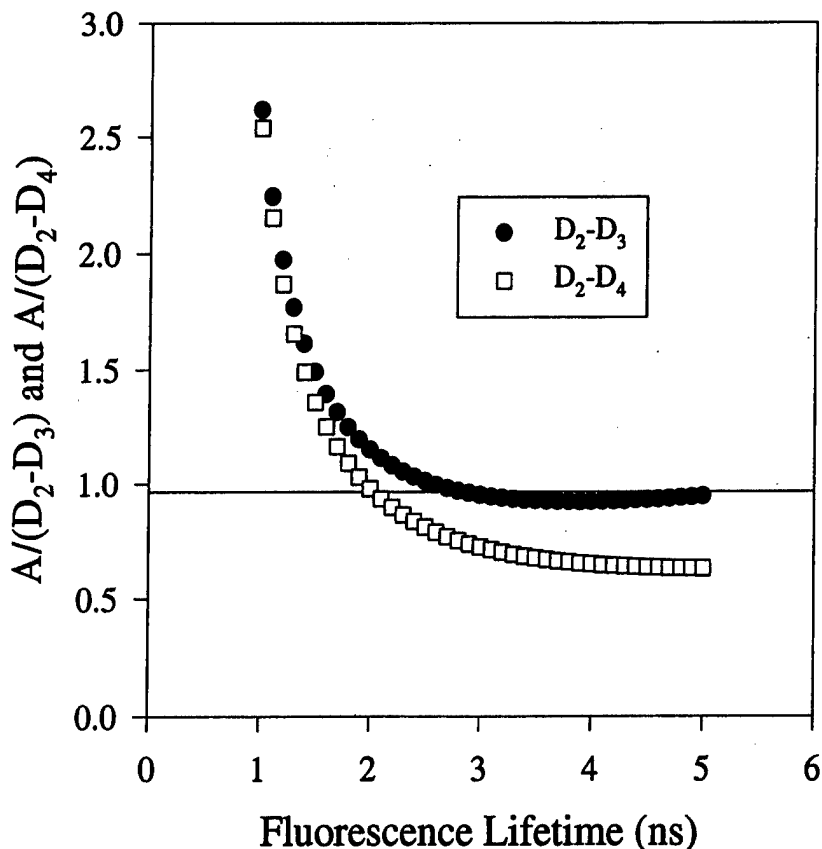


Figure 4. Predicted variation of alternate estimates of CH concentration vs. fluorescence lifetime.

lifetime. These simulations were performed by convoluting exponential decays with the measured response function of our photon counting system. For the range of lifetimes observed in the present flames (2.5–5.1 ns), the concentration is predicted to be proportional to $D_2 - D_3$ ($A = 0.97 \times [D_2 - D_3]$) within 5%. Moreover, since $D_2 - D_3$ is a much larger number than $D_3 - D_4$ (as needed for the lifetime), this alternate estimate for the concentration can often be made with significantly reduced error. The resulting calculation applied to the measured CH data is included in Table 2. We have included the predicted 5% variation of A with $D_2 - D_3$ in the measurement uncertainty and this is the dominant error for most measurement locations because of the relatively high SNR. The alternate and original estimates of A/A_{cal} are nearly identical for each measurement location.

In addition to the peak relative concentration reported in Table 2, full axial profiles were measured in each flame. To facilitate presentation of this data, each profile was fit to a Gaussian function to determine the profile location ($r_{\text{CH,max}}$), profile width (FWHM_{CH}), and profile peak (CH_{max}). Figure 5 shows normalized axial profiles for each of the eight flames. This normalization shows that the eight profiles are nearly identical in shape and can be accurately represented by only their peak relative concentration, axial location, and profile width. The peak values are given in Table 2, and the peak concentration location and FWHM_{CH} for each flame are given in Table 3. Note that as the strain rate increases, the CH profile moves from the air side toward the stagnation plane (~ 10 mm). The uncertainty in this measurement, assessed from repeated measurements in the calibration flame (CH4-20) is only $\pm 0.5\%$ (95% confidence interval). However, the width of the measured CH profile has an uncertainty of $\pm 10\%$ (95% confidence interval). For each flame, the CH profile FWHM is within about 10% of 0.26 mm, such that no distinction can be made from flame to flame within the uncertainty.

COMPARISON TO MODEL

Figure 6 shows the measured peak CH concentration ratios from Table 2 compared to the predictions using GRI-3.0 and GRI-2.11. For this figure, the CH concentrations have been renormalized by the peak concentration in the methane flame at a global strain rate of 35 s^{-1} , as this makes the comparison to the numerical modeling easier to

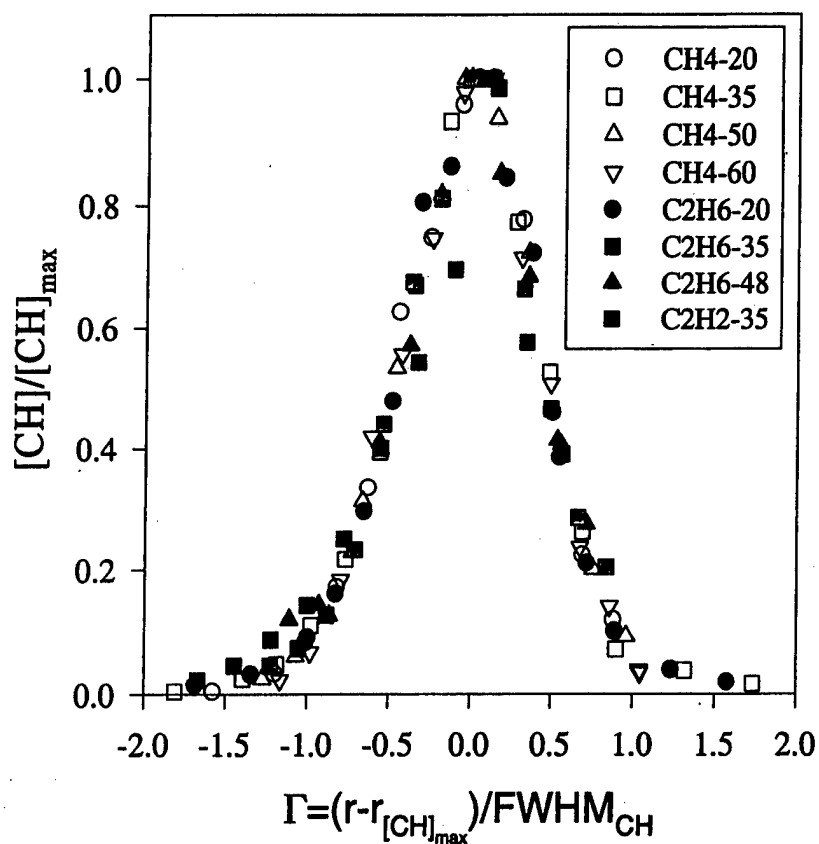


Figure 5. Normalized axial profiles for relative CH concentrations in each of the eight test flames.

visualize. The trends in the methane and ethane flames versus strain rate are generally well captured by the model, and the relative increase in the measured CH concentrations between the methane and ethane flames is equally well captured by the GRI-3.0 and GRI-2.11 mechanisms. However, for both mechanisms, the model predicts higher CH concentrations for the acetylene flame than for the methane flame, while the measured CH concentration ratio is significantly lower in the C_2H_2 flame. To determine the significance of this disparity, we must examine the effect of uncertainties in the experimental boundary conditions. Limits on the boundary conditions were determined from velocity

Table 3. Axial locations of peak CH concentration

Flame	$r_{\text{CH,max}}$ (mm)*	FWHM_{CH} (mm)#
CH4-20	11.52	0.26
CH4-35	11.29	0.24
CH4-50	11.01	0.25
CH4-60	10.72	0.27
C2H6-20	10.39	0.29
C2H6-35	10.32	0.24
C2H6-48	10.04	0.28
C2H2-35	10.66	0.28

*The position is relative to the fuel jet and has an uncertainty of $\pm 0.5\%$ (95% confidence interval).

#The profile width has an uncertainty of $\pm 10\%$ (95% confidence interval).

uncertainties, and predictions using both mechanisms were made at the extreme compositions and strain rates. The predicted ranges of CH concentrations and fluorescence lifetimes were used as indicators of the total uncertainties. The resulting uncertainty in predicted concentration ratios is $\pm 31\%$ (95% confidence interval) for both methane and ethane and $\pm 53\%$ for acetylene based on the boundary conditions. The uncertainty is much larger for the acetylene flame because of the large nitrogen dilution, such that a relatively small variation in C_2H_2 flow rate has a large effect on the composition. However, even considering these boundary-condition errors, both mechanisms overpredict the ratio of CH concentration in the acetylene flame to that in the methane flame by at least a factor of two as compared to the measurement. This result should not be too surprising, as both GRI mechanisms have been optimized for combustion of natural gas.

The measured fluorescence lifetimes are much larger than those reported for OH in similar flames (Pack et al., 1998a). In fact, the measured lifetime for the acetylene flame is outside the range for which our system has been calibrated (Pack et al., 1998b). On this basis, the acetylene lifetime has significant uncertainty based on the calibration procedure. The measured fluorescence lifetimes are shown in Figure 6, along with predicted lifetimes using the quenching cross sections of Tamura et al. (1998). Considering the paucity of measurements supporting the available cross sections and the prior lack of comparisons to

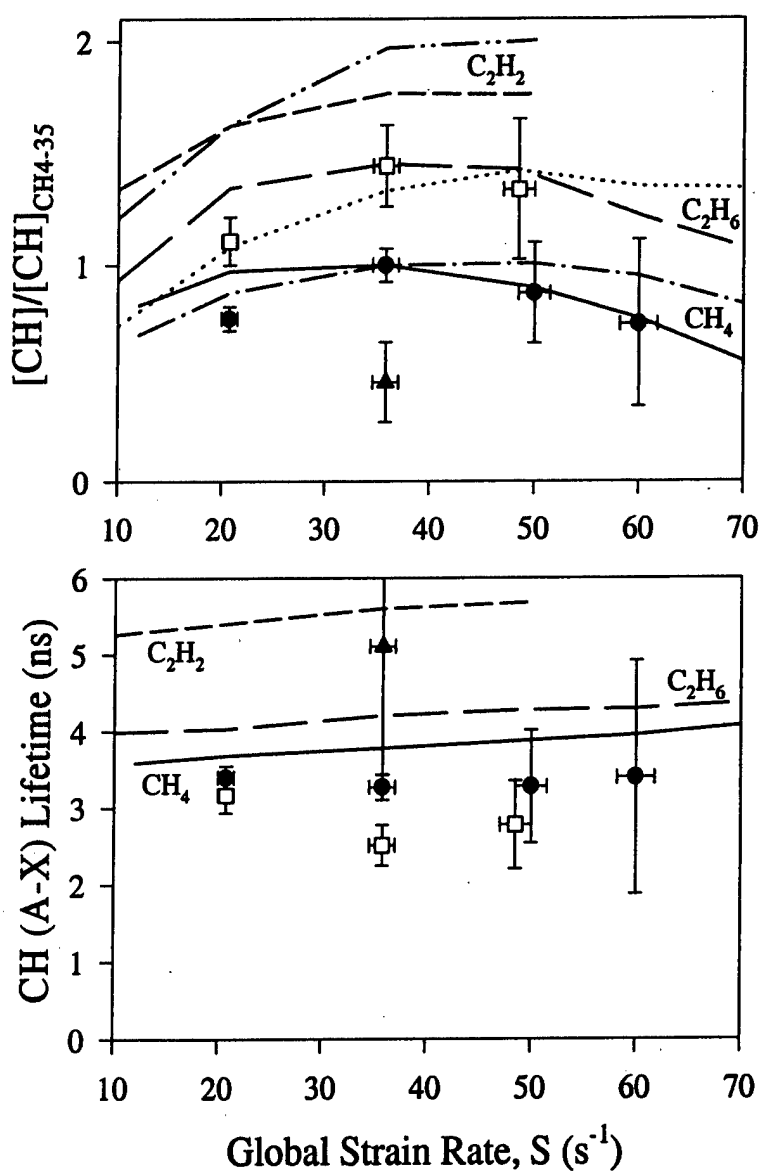


Figure 6. Relative peak CH concentrations and fluorescence lifetimes compared to GRI-3.0 and GRI-2.11 predictions. The CH concentrations are normalized by the peak CH value in the methane flame at $S=35 \text{ s}^{-1}$. Only the predictions for GRI-3.0 are shown for the fluorescence lifetimes, as the two predictions are nearly identical. Methane: ● (measured), — (GRI-3.0), - - - - (GRI-2.11); Ethane: □ (measured), - - - (GRI-3.0), ····· (GRI-2.11); Acetylene: ▲ (measured), - - - - (GRI 3.0), ····· (GRI-2.11).

measurements in atmospheric-pressure flames, the predicted lifetimes are in relatively good agreement with the measured lifetimes. In particular, the predictions are only 10–15% larger than the measurements for the methane and acetylene flames, which is acceptable when considering the scale of other measurement errors. However, the predicted lifetimes are 50% larger than the measurements for the ethane flames, which is unacceptably large for detailed comparisons to kinetic modeling or for calibration of CH fluorescence measurements. The numerical uncertainties for the fluorescence lifetimes based on the extreme compositions for the experimental boundary conditions are $\pm 5\%$ for the methane and ethane flames and $\pm 12\%$ for the acetylene flame. Including all sources of measurement error, the fluorescence lifetimes are still predicted to be higher than the measured lifetimes (except for acetylene where the total uncertainty is too large to permit detailed comparisons of predictions to measurements).

For both the methane and ethane cases, only nitrogen and water vapor contribute more than 10% to the total quenching rate coefficient, so it is likely that one of these two cross sections is slightly low (possible errors for these two colliders are discussed by Tamura et al., 1998). Nitrogen would appear to be the best target for improvement since it is the only collider that could cause a change sufficient to bring the ethane predictions in agreement with the measurements. However, nitrogen is predicted to contribute 68% to the total quenching rate coefficient for both the methane and ethane flames, so a drastic change in the nitrogen cross section would cause the methane prediction to become much worse. On the other hand, the temperatures for these flames differ, averaging 1690, 1600, and 1430 K for the CH₄, C₂H₆, and C₂H₂ flames, respectively. Thus, a correction to the temperature coefficient for the nitrogen cross section may bring all of these predictions into agreement with the measurements. We estimate that such a modification would require an N₂ cross section temperature dependence of only $T^{3.1}$ instead of the current $T^{2.9}$. Our measurements are not sufficiently comprehensive to determine this exponent or to suggest a specific change, and, in fact, insufficient high temperature data currently exist in the literature to accurately determine this exponent (Tamura et al., 1998). Clearly, high temperature cross-section data for CH/N₂ collisions would be of value in improving this cross-section correlation.

For a single flame, the variation in quenching cross sections with axial location is a negligible source of error in measuring the

concentration profiles (largely since CH exists in such a narrow spatial range). Figure 7 shows profiles of CH lifetimes normalized by their values at the radial location of peak (CH). For $-0.5 < \Gamma < 0.5$ (within a half-width of the peak concentration), the lifetime is constant within 10%. Outside of this range, the lifetimes may be varying by as much as 50%, but the measurement uncertainty is also very large. At the same time, the concentration is dropping rapidly (see Figure 5) so that the lifetime variation has little effect on the shape of the CH profile. Among the three different fuels, however, the changes in fluorescence lifetime are substantial and must be considered when making relative concentration measurements.

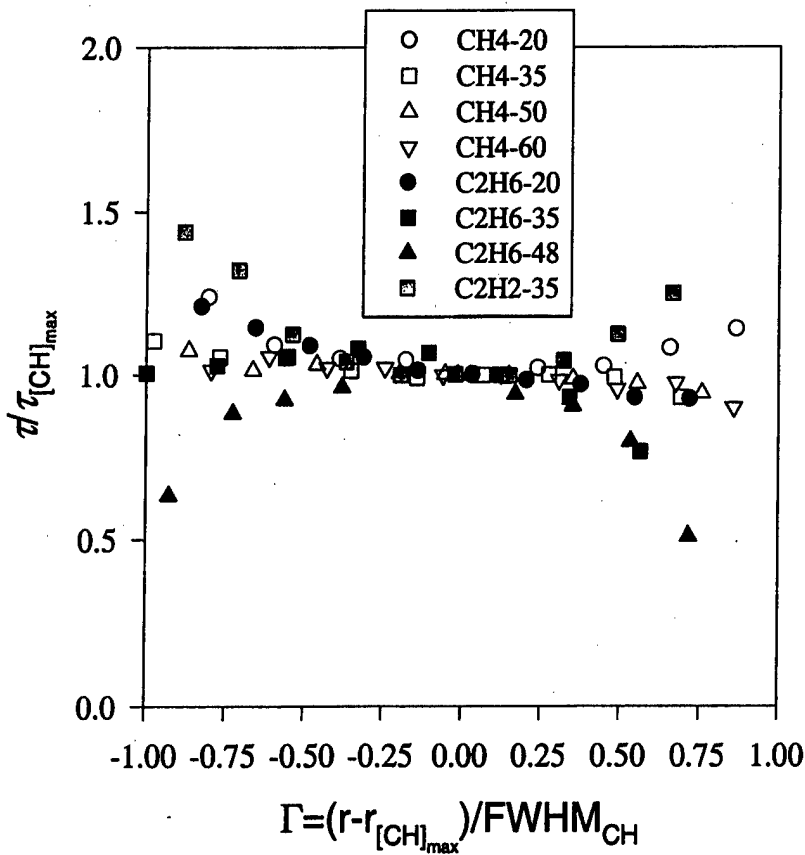


Figure 7. Axial profiles of CH fluorescence lifetimes in the eight test flames.

CONCLUSIONS

Measurements of relative CH concentrations have been reported for eight counterflow diffusion flames consisting of nitrogen-diluted methane, ethane, or acetylene at various strain rates. Fluorescence lifetimes have also been measured using a gated photon counting system after excitation with a picosecond laser. Predictions of these same quantities using OPPDIF (Lutz et al., 1996) are compared to the appropriate measurements. To our knowledge, this study is the first comparison of predicted CH lifetimes to direct measurements in atmospheric pressure flames. The following conclusions can be made:

1. The variation in fluorescence lifetimes among the various fuels is significant and must be considered to determine quantitative CH concentrations. However, in a single flame, the CH concentration profile can be measured without recourse to quenching corrections.
2. The measured lifetimes are much larger than for previous OH measurements, and the largest lifetimes from the acetylene flame have increased uncertainty because of an extrapolated calibration. Even for the other flames with lifetimes within the calibrated range, significant uncertainty exists in the measurements because of poor signal-to-background ratios. For this reason, the CH concentrations are also relatively uncertain. However, an alternate technique for determining the CH concentrations has been proposed that uses two gated photon counting bins in a manner that is significantly less susceptible to variations in the quenching rate coefficient for the range of lifetimes observed in these flames. These measurements of the CH concentration are nearly identical to the original estimates but with errors of less than 10% (95% confidence interval).
3. Within the uncertainties of the present measurements (and without an absolute calibration), both the GRI-3.0 and GRI-2.11 mechanisms provide good predictions of the relative CH concentrations in the methane and ethane flames but not in the acetylene flame. In the latter case, the predicted relative concentration is too large by at least a factor of two as compared to the methane flame.
4. The predicted fluorescence lifetimes are relatively close to the measurements in the acetylene and methane flames when considering the sparse treatment of CH quenching in the literature. However, the predictions in the ethane flames are too large by as much as 50%. An

error analysis indicates that improved predictions require an accurate determination of the temperature dependence of the CH/N₂ cross section.

ACKNOWLEDGEMENTS

This research was sponsored in part by the Air Force Office of Scientific Research, with Dr. Julain Tishkoff serving as technical monitor.

REFERENCES

- Berg, P. A., D. A. Hill, A. R. Noble, G. P. Smith, J. B. Jeffries, and D. R. Crosley. 2000. Absolute CH concentration measurements in low-pressure methane flames: Comparisons with model results. *Combust. Flame* 121:223.
- Bowman, C. T., R. K. Hanson, D. F. Davidson, W. C. Gardiner Jr., V. Lissianski, G. P. Smith, D. M. Golden, M. Frenklach, and M. Goldenberg. 1995. GRI Mechanism, version 2.11. http://www.me.berkeley.edu/gri_mech/.
- Carter, C. D., J. M. Donbar, and J. F. Driscoll. 1998. Simultaneous CH planar laser-induced fluorescence and particle imaging velocimetry in turbulent nonpremixed flames. *Appl. Phys. B* 66:129.
- Derzya, I., V. A. Lozovskya, and S. Cheskisa. 1999. Absolute CH concentration in flames measured by cavity ring-down spectroscopy. *Chem. Phys. Lett.* 306:319.
- Garland, N. L., and D. R. Crosley. 1986. On the collisional quenching of electronically excited OH, NH and CH in flames. *Proc. Combust. Inst.* 21:1693.
- Heinrich, P., and F. Stuhl. 1995. Electronic quenching of CH(A²) and NH(A₃) between 300 and 950 K. *Chem. Phys.* 199:105.
- Joklik, R. G., J. W. Daily, and W. J. Pitz. 1986. Measurements of CH radical concentrations in an acetylene/oxygen flame and comparisons to modeling calculations. *Proc. Combust. Inst.* 21:895.
- Luque, J., and D. R. Crosley. 1996. Absolute CH concentrations in low-pressure flames measured with laser-induced fluorescence. *Appl. Phys. B* 63:91.
- Luque, J., J. B. Jeffries, G. P. Smith, D. R. Crosley, K. T. Walsh, M. B. Long, and M. D. Smooke. 2000. CH(A-X) and OH(A-X) optical emission in an axisymmetric laminar diffusion flame. *Combust. Flame* 122:172.
- Lutz, A. E., R. J. Kee, and J. F. Grcar. 1996. OPPDIF: A FORTRAN program for computing opposed-flow diffusion flames. Sandia National Laboratories Report SAND96-8243.
- Mercier, X., P. Jamette, J. F. Pauwels, and P. Desgroux. 1999. Absolute CH concentration measurements by cavity ring-down spectroscopy in an atmospheric diffusion flame. *Chem. Phys. Lett.* 305:334.

- Pack, S. D., M. W. Renfro, G. B. King, and N. M. Laurendeau, 1998b. Laser-induced fluorescence triple-integration method applied to hydroxyl concentration and fluorescence lifetime measurements. *Combust. Sci. Tech.* 140:405.
- Pack, S. D., M. W. Renfro, G. B. King, and N. M. Laurendeau. 1998a. Photon-counting technique for rapid fluorescence-decay measurement. *Opt. Lett.* 23:1215.
- Ravikrishna, R. V., and N. M. Laurendeau. 2000. Laser-induced fluorescence measurements and modeling of nitric oxide in methane-air and ethane-air counterflow diffusion flames. *Combust. Flame* 120:372.
- Renfro, M. W., G. B. King, and N. M. Laurendeau. 2000. Scalar time-series measurements in turbulent $\text{CH}_4/\text{H}_2/\text{N}_2$ nonpremixed flames: CH. *Combust. Flame* 122:139.
- Renfro, M. W., S. D. Pack, G. B. King, and N. M. Laurendeau. 1999. A pulse-pileup correction procedure for rapid measurements of hydroxyl concentrations using picosecond time-resolved laser-induced fluorescence. *Appl. Phys. B* 69:137.
- Salmon, J. T., and N. M. Laurendeau. 1985. Calibration of laser-saturated fluorescence measurements using Rayleigh-scattering. *Appl. Opt.* 24:65.
- Seitzman, J. M. 1991. Quantitative applications of fluorescence imaging in combustion. Ph.D. Thesis, Stanford University, Palo Alto, CA.
- Smith, G. P., D. M. Golden, M. Frenklach, N. W. Moriarty, B. Eiteneer, M. Goldenberg, C. T. Bowman, R. Hanson, S. Song, W. C. Gardiner Jr., V. Lissianski, and Z. Qin. 1999. GRI Mechanism, version 3.0. http://www.me.berkeley.edu/gri_mech/
- Tamura, M., P. A. Berg, J. E. Harrington, J. Luque, J. B. Jeffries, G. P. Smith, and D. R. Crosley. 1998. Collisional quenching of CH(A), OH(A), and NO(A) in low pressure hydrocarbon flames. *Combust. Flame* 114:502.
- Woiki, D., M. Votsmeier, D. F. Davithon, R. K. Hanson, and C. T. Bowman. 1998. CH-radical concentration measurements in fuel-rich $\text{CH}_4/\text{O}_2/\text{Ar}$ and $\text{CH}_4/\text{O}_2/\text{NO}/\text{Ar}$ mixtures behind shock waves. *Combust. Flame* 113:624.

Scalar Time-Series Simulations Using Flamelet State Relationships for Turbulent Non-premixed Flames

MICHAEL W. RENFRO*, JAY P. GORE, and NORMAND M. LAURENDEAU

School of Mechanical Engineering, Purdue University, West Lafayette, IN 47907-1288, USA

Simulations of scalar (OH, CH, and number density) time series and comparisons to experimental data are presented using a laminar flamelet model. Realistic time series for mixture fraction (Z) were constructed by employing measured Z mean and rms values in conjunction with realistic power spectral densities (PSDs), probability density functions (PDFs), and integral time scales. A unique procedure was implemented to permit simultaneous specification of both the PSD and PDF shapes for Z . These Z time series were mapped to other scalar time series by using flamelet state relationships from a strained laminar flame code. The simulated statistics are compared to recent data in hydrogen/methane/nitrogen flames. The predictions of OH and CH time scales directly depend on the time scale for Z ; however, they are not identical because of the narrow state relationships for reactive scalars. The model successfully captures complicated features in the radial distribution of OH integral time scales. In a separate inverse calculation, the simulation is used to estimate Z time scales from each of the measured OH, CH, and number density data. In each case the Z time scale is found to be ~ 0.75 ms on the jet centerline. In contrast to time scales from non-reacting jet studies, this Z time scale is nearly invariant with axial height and at low axial heights varies only slowly with radial location, implying that convective scaling (jet width/local velocity) may be insufficient for the accurate description of mixing time scales in jets with heat release. © 2002 by The Combustion Institute

NOMENCLATURE

C	constant
CDF	cumulative distribution function
D	burner diameter (mm)
f	frequency (Hz)
N	number of time-series points
n	number density (cm^{-3})
PDF	probability density function
PSD	power spectral density (s)
r	radius (mm)
s	time delay (ms)
S	Global strain rate (s^{-1})
T	sampling time (s)
t	time (s)
U	mean axial velocity (m/s)
x	axial height (mm)
Z	mixture fraction

Greek

Φ	phase spectrum (rad)
Γ	normalized radial coordinate
ρ	autocorrelation coefficient
τ_I	integral time scale (ms)

Subscripts

CL	centerline value
o	jet exit value
1/2	half-width-at-half-maximum

INTRODUCTION

Quantitative time-series measurements of temperature and velocity in turbulent flames have been available for many years via Rayleigh scattering [1] and laser Doppler velocimetry [2], respectively. Recently, time series for minor-species concentrations have also been demonstrated using picosecond time-resolved laser-induced fluorescence (PITLIF) at sampling rates up to 40 kHz [3, 4]. These techniques provide unique information on the time scales of velocity and scalar fluctuations and on the distribution of these fluctuations as a function of frequency. Similar information is not available from typical "single-shot" diagnostics [5, 6]. Although single-shot techniques are ideal for determining probability density functions (PDFs) owing to their high signal-to-noise ratios, all time-correlation information is discarded by the low repetition rate of the measurement.

In non-reacting, turbulent flows, scaling laws

*Corresponding author. E-mail: renfro@ecn.purdue.edu

than that on the fuel side. In general, OPPDIF simulations show that the above differences are consistent with a drop of only 30 to 60 K in the peak flame temperature, which is certainly in agreement with expectation when accounting for soot radiation [5].

CONCLUSIONS

Quantitative LSF measurements of [NO] have been obtained along the centerline in laminar, counter-flow, CH_4/O_2 diffusion flames at atmospheric pressure by varying the N_2 content in both the oxidizer and fuel streams under sooting high-temperature oxy-fuel conditions. Comparisons of these measurements with predictions from OPPDIF indicate good agreement in those regions of the flames for which the temperatures are below 2600 K. Excellent spatial agreement also occurs because of dominance by the well-known thermal mechanism. Enhanced radiative heat loss caused by soot formation leads to poorer agreement between predicted and measured NO concentrations in regions at higher flame temperatures ($T > 2600$ K). Therefore, a model considering the effect of increased radiative heat loss owing to soot formation is necessary to more accurately model oxy-fuel flames. The LSF measurements also indicate that laser-saturated fluorescence can be used in high temperature environments such as oxy-fuel combustion. The selected excitation and detection strategy avoids interferences from other species and no significant change in background is observed even under sooting, high-temperature conditions.

REFERENCES

1. Eleazer, P. B., and Slavejkov, A. G., *Ceram. Eng. Sci. Proc.* 15:159 (1994).
2. Schroeder, R. N., and Zak, A. E., *Ceram. Eng. Sci. Proc.* 17:162 (1996).
3. Baukal, Jr., C. E., *Oxygen Enhanced Combustion*. CRC Press (1999).
4. Megaridis, C. M., Lee, K.-O., Zelepouga, S., Saveliev, A. V., Kennedy, L. A., Charon, O., and Ammouri, F., *Combust. Flame* 121:323 (2000).
5. Beltrame, A., Porshnev, P., Merchan-Merchan, W., Saveliev, A., Fridman, A., Kennedy, L. A., Petrova, O., Zhdanok, S., Ammouri, F., and Charon, O., *Combust. Flame* 124:295 (2001).
6. Al-Chalabi, R., Schatz, C., Yap, L., and Marshall, R., *Ceram. Eng. Sci. Proc.* 16:202 (1995).
7. Hedley, J. T., Pourkashanian, M., and Yap, L. T., *Combust. Sci. Technol.* 108:311 (1995).
8. Lin, K. C., and Faeth, G. M., *J. Prop. Power* 12:10 (1996).
9. Baukal, Jr., C. E., *Heat Transfer in Industrial Combustion*. CRC Press (2000).
10. Kuligowski, F. F., and Laurendeau, N. M., *Combust. Sci. Technol.* 130:423 (1997).
11. Sung, C. J., and Law, C. K., *Proc. Comb. Inst.* 27:1411-1418 (1998).
12. Naik, S. V., and Laurendeau, N. M., Submitted to *Combust. Sci. Tech.* (2001); also Naik, S. V., *Laser-induced Fluorescence Measurements and Modeling of Nitric Oxide in Oxygen-enriched, Laminar Counter-flow Diffusion Flames*, M. S. Thesis, School of Mechanical Engineering, Purdue University, West Lafayette, IN (2000).
13. Reisel, J. R., and Laurendeau, N. M., *Combust. Sci. Tech.* 98:137 (1994).
14. Cooper, C. S., and Laurendeau, N. M., *Meas. Sci. Technol.* 11:902 (2000).
15. Thomsen, D. D., and Laurendeau, N. M., *Combust. Flame* 124:350 (2001).
16. Cooper, C. S., and Laurendeau, N. M., *Applied Optics* 36:5262 (1997).
17. Harris, J. M., Lytle, F. E., and McCain, T. C., *Anal. Chem.* 48:2095 (1976).
18. Vora, N. A., *Flame Suppression Activity via Laser-induced Fluorescence Measurements and Modeling of Hydroxyl Concentration in Opposed CH_4 -Air Diffusion Flames*, M. S. Thesis, School of Mechanical Engineering, Purdue University, West Lafayette, IN (2000).
19. Magre, P., Aguerre, F., Collin, G., Versaev, P., Lacas, F., and Rolon, J. C., *Exp. Fluids* 18:376 (1995).
20. Reisel, J. R., Carter, C. D., Laurendeau, N. M., and Drake, M. C. *Combust. Sci. Tech.* 91:271 (1993).
21. Lutz, A. E., Kee, R. J., and Grcar, J. F., *OPPDIF: A Fortran Program for Computing Opposed-flow Diffusion Flames*, Sandia National Laboratories Report No. SAND96-8243 (1996).
22. Kee, R. J., Miller, J. A., Evans, G. H., and Dixon-Lewis, G., *Proc. Combust. Inst.* 22:1479-1494 (1998).
23. Bowman, C. T., Hanson, R. K., Davidson, D. F., Gardiner, Jr., W. P., Lissianski, V., Smith, G. P., Golden, D. M., Frenklach, M., and Goldenberg, M., (1999). http://www.me.berkeley.edu/gri_mech/.
24. Kee, R. J., Grcar, J. F., Smooke, M. D., and Miller, J. A., *A Fortran Program for Modeling Steady Laminar One-Dimensional Premixed Flames*, Sandia National Laboratories Report No. SAND85-8240 (1985).
25. Gore, J. P., Lim, J., Takeno, T., and Zhu, X. L., *A Study of the Effect of Thermal Radiation on the Structure of Methane-Air Counter-flow Diffusion Flames using detailed Chem. Kinetics*, Proceedings of the Fifth ASME/JSME Joint Thermal Engineering Conference, San Diego, CA. Paper AJTE99-6311 (1999).

have been successfully developed to relate fluctuation time scales to mean flow properties [7, 8]. Moreover, theoretical solutions to the frequency distribution of turbulent fluctuations (given by the power spectral density, PSD, and its well-known slope of $-5/3$ in the inertial subrange) have been found to be in agreement with experimental results under ideal conditions [9]. Unfortunately, this success with simple scaling does not transfer to flows with heat release, for which the PSDs deviate from the $-5/3$ slope for both velocity [2] and scalars [10]. Very little work has investigated this aspect of chemistry-turbulence interactions on the PSD or on the integral time scale [11]. Therefore, the general behavior of turbulent fluctuations in reacting flows remains an area for continued research.

The ability to understand and predict time-series behavior has applications to the evaluation and improvement of models for turbulent combustion, and to studies of fast transient phenomena such as extinction, reignition, and combustion instability. Developing this understanding is complicated by the fact that species concentrations depend on the mixture fraction, temperature, and scalar dissipation rate so that the interrelated fluctuations of velocity, mixture fraction, and temperature must be understood. A possible simplification for non-premixed flames suggested by analysis of our minor-species data are that scalar fluctuations are sufficiently dominated by the convective motion of relatively thin reaction zones that only information on mixture fraction fluctuations is necessary to predict fluctuations for other scalars in the flow [3, 4, 10]. This independence from diffusion effects may occur because the PSD is dominated by lower-frequency fluctuations occurring at larger spatial and temporal scales. Thus, even if a laminar flamelet approach is insufficient for prediction of instantaneous values for scalars (their PDFs) because of turbulence-chemistry interactions, this tactic may still be sufficient for predictions of PSDs and time scales. This potential simplification is examined in this paper by comparing predicted and measured time scales using one-dimensional state relationships.

A simple laminar-flamelet stochastic simulation for predicting time series of minor-species concentrations was presented previously by

Renfro et al. [12] following the work of Kounalakis et al. [13]. This model used input mixture fraction (Z) statistics to simulate a Z time series, which was then mapped to a concentration time series via a one-dimensional flamelet state relationship obtained from a detailed kinetics simulation. However, the time-series construction was limited to a few arbitrary conditions and no quantitative comparison to data were attempted. The variation in integral time scales that occurs in jet flames was not accounted for and the PDF for mixture fraction was not controlled in these simulations. Nevertheless, a parametric study of the effects of \bar{Z} and Z_{rms} on the predicted concentration time series was completed with encouraging agreement to qualitative data available at that time [12].

The present paper builds on this prior work by (1) directly including the mixture fraction PDF and integral time scale in the time-series simulations, (2) using measured Z data to create realistic, yet synthetic, time series, and (3) comparing the resulting scalar simulations directly to measured trends from OH, CH, and newly reported number density (n) time-series data. Having completed the development of this technique, a separate inverse calculation using the simulation as a tool is presented to assess actual mixture fraction time scales in a series of turbulent jet flames. The motivation for this work is to gain a better understanding of measured OH and CH time scales and their complicated radial dependencies, to enhance our understanding of mixing time scales used in some turbulence models, and to improve time-series construction techniques, which may have application to time-dependent boundary condition construction for large-eddy or direct-numerical simulations.

Autoregressive techniques for creating time series from their statistics are addressed by Box et al. [14] and have been applied previously to combustion systems [13, 15, 16]; however, it is generally difficult to simultaneously specify both the PDF and PSD. We first present an efficient technique as compared to the autoregressive approach for performing this time-series construction. Next, various statistics for mixture fraction are considered as inputs to the time-series simulation. These are taken from recent measurements in a series of hydrogen/methane/

nitrogen flames. The sensitivity to these inputs is assessed with respect to the simulation's predictions of scalar time scales, and predictions of OH, CH, and n time scales are acquired using the most plausible Z inputs. The scalar predictions are compared to quantitative data obtained using PTLIF for OH and CH [3, 4], and to data for number density acquired via laser Rayleigh scattering [17].

TIME-SERIES SIMULATION TECHNIQUE

The time-series simulation can be understood by examining which statistics are necessary to specify all of the information in a general time series. Consider a discrete times series for mixture fraction, $Z(t_i)$, which contains N data points, has a sampling-time interval of $\Delta t = t_{i+1} - t_i$, and therefore has a total sampling time of $T = \Delta t N$. The PSD for this series is

$$PSD_Z(f_i) = \frac{|\mathfrak{S}\{Z(t_i) - \bar{Z}\}|^2}{Z'^2}, \quad (1)$$

where $\mathfrak{S}\{Z(t)\}$ represents a complex Fourier transform and Z'^2 is the variance of Z . The PSD is defined from $f_{\min} = 1/T$ to $f_{\max} = 1/2\Delta t$, with $\Delta f = 1/T$; thus, the discrete PSD contains $N/2$ points. The autocorrelation function of $Z(t_i)$ contains the same information as the PSD, but in the time domain; that is,

$$\begin{aligned} \rho_Z(s) &= \frac{\overline{(Z(t_i) - \bar{Z})(Z(t_i + s) - \bar{Z})}}{Z'^2} \\ &= \mathfrak{S}^{-1}\{PSD_Z(f_i)\}, \end{aligned} \quad (2)$$

where s is the time delay between points in the time series. Often the entire frequency distribution of fluctuations given by the PSD is not as important as a single "fluctuation rate." Many time scales can be defined, but one very common definition is the integral time scale, which is given by

$$\tau_{i,Z} = \int_0^{\infty} \rho_Z(s) ds. \quad (3)$$

This definition assumes a continuous and infinite time series. For discrete data the integral is replaced by a summation from $s = 0$ to s_{\max}

which is chosen to be large enough to encompass the relevant information in the autocorrelation function. It is important to note that the integral time scale is a sufficient time scale only when the PSD or autocorrelation function has a shape that can be described with one parameter, such as an exponential decay. More complicated shapes have been experimentally observed (e.g., the fuel-side CH PSDs of Renfro et al. [4]), and in such cases, the integral time scale is not sufficient for characterizing the "fluctuation rate."

Because the PSD and the autocorrelation function are defined from the magnitude of the complex Fourier transform, all phase information is discarded. Therefore, the PSD (or ρ) only specifies the intensity of fluctuations as a function of frequency (or time delay) and contains no information on the distribution of mixture fraction values in the time series. A phase spectrum, $\Phi(f_i)$, which varies for each time series, can also be computed from the complex Fourier transform, and together with the PSD, mean, and rms, fully specifies the parent time series. The PDF, simply a normalized histogram of $Z(t_i)$, also contains information on the distribution of Z values in the time series. However, differences in Z smaller than the PDF bin width are ignored so that the PDF contains a smaller number of points (typically $\sim N/100$ points) compared to a phase spectrum. Thus, a time series (N points) characterized by only its PSD ($N/2$ points) and PDF ($N/100$ points) is always under-specified.

The approach of the present simulations is to assume values for certain critical mixture fraction statistics and to construct a realistic $Z(t_i)$ for a single point in the flame. We choose to use the PDF and PSD as significant information is available concerning these statistics, although the resulting time series are underspecified and some assumptions must be made to complete the simulation. By using this approach, the synthetic time series will have the correct frequency content and the correct range of instantaneous values. While the PDF directly contains the mean and rms as its first two moments, and the PSD directly contains the integral time scale, it is convenient to specify only normalized PSD and PDF shapes. The mean, rms, and integral time scale must then be specified sepa-

rately. For the PSD this normalization is accomplished by

$$PSD_Z(f\tau_{I,Z}) = \frac{|\mathfrak{I}\{Z(t_i/\tau_{I,Z}) - \bar{Z}\}|^2}{Z'^2} = \frac{PSD_Z(f)}{\tau_{I,Z}} \quad (4)$$

For the PDF, standard shapes that have only the mean and rms as parameters are considered, such as the clipped Gaussian or the Beta-PDF. This choice of PDF shape has been found to have little impact on previous scalar simulations [15].

The time-series construction proceeds as follows. An initial Z time series, Z_1 , is constructed via

$$Z_1(t_i) = \bar{Z} + \mathfrak{I}^{-1} \left\{ \sqrt{\frac{PSD_Z(f_i\tau_{I,Z})}{Z'^2}} \times e^{i\Phi(f_i)} \right\}, \quad (5)$$

The sampling rate and sampling time of the synthetic time series depends directly on the input PSD resolution and range. For the present simulations, each time series contains between 1,048 and 8,192 points. The phases of the fluctuation frequencies, $\Phi(f_i)$, are chosen by random number generation so that each simulated time series is unique, while maintaining the required mean, rms, PSD shape, and integral time scale. This procedure yields a nearly Gaussian PDF for the synthetic time series, $PDF_1(\alpha)$, including some values greater than one and less than zero.

An iterative mapping procedure is used next to force the time series to match the chosen PDF shape. The cumulative distribution function (CDF) of the simulated time series is computed from its PDF as

$$CDF_1(\gamma) = \sum_{\alpha=-\infty}^{\gamma} PDF_1(\alpha) \cdot \Delta\alpha, \quad (6)$$

where α and γ are sample-space variables. The desired CDF, $CDF_Z(\gamma)$, is also computed from the specified PDF_Z . This discrete function is then inverted (CDF_Z^{-1}) and the synthetic time series is mapped to force its distribution to equal the specified PDF, via

$$Z_2(t_i) = CDF_Z^{-1}\{CDF_1[Z_1(t_i)]\}. \quad (7)$$

In essence, the initial simulated time series has been constructed without regard for its PDF and then stretched to match the desired PDF shape. Although only a clipped-Gaussian or Beta-PDF have been used in the present simulations, there are no foreseen limitations on this shape. This procedure affects the PSD shape so that the frequency content of the mapped time series yields $PSD_2(f)$. Hence, the effect of the map on frequency content is $PSD_2(f)/PSD_Z(f)$. To correct for this undesired alteration to the PSD, a third spectrum is computed as

$$PSD_3 = PSD_Z \times \frac{PSD_Z}{PSD_2}, \quad (8)$$

which is used as a new input to the time series simulation in Eq. 5. This procedure must be repeated a few times until the mapped time series is indeed found to have both the desired PDF and PSD shapes. The average PSD computed from 50 simulated time series is usually within 0.1 decades of the desired PSD at all frequencies and the agreement between the desired and simulated PDFs is exact. This entire procedure can be repeated to create any number of simulated Z time series with arbitrary input conditions.

For comparison to OH, CH, and n data, the synthetic Z time series must be mapped, point-by-point, to other scalar time series by assigning a scalar value to each mixture fraction using a one dimensional flamelet state relationship, for example, OH(Z). The resulting scalar time series can then be used to compute the mean, rms, PSD, PDF, and integral time scale for OH, CH, or n . For each combination of input parameters, the entire simulation was repeated fifty times for the present results. The scalar statistics from the fifty simulations were then averaged to yield cleaner simulated statistics. Variations among simulations arise from changing the random generator seed for the phase relationships used in the simulations.

TIME-SERIES SIMULATION INPUTS

Using the procedures outlined in the previous section, the synthetic scalar time series were

TABLE 1

Experimental Results Available for the Flames Simulated in the Present Study

Data	Re	D (mm)	Heights (x/D)	Statistics Available	Reference
OH time series	2800	3.4 (flame A1)	1, 2, 5, 10, 20, 40, 60	Mean, rms, PDF, PSD, time scales	3
	5000	3.4 (flame A2)			
CH time series	9000	3.4 (flame A3)	1, 2, 5, 10	Mean, rms, PDF, PSD, time scales	4
	13,000	3.4 (flame A4)			
	15,200	3.4 (flame A5)			
<i>n</i> time series	9000	7.8 (x/D < 40)	5, 10, 20, 40, 60	Mean, rms, PDF, PSD, time scales	17
	15,200	7.8 (x/D < 40)			
Major species, T, Z	15,200	8 (flame DLR-A)	5, 10, 20, 40, 60, 80	Mean, rms, PDF	5
Major species, T, Z, OH, NO, CO	15,200	8 (flame DLR-A)	5, 10, 20, 40, 60, 80	Mean, rms, PDF	6
Velocity	22,800	8 (flame DLR-B)			
	15,200	8 (flame DLR-A)	0, 5, 10, 20, 40, 60, 80	Mean, rms	18

constructed to match the following pre-chosen input statistics:

1. Mean mixture fraction, \bar{Z}
2. Mixture fraction rms or variance, $\overline{Z'^2}$
3. Normalized mixture fraction PSD or auto-correlation function shape, $\text{PSD}_Z(f\tau_{1,Z})$
4. Mixture fraction integral time scale, $\tau_{1,Z}$
5. Mixture fraction PDF shape, PDF_Z
6. Scalar state relationship, for example, $[\text{OH}] = f(Z)$

We now examine realistic conditions for each of the six input parameters.

All simulations reported here are performed for a flame of 33.2% H₂, 22.1% CH₄, and 44.7% N₂ (by volume) burning in air. This standard flame was chosen because it is well documented in the literature. OH, CH, and *n* time-series measurements, using LIF and Rayleigh scattering, are available from Re = 2,800 to Re = 15,200 [3, 4, 17]. Single-shot major-species concentrations along with measurements of OH and NO are available for a Re = 15,200 and a Re = 22,800 flame [5, 6], and mean velocities are available for the same Re = 15,200 flame [18]. The related experimental data and flame configurations are summarized in Table 1. Lakshmanarao et al. [19] also present direct measurements of mixture fraction time scales in a non-reacting jet using acetone LIF with the same burner diameter and Reynolds number as the flame measurements of Renfro et al. [3]. A few measurements from this study are discussed with the results of the present simulations.

Because the experimental studies do not all use the same burner diameter, normalized coordinates (*r*/*x* and *x*/*D*) are employed to compare between the simulations and experiments. Furthermore, the most detailed time series data for OH and CH are available in only a Re = 9,000 flame (flame A3), so the results presented here focus on this condition. The effects of using measured data from a Re = 15,200 flame as inputs to the Re = 9,000 simulation will be discussed with the results. For the comparisons reported here, only axial heights of *x*/*D* = 10, 20, 40, and 60 are used as the time-series data at lower heights are strongly affected by laminarization [3, 4].

Mixture Fraction Mean and RMS

Self-similar radial profiles for \bar{Z} have been extensively studied in non-reacting jets [7, 8, 20] and are found to follow either a Gaussian profile,

$$\bar{Z} = Z_{CL} e^{-\ln(2)(r/r_{1/2})^2}, \quad (9)$$

or a slightly different polynomial profile of order (*r*/*x*)⁻⁴ [21],

$$\bar{Z} = \frac{Z_{CL}}{(1 + (\sqrt{2} - 1)(r/r_{1/2})^2)^2}. \quad (10)$$

In each case, Z_{CL} is the mixture fraction on the jet centerline and $r_{1/2}$ is the radial location where the mixture fraction has decreased to half of its centerline value. The mean velocity is also

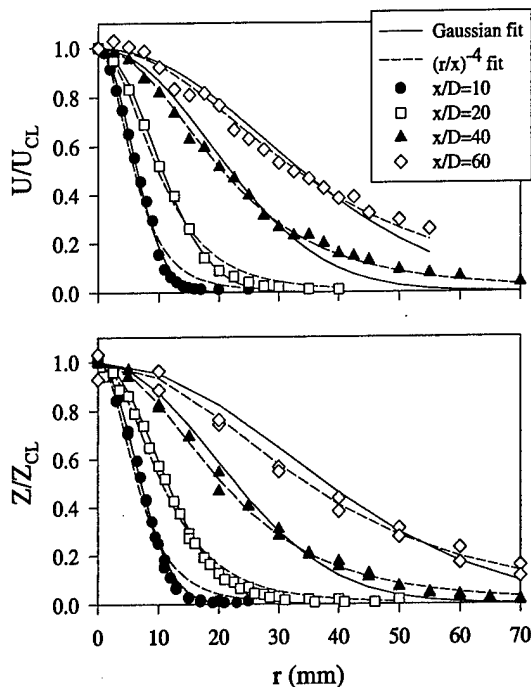


Fig. 1. Least-squares fit of Eq. 9 and Eq. 10 to the measured velocity data (top) of Schneider et al. [18] and to the measured mixture fraction data (bottom) of Meier et al. [6] and Bergmann et al. [5].

found to follow one of these forms at sufficiently large axial heights [22, 21]. Figure 1 shows curve fits for U/U_{CL} [18] and Z/Z_{CL} [5, 6] using both the Gaussian and $(r/x)^{-4}$ forms for axial heights of $x/D = 10, 20, 40,$ and 60 in flame DLR-A. At the two lower heights, the Gaussian fit (Eq. 9) best matches the data, while Eq. 10 provides the better fit at the two downstream locations. The parameters for each of these fits are given in Table 2 and are used for input (1) to the simulations. Bergmann et al. [5] and Meier et al. [6] also provide data for profiles of Z_{rms} . A sixth-order polynomial fit to these measured

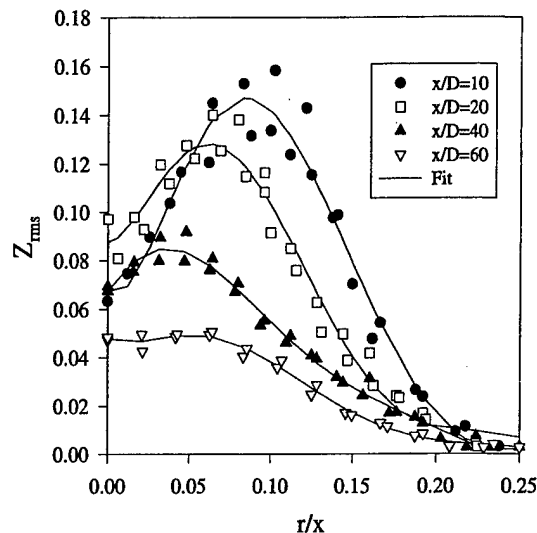


Fig. 2. Polynomial fits to the measured mixture fraction rms data of Meier et al. [6] and Bergmann et al. [5].

profiles, as shown in Fig. 2, was used for input (2) to the simulations.

Mixture Fraction PSD and PDF

For the mixture fraction PSD, measurements of Z time series in non-reacting [7, 8, 20] and reacting [11] jets suggest an autocorrelation function that is nearly exponential. Previous OH time series simulations [12] assumed a PSD that was flat for $f \leq 100$ Hz and had a slope of -2.0 at $f > 100$ Hz. These two cases are shown in Fig. 3 along with a composite PSD averaged over many OH measurements taken in our laboratory. When normalized as indicated above, all three cases are quite similar. In the present study, a PSD shape characterized by only the integral time scale is used for simplicity. More complicated multi-scale PSDs could be incorporated if necessary. For most of the sim-

TABLE 2

Coefficients for least-squares fit of Eq. 9 or Eq. 10 to the measured mixture fraction [5, 6] and velocity [18] data in flame DLR-A

x/D	Z best fit	Z_{CL}	$r_{1/2,Z}$ (mm)	U best fit	U_{CL} (m/s)	$r_{1/2,U}$ (mm)
10	Eq. 9	0.91	7.12	Eq. 9	45.90	6.44
20	Eq. 9	0.64	11.50	Eq. 9	33.33	10.71
40	Eq. 10	0.33	20.50	Eq. 10	17.98	20.81
60	Eq. 10	0.18	34.31	Eq. 10	11.40	33.03

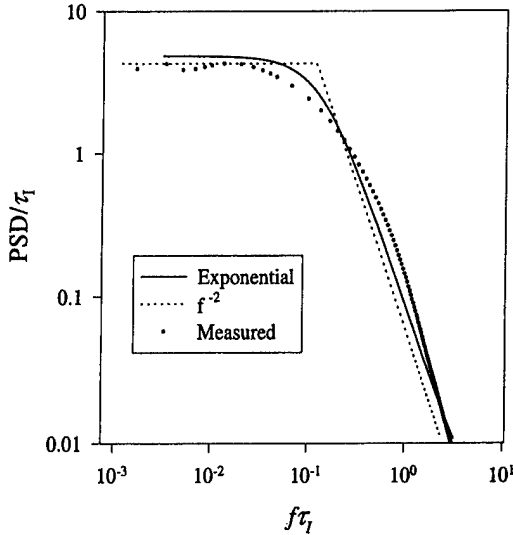


Fig. 3. Power spectral density shapes for the scalar time-series simulations. The exponential PSD refers to the shape of its autocorrelation function. The measured data are compiled from the OH measurements of Renfro et al. [4].

ulations considered here, the exponential autocorrelation shape is used for input (3). This shape is not expected to be realistic for small time delays (large frequencies) representative of diffusive scales. However, if convective fluctuations are dominant in determining scalar fluctuations, this limitation will be negligible.

Both a clipped Gaussian and a Beta PDF are considered for input (5) in the present simulations. These provide a range of Z distribution shapes that are similar to those observed experimentally [23, 24].

Mixture Fraction Integral Time Scale

The integral time scale for Z is the least documented of the six model inputs. In non-reacting jets, convective scaling has been found to be effective in describing the evolution of $\tau_{I,Z}$. On this basis, the integral time scale is proportional to the jet width divided by the local mean velocity [7]. In the self-similar region of a non-reacting jet, the jet width and the inverse of the centerline velocity are both proportional to the axial height, thus

$$\tau_{I,Z} \sim \frac{r_{1/2,U}(x)}{U(r,x)} = C \frac{x^2}{DU_0 f(r/x)}, \quad (11)$$

where U_0 is the jet exit velocity, $f(r/x)$ is a dimensionless function describing the self-similar radial velocity distribution, D is the burner diameter, and C is a dimensionless proportionality constant. In support of Eq. 11, Birch et al. [7] find an x^2 dependence for $\tau_{I,Z}$ in a non-reacting methane jet; however, the more recent data of Pitts and Kashiwagi [20] show a linear dependence (with considerable scatter). This discrepancy may be caused by differences in the virtual origin of the experimental jets. In particular, the time-scale data of Pitts and Kashiwagi [20] focuses on axial heights of $x/D < 30$. Over this relatively small range, the difference in x^1 and x^2 scaling can be masked by an offset in the origin of x . However, if the velocity and mixture fraction profiles are assumed to be similar (velocity was not measured), both data sets display time scales that are approximately $0.4 \times r_{1/2,U}(x)/U_{CL}$. Hence, convective scaling may still hold for the mixture fraction time scales, and the apparent discrepancy in axial height scaling may only be caused by the scaling of the jet width in the near field.

The convective scaling of Eq. 11 has also been attempted in jet flames [11] with some success, but the limited range of available data precludes a conclusive determination of the $\tau_{I,Z}$ profile and its dependence on x . For the measured U and Z profiles discussed above, an estimate for the evolution in time scales can be made by considering the axial dependence of both the centerline values and the profile widths. These data sets are shown in Fig. 4, both of which suggest a time scale (width/mean) growth rate of less than x^2 . From the velocity data a best fit yields $r_{1/2,U}/U_{CL} \sim (x/D)^{1.70}$ while the mixture fraction data are best fit by $r_{1/2,Z}/Z_{CL} \sim (x/D)^{1.85}$. For input (4) to the simulation, the measured velocities of Schneider et al. [18] were used with Eq. 11, but this feature is examined further with the results. It is important to note that insufficient data exist to predict the proportionality constant, C , for jets with heat release. Hence, it is not possible to quantitatively predict the Z time scale.

Scalar State Relationships

The scalar state relationships used as input (6) are specified via predictions of the OPPDIF

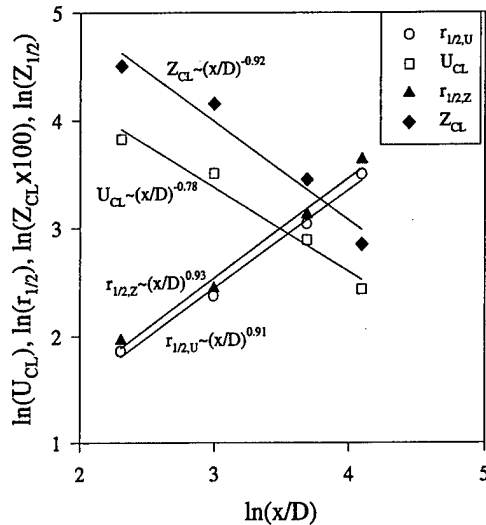


Fig. 4. Power-law fits to the peak and half-width-at-half-maximum values for velocity and mixture fraction taken from the curve fits of Fig. 1.

flame code [25] using GRI-Mech 2.11 [26] for OH, CH, and n . The state relationships were computed for the experimental fuel mixture over a wide range of strain rates, S . Several plausible state relationships were examined, but results are presented for only a single global strain rate of 100 s^{-1} as shown in Fig. 5. For this

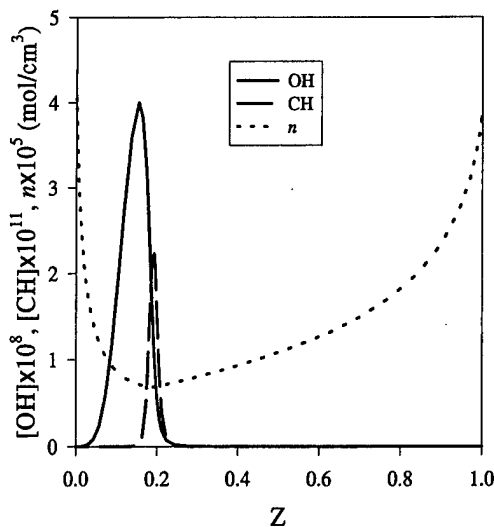


Fig. 5. Input state relationships for OH, CH, and number density used in the scalar time-series simulations. These relationships were computed at a global strain rate of 100 s^{-1} using OPPDIF [25] and GRI-Mech 2.11 [26] with variable Le and fixed $Sc = 0.75$ for all species.

case, the mass diffusivity for each species was set via $Sc = 0.75$ while the thermal diffusivity (Le) was calculated from the fluid composition. This procedure was found to best match experimental state relationships for major-species concentrations, as differential diffusion is attenuated sufficiently far downstream [5]. This procedure also provides approximately the correct location and width (in Z coordinates) for the OH state relationship as compared to the data of Meier et al. [6]. Hence, one-dimensional state relationships corresponding to $S = 100 \text{ s}^{-1}$ were used for simulations at all locations in the flame. Several other state relationships were created by varying Sc/Le ratios and by permitting differential diffusion in the OPPDIF calculations. However, as discussed with the results, these changes had only minimal effects on the time scale simulations.

RESULTS

The prediction of the scalar mean, rms, and PDF via this time-series technique is no different than that which would be achieved by an assumed PDF approach with no concern for the mixture fraction PSD or time scale. This agreement occurs because the mean and rms for the simulated scalar are computed from only the scalar PDF, which is defined by only the Z PDF and the scalar state relationship. For this reason, we focus on the prediction of statistics unique to the full time-series simulation, in particular the scalar time scales and PSDs. A sample time series for Z and OH is shown in Fig. 6, as simulated for $r/x = 0.1$ and $x/D = 20$ (near the peak mean OH concentration) at $Re = 9,000$. Unless otherwise stated, an exponential autocorrelation function and a Beta PDF are used for all of the simulations shown here. Two reference lines on the Z time series show the limits ($Z = 0.06-0.20$) beyond which negligible OH exists (based on the state relationship used). The limited range of Z values for which appreciable OH exists causes several important differences between the Z and OH time series. First, the Z time series contains fluctuations outside the range $Z = 0.06$ to 0.20 that are completely nonexistent in the scalar time series (an example is marked at position A in Fig. 6).

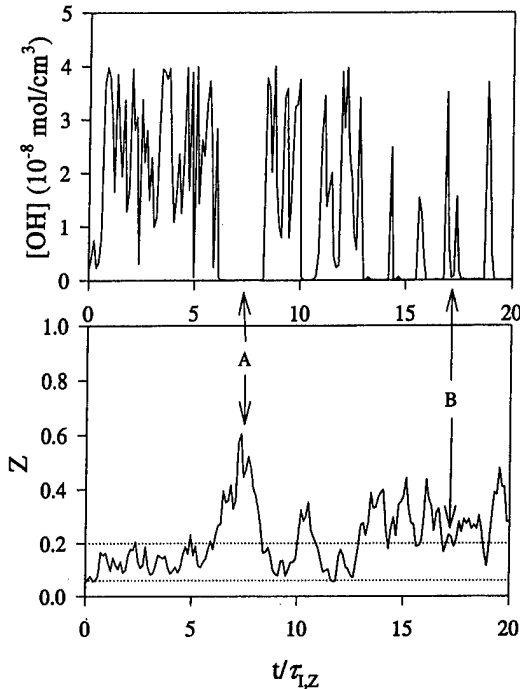


Fig. 6. Sample simulated time series for OH and Z at $r/x = 0.1$, $x/D = 20$, $Re = 9,000$, $\tau_{i,z} = 9.7$ ms. The simulations utilize a Beta Z PDF and an exponential Z autocorrelation function for the PSD. Regions of scalar intermittency (A) and enhanced scalar fluctuations (B) are emphasized. The dotted lines show the limits of the OH state relationship.

Information from these Z values is not transferred to the OH time series. In contrast, the position marked B in Fig. 6 shows a location where very small deviations in Z are amplified in the OH time series because they occur near the edge of the OH distribution. Thus, the spectral content of the OH distribution is expected to differ significantly from that of the Z distribution. In particular, the integral time scale will generally be much less for a more narrowly distributed scalar such as OH. This effect will be even stronger for a considerably narrower state relationship such as that for CH, since even fewer Z values contribute to the scalar signal.

It is beneficial to define a scalar intermittency to aid in the interpretation of the above results. Regions such as the one marked A in Fig. 6 show the simulated scalar going to zero because the instantaneous Z value falls outside the range of the state relationship. An intermittency factor can be defined to quantify the frequency

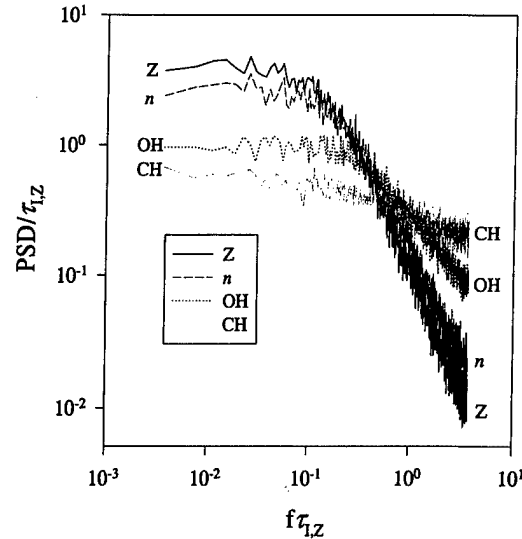


Fig. 7. Predicted PSDs for n , OH, and CH compared to the input Z PSD for the same conditions as those used for Fig. 6. The Z PSD contains noise because of the PDF mapping procedure.

of these events as the percentage of points in the time series for which the Z value falls outside the range 0.06 to 0.2 (for OH). This definition is not the same as that for turbulence intermittency, which is defined based on fluctuations between laminar and turbulent conditions, since reactive scalars such as OH can be zero in the presence of rich mixtures that are still turbulent (as in region A). Moreover, the scalar intermittency will strongly depend on the identity of the scalar, and will be smaller for major species and larger for narrowly distributed minor species.

The effect of increased scalar intermittency is clearly visible in the scalar PSDs. Figure 7 shows simulated Z, n , OH, and CH PSDs for the same conditions as the time series of Fig. 6. The n and Z PSDs are essentially the same since the n state relationship exists over all Z values (low scalar intermittency). The OH and CH PSDs show an increasing change from the input Z PSD because of this scalar intermittency. The faster fluctuations visible in the time series are represented in the PSDs by an extension to higher frequencies. The PSD shape itself is also modified, as the slope at high frequencies drops for a larger intermittency. This effect has been fully discussed by Renfro et al. [12], but our

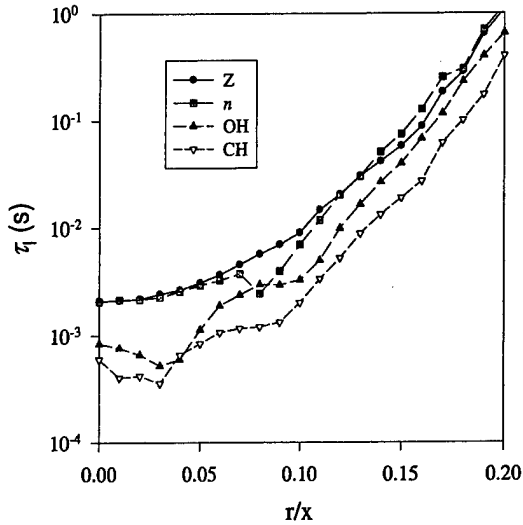


Fig. 8. Predicted profiles versus r/x of integral time scales for n , OH, and CH compared to that for the input Z time scales at $x/D = 20$. All other conditions are the same as those used for Figs. 6 and 7.

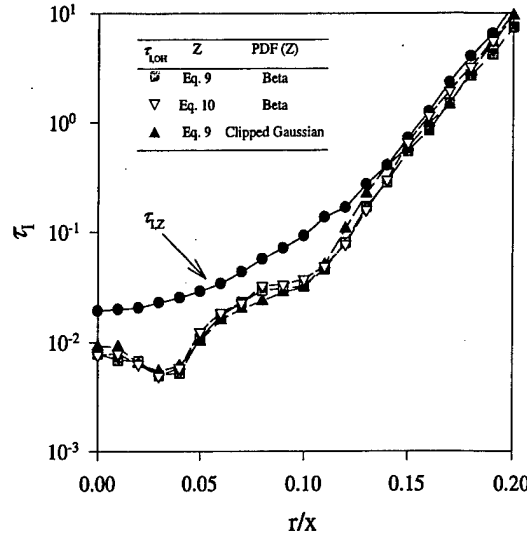


Fig. 9. Radial profiles of integral time scales predicted for OH with three input mixture fraction mean and PDF conditions.

prior work did not address the impact of this intermittency on the scalar integral time scale.

Figure 8 shows radial profiles of integral time scales for the four scalars at $x/D = 20$. The n time scale is nearly identical to the Z time scale for all radial locations except at $r/x = 0.08$, which corresponds to the radial location of minimum average number density. For OH and CH, the scalar time scales are always lower than the input mixture fraction time scales because of the influence of scalar intermittency. Since CH has a narrower state relationship than OH, its time scale is smaller than that of OH.

Sensitivity of Predicted Time Scales to Z Inputs

To assess potential errors in the prediction of scalar time scales caused by uncertainty in the measured Z inputs, each input was parametrically varied over a large range of conditions. The mixture fraction mean, rms, and PDF were found to significantly affect the corresponding statistics for the predicted scalars. For example, the maximum in the mean scalar profile occurs at a different radial location when the profile for mean mixture fraction is changed from Eq. 9 to Eq. 10. These dependencies are exactly the same as for an assumed PDF simulation (with-

out time scale consideration) and are therefore not addressed here. Instead we focus on the predicted scalar PSD and time scale. These two statistics are largely unaffected by the input mean and PDF shape for the mixture fraction. As an example, Fig. 9 shows the predicted radial profile of the OH time scale for both a clipped Gaussian and a Beta PDF shape with Z from Eq. (9), and for a Beta PDF with Z from Eq. 10. For all combinations the predicted time scales are essentially the same.

As demonstrated by Renfro et al. [12], the PSD shape for a scalar is significantly affected by Z_{rms} , with a decreased high-frequency slope and an extension to higher frequencies at greater Z_{rms} . These changes occur because a larger Z_{rms} causes a larger scalar intermittency. Consequently, the time scale for scalar fluctuations tends to decrease with increasing Z_{rms} . Recall, we are using measured mean and rms values for Z from a $Re = 15,200$ flame ($D = 8$ mm) for these simulations, but are comparing to times-series measurements in a $Re = 9,000$ flame ($D = 3.4$ mm). The potential differences in the axial mixing rate and the jet width at a given height (x/D) between these two flames affect the prediction of mean and rms values for the various scalars. Thus, if the $Re = 9,000$ flame has significantly different Z_{rms} profiles vs.

r/x than those shown in Fig. 2, the shape of the time scale profiles will be altered accordingly. Likewise, the PSD is affected by the width of the scalar state relationship as this impacts the scalar intermittency.

In addition to Z_{rms} , the mixture fraction PSD shape strongly affects the scalar PSD shape. For small scalar intermittency, the two PSD shapes are virtually identical. As the scalar intermittency increases, the PSD shapes differ as demonstrated by Renfro et al. [12]. Little difference between the scalar and mixture fraction PSDs is observed on the air-side of the scalar peak (where the mixture fraction mean, rms, and scalar intermittency are all small). Thus, the measured OH PSDs on the air side of the maximum OH location reported by Renfro et al. [3] are likely indicative of the corresponding mixture fraction PSDs. The composite PSD shown in Fig. 3 is from the air-side OH data in these flames and is indeed quite similar to the exponential PSD previously reported for mixture fraction [11].

The predicted scalar time scales are found to be independent of the mixture fraction mean, PDF shape, and PSD shape, but are directly affected by $\tau_{I,Z}$ and the scalar intermittency. In fact, the predicted OH time scale was found to be linearly related to the input mixture-fraction time scale over a two orders-of-magnitude change in the value of C , which is even larger than the changes observed in our measurements as a function of radial and axial position. Changing the shape of the velocity profile alters the shape of the scalar time scale profile as shown in the top panel of Fig. 10; however, the ratio $\tau_{I,[OH]}/\tau_{I,Z}$ is unique and appears to be affected by only the scalar intermittency, as shown in the bottom panel of Fig. 10. For this reason, differences between the velocities in the flames measured by Schneider et al. [18] and our smaller $Re = 9,000$ flames have minimal impact on the results of the simulations. The reduction in time scale caused by scalar intermittency is a very convoluted function that consequently depends on the detailed shape of the state relationship as well as on the Z_{rms} statistics.

The simulated scalar time scales depend on the input state relationships primarily because the width of each state relationship (in Z coordinates) is important for determining the scalar

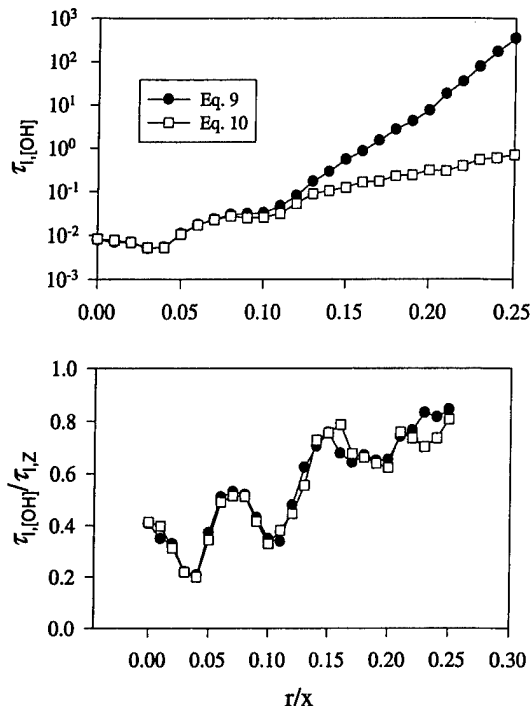


Fig. 10. Hydroxyl time scale profiles (top) and the ratio of OH time scales to mixture fraction time scales (bottom) for variable input velocity conditions. The time scale ratios are uniquely predicted by the time-series simulations.

intermittency. A narrower state relationship, such as for [CH], causes a higher scalar intermittency than that for [OH] and the resulting time scales are smaller (see Fig. 8). We have examined other state relationships corresponding to strain rates from $S = 10$ to $S = 450 \text{ s}^{-1}$, over which the flame thickness differs by a factor of nearly four. Since the simulation uses a one-dimensional laminar flamelet, however, it is the variation in profile width vs. mixture fraction that is important, and this changes by only 20% from $S = 10$ to $S = 450 \text{ s}^{-1}$. This difference is much smaller than the difference between the OH and CH widths at a fixed strain rate. Thus, the results presented here depend only minimally on the chosen strain rate.

Model Evaluation using Experimental Data

Having examined the sensitivity of the present time-series model to the various inputs, the following observation can be made:

1. The prediction of a scalar's mean, rms, or PDF shape only depends on the mean, rms, and PDF of the mixture fraction and on the chosen state relationship. This result is the same as for an assumed PDF simulation that neglects time scale information.
2. The predicted PSD and time scale for a reactive scalar differ from those of the input mixture fraction because of scalar intermittency, which is caused by the narrow extent of most state relationships for reactive scalars.
3. Increases in reactive scalar intermittency are caused by an increased Z_{rms} , narrower scalar state relationships, or an average Z value close to the edge of the reactive scalar distribution.
4. As the scalar intermittency increases, the integral time scales become smaller and the PSD flattens and extends to higher frequencies. The ratio of scalar to mixture fraction time scales is a convoluted function that depends strongly on the shape of the state relationship and on the radial profile for Z_{rms} .

Renfro et al. [4] found that the radial profiles of mean concentration and integral time scale for OH collapse to a self-similar curve for different axial heights when normalized by the radial location of peak [OH] and by the OH profile full-width-at-half-maximum (FWHM). To separate the prediction of scalar intermittency and time scale reduction from that of scalar peak location, the simulations and the measurements must be compared with respect to the similarity variable, $\Gamma = (r - r_{[\text{OH}]_{\text{max}}}) / \text{FWHM}_{[\text{OH}]}$, where the peak location and FWHM are determined from a least-squares fit to each simulation and measurement.

Figure 11 shows a comparison of the OH measurements and simulations at each of the four axial heights investigated. Quantitative agreement between the simulations and measurements cannot be achieved because there is no basis for an a priori selection of the constant C . However, in Fig. 11, each predicted radial profile has been normalized such that the predictions match the measurements on the fuel side of the [OH] peak. Because the simulated

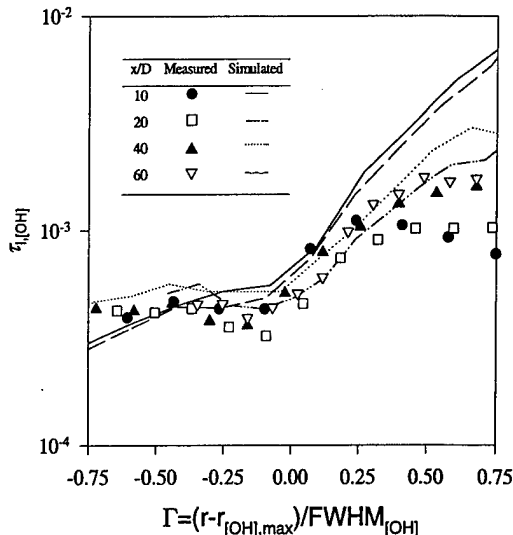


Fig. 11. Comparison of predicted to measured OH integral time scale profiles at axial heights of $x/D = 10, 20, 40,$ and 60 . Measured data are from Renfro et al. [3]. The predicted profiles have been normalized by the average time scale on the fuel side of the [OH] peak.

scalar time scales depend linearly on the input time scales for mixture fraction, this normalization does not affect the shapes of the profiles. In general, the simulation does a good job of replicating the shape of the radial profiles; that is, both the measurements and simulations show an increase in time scale to the air side of the [OH] peak ($\Gamma > 0$) and a slow decrease or invariance in the time scale toward the fuel side ($\Gamma < 0$). This nearly flat time-scale profile for $\Gamma < 0$ is surprising since the Z time scales used as inputs to the time series simulation decrease by a factor of two or more over this same range. Nevertheless, the laminar-flamelet approximation captures this experimental trend with reasonable accuracy. However, the simulation does not capture the axial change in time scales. The measurements show that the time scale at the [OH] peak ($\Gamma = 0$) and on the fuel-side of the [OH] peak is invariant with axial height (these have not been scaled in any way), whereas the input time scale increases in a manner consistent with Eq. 11. Therefore, the present data do not appear to be consistent with the convective scaling of Eq. 11. This discrepancy is addressed further in the next section.

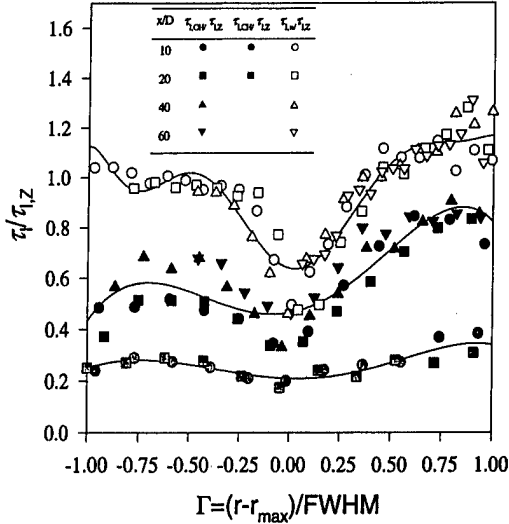


Fig. 12. Predicted ratios of scalar to mixture fraction time scales for n , OH, and CH at different axial heights. The curves are polynomial fits through all of the simulations.

Inverse Calculation of Mixture Fraction Time Scale from Reactive Scalar Data

Although the simulation does not predict quantitative time scales for OH because of the uncertainty of Eq. 11 for jets with heat release, the bottom panel of Fig. 10 indicates that it does a good job of predicting the radial profile of the OH time scale in normalized coordinates. This was found to be the case for all of the simulations considered in this investigation. A reasonable extension of this technique is to estimate mixture fraction time statistics from the measured OH data using an inverse (or iterative) calculation. Essentially, the simulation is used to predict the ratio of OH to Z time scales (as in the bottom of Fig. 10). This predicted ratio and the measured OH time scales then imply a quantitative value for the Z time scale. This procedure is successful because the predicted time scale ratios are insensitive to most model inputs.

The ratios of predicted to input mixture fraction time scales for OH, CH, and n are shown in Fig. 12. As discussed previously, these ratios decrease as the scalar profile width narrows, owing to an increase in scalar intermittency. A polynomial fit to these ratios yields a prediction of the effect of this inter-

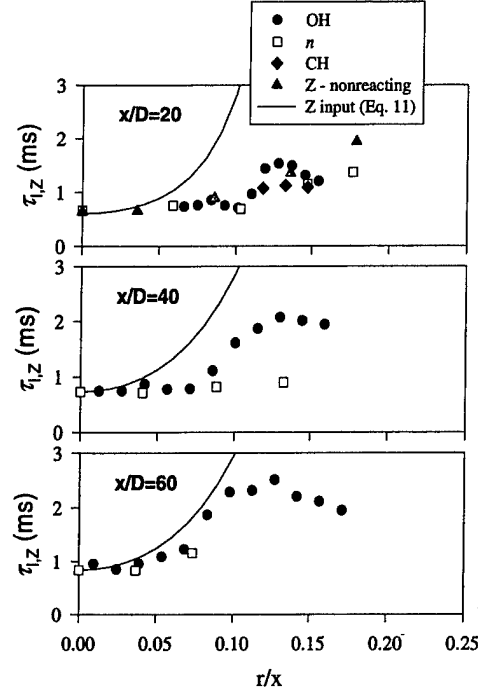


Fig. 13. Extrapolated mixture fraction time scales. For each data set, the Z time scale has been computed by dividing the measured scalar time scale by the predicted time scale ratio (Fig. 12). The measured data are from Renfro et al. [3] for OH, Renfro et al. [4] for CH, Lakshmanarao [17] for n and Lakshmanarao et al. [19] for the non-reacting jet mixture fraction.

mittency as a function of the similarity variable, Γ . This function is invariant with height in the flame to within $\pm 20\%$ and is mostly insensitive to the simulation's inputs (except Z_{rms} , as previously discussed). An estimate for the mixture fraction time scale can therefore be made by dividing the measured OH, CH, and n time scales by this ratio. This was performed for each measured data point and the resulting estimated mixture fraction time scales are shown in Fig. 13 for heights $x/D = 20, 40,$ and 60 . Data for $x/D = 10$ are excluded since reliable data are only available for OH at this height.

The estimates for the underlying mixture fraction time scales based on n and OH are independent of one another. Nevertheless, at each height the two calculations are nearly identical (with the exception of one point at $x/D = 40$). Similar independent estimates obtained from the CH data are also shown at

$x/D = 20$. These values are consistent with the n and OH values at the same height (CH data could not be collected at large x/D). A comparison of the three estimates for $\tau_{1,Z}$ cannot be made at all radial locations because of errors with the Rayleigh scattering technique caused by entrainment of particles from room air [17], and because the PSDs for CH at some locations are not conducive to calculation of an integral time scale [4].

The accuracy of these estimates for $\tau_{1,Z}$ are affected by the accuracy of the measured scalar time scales, by the accuracy of the simulated time scale ratios, and by any systematic limitations in the model's assumptions, primarily the one-dimensional flamelet approximation. The uncertainty for $\tau_{1,[OH]}$ is about $\pm 20\%$ [3] and the variation in $\tau_{1,Z}/\tau_{1,[OH]}$ from Fig. 12 is also $\pm 20\%$ for a wide range of conditions. Thus, the estimated mixture fraction time scales have an uncertainty of at least $\pm 28\%$ (95% confidence interval). For this particular flame, the number density is well described by a laminar flamelet approximation based on the single-shot realizations of Meier et al. [6], so the simulation should yield the true mixture fraction time scale when applied to the measured number density data. The good agreement between values for the mixture fraction time scale estimated using OH, CH, and n implies that this simple simulation is also applicable to intermediate scalars, even though their instantaneous values are not always solely dependent on the mixture fraction [6].

Figure 13 also shows ($x/D = 20$) direct measurements of mixture fraction time scales in a non-reacting jet using acetone-seeded LIF [19] and the input time scales from Eq. 11 using the measured profile of Schneider et al. [18]. The three mixture fraction time scale profiles estimated from the reactive scalar data are much shallower than that estimated from Eq. 11. The simulations are very similar to the non-reacting jet measurements, but this agreement is likely coincidental since several differences exist between the reacting and non-reacting flows. However, it appears likely that the mixture fraction time scale increases more slowly with rising radial location than predicted by the velocity profile alone. The mixture fraction time scale also displays a significantly different de-

pendence on axial height than that assumed for Eq. 11. In fact, there is only a 27% increase in the integral time scale from $x/D = 20$ to $x/D = 60$, instead of the factor of 9 increase suggested by an x^2 dependence. We are not able to assess the virtual origin of our jet from our measurements, which will impact the axial growth rate of mixing time scales. However, no plausible virtual origin location will make these results consistent with x^2 scaling, and the shallow growth of time scale vs. r/x at $x/D = 20$ is inconsistent with the width of the velocity profile. These results suggest that for jets with heat release, the time scale cannot be simply computed as the jet width divided by the local velocity. This result may depend on the relatively low axial heights and Reynolds numbers considered here; however, these heights are representative of typical flame lengths for turbulent jets.

CONCLUSIONS

A time-series simulation has been utilized to predict the mean, rms, PDF, PSD, and integral time scale for [OH], [CH], and total number density in a series of hydrogen/methane/nitrogen flames for which the same data are available. This simulation depends on assumed values for the mean, rms, PDF shape, PSD shape, and integral time scale for the mixture fraction and on a one-dimensional state relationship for the scalar of interest. Comparisons between measurements and predictions have been presented for a $Re = 9,000$ flame because of the availability of more extensive data for this condition. The following conclusions can be drawn from this study:

1. The scalar (OH, CH, or n) mean, rms, and PDF statistics are not affected by the inclusion of mixture fraction PSD and time scale information.
2. The shape of the mixture fraction PSD affects the predicted shape of other scalar PSDs, but the two PSDs and their respective time scales are different because of intermittency in the concentration time series [12]. No other statistic is significantly affected by the PSD shape for Z.
3. Variations in the width of the scalar state

relationship do not significantly affect the shape of the radial profile for the integral time scales but do directly affect the magnitude of the time scales.

4. The predicted ratio of the scalar to mixture fraction time scale is very sensitive to Z_{rms} and to the width of the state relationship, but essentially insensitive to all other input mixture fraction statistics.
5. Mixture fraction time scales can be estimated from the measured OH, CH, and n time series using an inverse calculation. All three data sets give consistent estimates for the mixture fraction time scale, which increases slightly with axial height (27% increase from $x/D = 20-60$) but is always within 12% of $750 \mu s$ on the jet centerline. Convective scaling using the jet width and the local mean velocity to define the mixture fraction time scale is inconsistent with the measured data.

The implementation of a one-dimensional laminar flamelet approximation precludes description of turbulence-chemistry interactions in the scalar time series. Hence, an important application of this analysis is to distinguish between those scalar measurements that are simply dominated by convective fluctuations and those that are more complicated. As an example, time series measurements of CH in a $Re = 15,200$ flame [4] display PSDs that cannot be described with a single time scale. This particular flame is very near the blow-off limit, and it is likely that local extinction is present. Consequently, the simulations presented here may eventually permit a distinction between those aspects of the CH time series arising from convective fluctuations and those arising from extinction events.

This work has been supported by the Air Force Office of Scientific Research, with Dr. Julian Tishkoff as technical monitor. We would like to thank Rob Barlow (Sandia National Laboratories), Wolfgang Meier (German Aerospace Center), and Christoph Schneider (TU-Darmstadt) for providing their data and for fruitful discussions about this work.

REFERENCES

1. Dibble, R. W., and Hollenbach, R. E., *Proc. Combust. Inst.* 18:1489 (1981).
2. Gökalp, I., Shepherd, I. G., and Cheng, R. K., *Combust. Flame* 71:313 (1988).
3. Renfro, M. W., Gutfenfelder, W. A., King, G. B., and Laurendeau, N. M., *Combust. Flame* 123:389 (2000).
4. Renfro, M. W., King, G. B., and Laurendeau, N. M., *Combust. Flame* 122:139 (2000).
5. Bergmann, V., Meier, W., Wolff, D., and Stricker, W., *Appl. Phys. B* 66:489 (1998). (see also *DLR - Experimental Data Arch.*, <http://www.dlr.de/VT/Datenarchiv>).
6. Meier, W., Barlow, R. S., Chen, Y.-L., and Chen, J.-Y., *Combust. Flame* 123:326 (2000). (see also *International Workshop on Measurement and Computation of Turbulent Nonpremixed Flames*, <http://www.ca.sandia.gov/tdf/Workshop.html>).
7. Birch, A. D., Brown, D. R., Dodson, M. G., and Thomas, J. R., *J. Fluid Mech.* 88:431 (1978).
8. Becker, H. A., Hottel, H. C., and Williams, G. C., *J. Fluid Mech.* 30:285 (1967).
9. Dowling, D. R., and Dimotakis, P. E., *J. Fluid Mech.* 218:109 (1990).
10. Renfro, M. W., Pack, S. D., King, G. B., and Laurendeau, N. M., *Combust. Flame* 115:443 (1998).
11. Kounalakis, M. E., Sivathanu, Y. R., and Faeth, G. M., *J. Heat Trans.* 113:437 (1991).
12. Renfro, M. W., Sivathanu, Y. R., Gore, J. P., King, G. B., and Laurendeau, N. M., *Proc. Combust. Inst.* 27:1015 (1998).
13. Kounalakis, M. E., Gore, J. P., and Faeth, G. M., *Proc. Combust. Inst.* 22:1281 (1988).
14. Box, G. E. P., Jenkins, G. M., and Reinsel, G. C. *Time Series Analysis*, 3rd ed., Prentice Hall, Englewood Cliffs, NJ, 1994.
15. Faeth, G. M., Kounalakis, M. E., and Sivathanu, Y. R., *Chemom. Intell. Lab. Syst.* 10:199 (1991).
16. Ji, J., Sivathanu, Y. R., and Gore, J. P., *Proc. Combust. Inst.* 28:391 (2000).
17. Lakshmanarao, A., *Time-series measurements of mixture fraction and temperature in turbulent non-reacting jets and turbulent nonpremixed flames*, M.S. Thesis, Purdue University, West Lafayette, IN, 1999.
18. Schneider, C., Dreizler, A., and Janicka, J., *LDV-Measurements in Hydrocarbon Air Jet Flames*, Private Communication, 2000.
19. Lakshmanarao, A., Renfro, M. W., King, G. B., and Laurendeau, N. M., *Exp. Fluids* 30:595 (2001).
20. Pitts, W. M., and Kashiwagi, T., *J. Fluid Mech.* 141:391 (1984).
21. Schlichting, H., *Boundary-Layer Theory*. McGraw-Hill, New York, 1979, pp. 747-750.
22. Dai, Z., Tseng, L. K., and Faeth, G. M., *J. Heat Trans.* 117:138 (1995).
23. Drake, M. C., Bilger, R. W., and Stårner, S. H., *Proc. Combust. Inst.* 19:459 (1982).
24. Effelsberg, E., and Peters, N., *Combust. Flame* 50:351 (1983).
25. Lutz, A. E., Kee, R. J., and Grcar, J. F., *OPPDIF: A*

Fortran program for computing opposed-flow diffusion flames, Sandia National Laboratories Report No. SAND96-8243, 1996.

26. Bowman, C. T., Hanson, R. K., Davidson, D. F., Gardiner Jr., W. C., Lissianski, V., Smith, G. P., Golden, D. M., Frenklach, M., and Goldenberg, M.,

GRI Mechanism, version 2.11. http://www.me.berkeley.edu/gri_mech/ (1995).

Received 19 April 2001; revised 19 September 2001; accepted 16 November 2001

Mass Spectrometric Study of Combustion and Thermal Decomposition of GAP

O.P. KORBEINICHEV*, L.V. KUIBIDA, E.N. VOLKOV, and A.G. SHMAKOV

Institute of Chemical Kinetics and Combustion, Russian Academy of Science, Novosibirsk 630090, Russia

Glycidyl azide polymer (GAP) is an active energetic binder in rocket propellants. The main objective of this research was to study the decomposition and combustion chemistry of thoroughly characterized GAP samples to develop a model for the combustion of GAP and propellants based on GAP. The combustion characteristics (burning rates, temperature profiles) and kinetic parameters (order of reaction, activation energy, pre-exponential factor of rate constants) for the thermal decomposition of GAP together with the composition of the products of both the combustion and decomposition of uncrosslinked GAP (with a molecular weight of 350 or 2000) and cured GAP were studied. The flame and thermal decomposition of GAP, as well as the composition of the products were studied using molecular-beam mass-spectrometry (MBMS). The final temperature of a flame of GAP was measured as 1000 to 1100 K. About half of the mass of the combustion products involves large fragments of a polymer without its azide groups. For this reason the mass spectrum obtained on direct MBMS sampling of a flame burning GAP could not be completely interpreted. However, ~47% of the mass of the combustion products was found to be the volatile gases N_2 , H_2 , CO , CO_2 , CH_4 , C_2H_4 , C_2H_6 , NH_3 , H_2O , acetonitrile, acrylonitrile, and furane, as obtained by mass-spectrometry using freezing/thawing in a liquid nitrogen trap.

The thermal decomposition of thin films of GAP at 1 bar was done in a flow reactor with Ar flowing through it. A tungsten plate was used as a sample heater; its temperature was controlled using a chromel-copel (copel is an alloy of 56.5% Cu, 43.0% Ni and 0.5% Mn) or Pt-PtRh (10%) thermocouples. The thermal decomposition of GAP was studied at a high heating rate over a wide temperature range in three ways: (1) the heating rate was changed from the maximal to the minimal one in the course of decomposition (400–100 K/s); (2) at the linear heating rate (50–400 K/s); (3) fast heating (~400 K/s) to the given temperature and subsequently maintained isothermal. Three stages of thermal decomposition were found. The first stage (yield of nitrogen is ~15%) is a first order reaction. The second stage (yield of N_2 is ~25%) is an autocatalytic one; the third stage is first order and is a weakly exothermic one, with a yield of nitrogen of ~60%. Kinetic parameters (activation energy and pre-exponential factor of rate constants) were found for each stage. The results for both the combustion and thermal decomposition of GAP were compared with literature data and it was concluded that the results strongly depend on the conditions of the experiment and on the source of the GAP. © 2002 by The Combustion Institute

INTRODUCTION

Azide polymers incorporate one or several N_3 groups per monomer. Their study is of great interest as they can be used as active binders in rocket propellants. The availability of the N_3 -group in a monomer releases additional heat on combustion, giving a higher final combustion temperature and specific impulse. The energy released by an N_3 -group decomposing to N_2 is ~378 kJ/mol [1]. Glycidyl azide polymer (GAP) has the formula: $OH(-CH_2-CH(CH_2-N_3)-O-)_nH$. Uncured GAP with $n = 20$ is a viscous yellow liquid under normal conditions. Its density is $\rho = 1.3 \text{ g/cm}^3$, adiabatic flame temperature is $T_f = 1465 \text{ K}$ at $p = 50 \text{ bar}$ [1]. Cured GAP includes 84.8 wt% of uncured GAP, 12.0

wt% of hexamethylene diisocyanate (HMDI) and 3.2 wt% of trimethylpropane (TMP). Cured GAP has the formula $C_{3.3}H_{5.6}O_{1.12}N_{2.63}$, with a density of 1.27 g/cm^3 and an adiabatic flame temperature of 1365 K at 50 bar [1].

Previous work on GAP as a propellant ingredient can be divided into two groups. The first group is devoted to the study of the combustion of GAP [1, 2], and the second to its thermal decomposition [1, 3–10]. Kubota et al. [1] have measured the burning rate of cured GAP in an atmosphere of nitrogen. The burning rate was found to increase monotonically with pressure from 2.2 mm/s at 4.5 bar to 11 mm/s at 80 bar at the initial temperature $T_0 = 293 \text{ K}$. The initial temperature rise of 50 K results in a 1.7-fold rise in burning rate. The calculated mole fractions of the products from the combustion of GAP for equilibrium at 50 bar are: $0.2234 N_2 + 0.2847 C$

*Corresponding author. E-mail: korobein@ns.kinetics.nsc.ru

Scalar Time-Series Measurements in Turbulent CH₄/H₂/N₂ Nonpremixed Flames: CH

MICHAEL W. RENFRO, GALEN B. KING, AND NORMAND M. LAURENDEAU

School of Mechanical Engineering, Purdue University, West Lafayette, IN 47907-1288, USA

Time-series measurements of CH concentrations [CH] are reported in a series of methane/hydrogen/nitrogen diffusion flames. Power spectral densities (PSDs) and autocorrelation functions are computed from the time series, permitting a detailed investigation of [CH] fluctuation time scales. The effects of fluorescence lifetime fluctuations are found to be negligible for quantitative determination of the PSDs. A similar study of hydroxyl concentrations in nonpremixed hydrogen/argon flames recently demonstrated that OH PSDs collapse to a single curve when normalized by the integral time scale, in agreement with mixture fraction statistics. However, for the present measurements, [CH] data on the fuel-side of the peak [CH] location exhibit low-frequency differences in their PSDs with respect to both the [OH] and air-side [CH] PSDs. These differences could be associated with the closer proximity of the CH radical to the shear layer and thus to enhanced fluctuations in the local mixture fraction. This possibility can be examined via measurements of other scalars. © 2000 by The Combustion Institute

INTRODUCTION

Measurements of minor-species concentrations in turbulent flames are of interest owing to their importance in pollutant chemistry and to their use as markers of instantaneous flame structure. Hydroxyl (OH), nitric oxide (NO), and methylidyne (CH) measurements have been reported by many researchers in a wide variety of laminar and turbulent flames; however, most of these studies have employed high-power, low-repetition-rate, pulsed lasers. With such instrumentation, two sequential measurements are further apart in time than most correlations arising from turbulent fluctuations. Thus, the measurements are temporally independent from one shot to the next and yield only single-time statistics, including the mean, variance, and probability density function (PDF). For most engineering applications, accurate prediction of scalar PDFs (and in many cases just the mean) is sufficient. However, current model closure assumptions, and thus predictions, are not yet adequate as a design tool. Hence, turbulence models will benefit from a better physical understanding of turbulent flames, including the effects of turbulence-chemistry interactions.

Many groups have developed diagnostic techniques to provide novel data which may better address these issues. For example, multiscale

measurements have provided conditional statistics [1] and multipoint measurements have provided spatial-scale information [2, 3]. Our research has focused on the development of a technique for determining temporal scales for minor-species concentrations. The statistics recovered from these measurements complement other available diagnostics, thus providing a more complete representation of scalar fluctuations.

Time-series measurements of minor-species concentrations are complicated by potential fluctuations in the fluorescence lifetime. Such time-series measurements are obtainable via picosecond time-resolved laser-induced fluorescence (PITLIF), as reported previously for both CH [4] and OH [5] in a low-Reynolds number methane flame. However, the potential effects of lifetime fluctuations were not fully addressed in these initial studies. Subsequently, quantitative time-series measurements of minor-species concentrations were made possible via a unique photon counting technique which simultaneously measures both the fluorescence signal and the fluorescence lifetime [6, 7]. This photon-counting version of the PITLIF technique was recently applied to hydroxyl measurements in a series of hydrogen/argon flames at Reynolds numbers up to 17,000, yielding the first quantitative measurement of time scales for minor-species concentrations [8]. Remarkably, the measured OH power spectral densities (PSDs) (and equivalently, the autocorrelation

Corresponding author. E-mail: renfro@ecn.purdue.edu

functions) were found to collapse onto a single curve when normalized by the measured integral time scales [9]. Furthermore, the integral time scales were found to essentially follow existing scaling laws for velocity in nonreacting turbulent jets [10], which are also similar to those for mixture fraction in nonreacting jets [11, 12] and in flames [13]. This collapse is not expected for reactive scalars and may have direct implications with respect to improved modeling of species concentrations in turbulent flames.

In the present study, time-series measurements of CH concentrations are presented for a series of methane/hydrogen/nitrogen jet diffusion flames. The effect of lifetime fluctuations on the measured CH concentrations is examined. PSDs and PDFs are compared for various axial and radial locations and for various Reynolds numbers. The PSDs and autocorrelation functions are also normalized appropriately to determine if the two-time statistics collapse, as for the previous OH measurements [9]. The CH measurements reported here represent the first part of an ongoing effort to characterize scalar time series for these specific $\text{CH}_4/\text{H}_2/\text{N}_2$ flames. Hydroxyl, nitric oxide, and temperature measurements are planned for the same flames in the near future. Bergmann et al. [14] reported multiscale measurements in a similar flame and have made this data available via the Internet [15]. When combined with these multiscale measurements, detailed analyses of our time-series data may eventually offer new insights on turbulence-chemistry interactions in nonpremixed flames.

MEASUREMENT TECHNIQUE

The laser system used for the present measurements is identical to that employed by Renfro et al. [4]. Briefly, an argon-ion pumped Ti:Sapphire laser was frequency doubled to produce an 80-MHz repetition rate, 1.5-ps full-width at half-maximum (FWHM) pulse stream at 430.6 nm (0.2-nm FWHM). The laser was focused over the burner and excited ~ 10 Q-branch transitions within the (0,0) vibrational band of the $X^2\Pi - A^2\Delta$ electronic system of CH. This wavelength was chosen to minimize the temper-

ature dependence of the Boltzmann fraction. Based on full simulations of CH absorption using a code developed by Seitzman [16], this spectral location produces an absorption coefficient variation of only $\pm 3\%$ from 1500 to 2500 K. Excitation of a single rovibronic transition (via a modified laser pulse width) has been used for our CH time-series measurements in the past with nearly identical results, but at a lower signal-to-noise ratio [4].

The detection and electronics system used for the present study is identical to that employed for our previous hydroxyl measurements [8]. Fluorescence photons were collected by a 0.25-m monochromator and a Hamamatsu HS5321, 700-ps risetime photomultiplier tube (PMT). The fluorescence signal from CH is much weaker than that from OH because of the much lower concentration; thus, significant care must be taken to ensure that no laser light is scattered into the monochromator from surfaces near the flame. Moreover, the reduced fluorescence signal requires a slightly larger probe volume along the laser beam to achieve an adequate total photon count. The spatial resolution for these measurements was $140 \times 140 \times 250 \mu\text{m}^3$ based on the beam diameter (e^{-2}) and the monochromator entrance slit width. The spectral resolution was 10 nm centered at 431 nm. Each pulse from the PMT (corresponding to a single photoelectron) was counted using the methodology of Pack et al. [6], which divides the signal into three 3.5-ns gated bins locked to the arrival time of the laser pulse. The photon counts in each bin were integrated for a period of time equal to the inverse of the sampling rate, which produced three separate but simultaneous time series. These time series were converted to two time series representing concentration and lifetime by using a code developed by Renfro et al. [17], which corrects for pulse pileup and permits much higher total photon counts than are possible with traditional photon-counting techniques.

Unlike the previous hydroxyl measurements [8], the resulting CH concentration time series are not calibrated to recover absolute values, owing to the difficulty of obtaining an absolute CH concentration from either kinetic models or potential calibration flames. However, each

measurement reported here has been internally calibrated relative to a single location in one of the test flames, and all concentrations are reported relative to this value. Fortunately, both the PDF shape and the PSD are measures of only concentration fluctuations, and are not affected by the lack of an absolute calibration.

CH measurements were made in seven 22.1% CH₄, 33.2% H₂, 44.7% N₂ (by volume) jet diffusion flames issuing from a circular nozzle into still air with Reynolds numbers from 2800 to 15,200. Two burners were used with diameters of 3.4 and 7.8 mm. The seven flames are designated A1–A5 and D1–D2, as shown in Table 1. Radial profiles of time-averaged [CH] were obtained at $x/D = 1, 2, 5,$ and 10 in each flame using a sampling rate of 10 Hz and an averaging time of 3 seconds. At each height time-series measurements were obtained with sampling rates as given in Table 1 for about three radial locations displaying significant CH signals. Fifty time series of 4096 points each were collected to obtain clean statistics. PDFs, PSDs, autocorrelation functions, and integral time scales were computed from these time series in the same manner as reported by Renfro et al. [8, 9].

TABLE 1

Burner and Flow Parameters for the Seven Flames Utilized in This Study^a

Flame	Burner Diameter (mm)	\bar{V} (m/s)	Re	Sampling Rate (Hz)
A1	3.4	16.3	2,800	10,000
A2	3.4	29.0	5,000	20,000
A3	3.4	52.3	9,000	20,000
A4	3.4	75.5	13,000	30,303
A5	3.4	88.3	15,200	40,000
D1	7.8	22.8	9,000	20,000
D2	7.8	38.5	15,200	30,000

^a The Reynolds number is computed from the average velocity, \bar{V} , and the cold-flow properties. The sampling rate for the time-series measurements is also given for each flame. Time-averaged radial profiles were measured at a sampling rate of 10 Hz in each case.

RESULTS

CH Concentration and Lifetime Profiles

Radial profiles of CH concentration are shown in Fig. 1 for each flame and height studied. The concentrations have been normalized by the maximum concentration at each height, and the radial coordinate has been normalized by subtracting the location of peak [CH] and dividing by the profile width (FWHM). The peak CH concentration (calibrated to the peak [CH] at $x/D = 5$ in flame A3), peak [CH] location, and profile width are given for each flame and each height in Table 2. The profiles are normalized in this manner for convenience in presenting the data. As a visual aid in Fig. 1, the plots have been scaled to show the decrease in [CH] through the calibration flame (3.4-mm burner, $Re = 9000$). The accuracy of the concentrations reported in Fig. 1 and Table 2 is approximately $\pm 25\%$ (95% confidence interval), as computed from errors associated with the day-to-day repeatability of the calibration flame measurement (20%), errors caused by spatially missing the exact peak of the narrow CH distributions (10%), and errors arising from measurement repeatability at each point (<5% typically). Error bars in Fig. 1 are shown only for the calibration flame to avoid clutter, but these are typical of all of the flames.

As discussed by Renfro et al. [8], the low

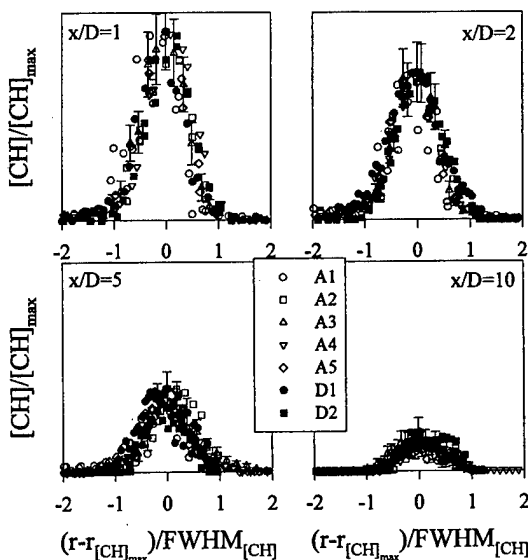


Fig. 1. Normalized radial profiles of CH concentration for each of the flames investigated. The parameters for normalization are given in Table 2. Each figure is scaled to show the relative concentration decay with axial height for flame A3.

TABLE 2
Measured Concentration and Lifetime Statistics for the Location (r/x) of Peak [CH] at
Each Measured Axial Height^a

Flame	x/D	r/x	$[\text{CH}]_{\text{max}}/[\text{CH}]_{\text{cal}}$	$[\text{CH}]_{\text{ms}}$ (%)	FWHM (mm)	I (%)	τ (ns)
A1	1	0.96	1.49	18.3	0.39	67.6	2.37
A1	2	0.53	1.18	35.8	0.53	89.8	2.25
A1	5	0.24	0.99	35.4	0.87	92.6	2.19
A2	1	0.86	1.73	16.2	0.39	52.3	2.28
A2	2	0.48	1.58	35.6	0.43	77.8	2.18
A2	5	0.21	1.09	75.9	0.64	78.5	2.15
A2	10	0.13	0.49	141.4	1.75	86.7	2.09
A3	1	0.77	2.29	16.5	0.29	37.0	2.30
A3	2	0.42	1.79	28.0	0.38	42.8	2.27
A3	5	0.20	1.00	79.4	0.53	72.4	2.10
A3	10	0.14	0.46	196.5	1.54	86.6	2.02
A4	1	0.70	2.33	22.2	0.31	40.4	2.24
A4	2	0.40	1.83	54.8	0.37	57.2	2.17
A4	5	0.20	1.12	89.9	0.62	71.3	2.10
A4	10	0.13	0.46	157.2	1.69	85.1	1.95
A5	1	0.70	2.98	22.3	0.31	37.4	2.32
A5	2	0.39	2.37	55.3	0.41	50.6	2.26
A5	5	0.19	1.37	115.1	0.71	75.5	2.07
A5	10	0.12	0.49	189.8	2.11	87.5	1.93
D1	1	0.70	1.01	37.8	0.50	60.3	2.16
D1	2	0.38	0.64	63.8	0.58	73.8	2.10
D1	5	0.19	0.31	195.3	1.59	89.5	2.03
D2	1	0.65	1.36	45.5	0.48	57.5	2.08
D2	2	0.36	0.88	85.8	0.71	71.8	2.02
D2	5	0.18	0.38	219.6	1.92	88.4	1.95
D2	10	0.11	0.26	436.0	2.95	93.9	1.88

^a The mean concentrations are calibrated to the peak concentration at $x/D = 5$ in flame A3 ($[\text{CH}]_{\text{cal}}$). The radial profile full-width at half-maximum (FWHM) and the PDF clipping factor, I , are also reported. The accuracy of the CH concentrations is typically $\pm 25\%$ (95% confidence interval).

repetition rate (10 Hz) used for the time-averaged radial profile measurements can potentially bias the results because of small nonlinearities in the relationship between photon counts and concentration or lifetime. At high sampling rates (as used for the time-series measurements) this biasing does not occur since all fluctuations are resolved; thus, reported PSDs and PDFs are not affected. Unfortunately, the data reduction algorithm is too slow to permit time-series measurements to be taken at all radial locations. Potential biasing of the radial profiles has been assessed here by comparing mean CH concentrations from the low-repetition rate measurements to those of the time-series measurements where available. As with the previous OH measurements [8], there are no noticeable differences in the shapes of the mean CH radial profiles as obtained from the

low repetition rate or time-series measurements; nevertheless, all of the statistical parameters in Table 2 have been taken from the high repetition rate data to avoid potential errors.

Radial profiles of the CH fluorescence lifetime were also examined and found to be nearly invariant throughout these flames. At very low heights ($x/D = 1$), the lifetimes decrease somewhat from the peak to the air side of the CH distribution but are always within 20% (and typically within 10%) of the lifetime given in Table 2. At $x/D = 5$ and $x/D = 10$, where most of the time-series analyses occur, the CH fluorescence lifetimes are always within 4% of the values in Table 2. The lifetimes at the location of peak [CH] decrease by an average of $\sim 12\%$ from $x/D = 1$ to $x/D = 10$ in each flame. In comparison to the previous hydroxyl lifetime measurements [8], the CH lifetimes display a

comparable decrease with axial height but are weaker functions of radial location than the OH lifetimes.

We have compared our measured lifetimes to predictions by using the major-species concentrations and temperatures of Meier [15] at $x/D = 5$ in flame D2 with the CH quenching cross-section correlations of Tamura et al. [18]. Temperature- and species-dependent cross-section information is presently much coarser for CH than for OH, particularly for the important quenching partner H_2O . Nevertheless, this simple calculation predicts lifetimes of about 2.8 ns near the [CH] peak location. This value is about 30% greater than our measured lifetime, which is consistent with the results of Tamura et al. [18] in low-pressure methane flames. More importantly, the variation of predicted lifetimes is less than 10% over the range of mixture fractions 0.15–0.45, for which any CH would be expected.

Calculation of root-mean-square values from time-series data requires correction for the effects of shot noise. Renfro et al. [8] corrected their OH data after computing the shot noise rms at each measurement location directly from the power spectra. This procedure requires a reasonably clean PSD so that the noise contribution can be accurately computed. For CH, the lifetime does not fluctuate sufficiently to recover a usable PSD or rms value; i.e., the fluctuations are almost entirely due to shot noise. This dominance of shot noise is also apparent in the lifetime PDFs, which are almost exactly equivalent to simulated PDFs obtained for the limiting case of independent, random (Poisson distributed) fluctuations in the three photon-counting bins. In particular, we performed this noise simulation with average bin counts taken from several measurements and found, in each case, that the entire lifetime PDF was predicted by only shot noise.

The concentration rms values in Table 2 have been computed from the uncorrected fluorescence data. As with our previous OH measurements, the CH fluorescence statistics were found to be identical to the concentration statistics, but with significantly improved signal-to-noise ratios. Hence, while [CH] fluctuations are measurable, CH lifetimes in these flames do not fluctuate at a level sufficient to affect the fluo-

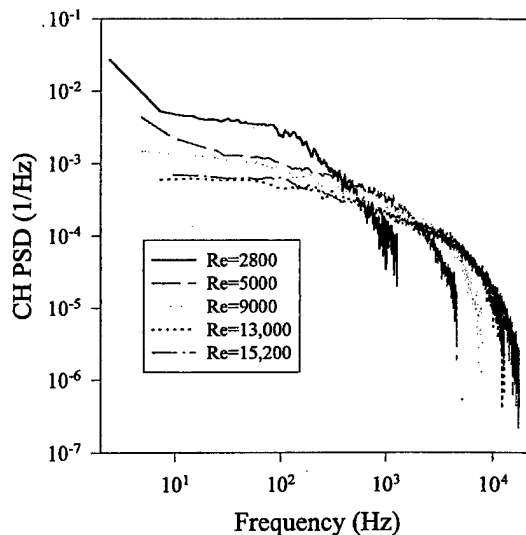


Fig. 2. Fuel-side PSDs at $x/D = 5$ in flames A1–A5. The radial location for the measurements is 0.0–0.2 mm toward the fuel side of the peak [CH] location given in Table 2. The PSDs have been corrected for shot noise and have been filtered by a 5-point moving average.

rescence measurements and thus may be neglected. This fortunate condition is not surprising since lifetime variations are less than 4% across the CH distribution through most of the flame, which permits fluorescence PSDs to be interpreted as concentration PSDs. The resulting simplification is utilized in the remainder of this paper and is further justified in the next section.

PSDs and Autocorrelation Functions

PSDs for each of the flames from the 3.4-mm burner are shown in Fig. 2. The measurement location for these spectra is about 0.1 mm to the fuel-side of the [CH] peak at $x/D = 5$. Measurements at the [CH] peak were essentially the same as these fuel-side measurements. As with our previous OH measurements, a significant change was found in the PSDs with Reynolds number. The decay of each PSD occurs at higher frequencies and the relative intensity of low-frequency fluctuations decreases as the Reynolds number rises. In Fig. 3, similar PSDs are shown for flames A2–A5 at a radial location approximately 0.5 mm to the air side of the [CH] peak. As with the spectra in Fig. 2, the

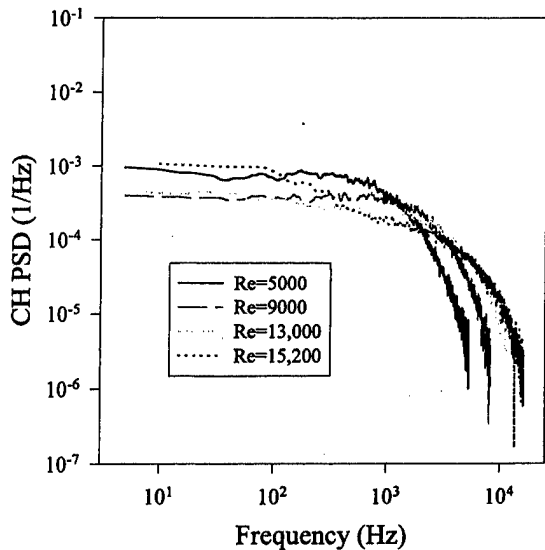


Fig. 3. Air-side PSDs at $x/D = 5$ in flames A2-A5. The radial location for the measurements is ~ 0.5 mm toward the air side of the peak [CH] location given in Table 2. The PSDs have been corrected for shot noise and have been filtered by a 5-point moving average.

decay of each PSD occurs at higher frequencies with increasing Reynolds number. However, the shapes of the air-side spectra (Fig. 3) are notably different from those on the fuel side and at peak [CH] locations (Fig. 2). In particular, at low frequencies, the air-side spectra are flat, whereas the fuel-side spectra have a slope of about -0.6 . In comparison, the CH PSDs display a slope of about -3.8 at high frequencies for both measurement locations.

These differences are especially apparent in the autocorrelation functions which are shown for the air-side measurements in Fig. 4 and for the fuel-side measurements in Fig. 5. Figs. 4b and 5b have been normalized by using the Reynolds number to permit better comparison among the different curves. The normalized autocorrelation functions are also compared with an exponentially decaying autocorrelation function. Hydroxyl fluctuations measured in hydrogen/argon flames were found to be well approximated by an exponential autocorrelation function [9], which has also been found to successfully characterize mixture fraction fluctuations in turbulent flames [13]. On the air-side of the [CH] peak (Fig. 4), all of the autocorrelation functions, except that for $Re = 15,200$,

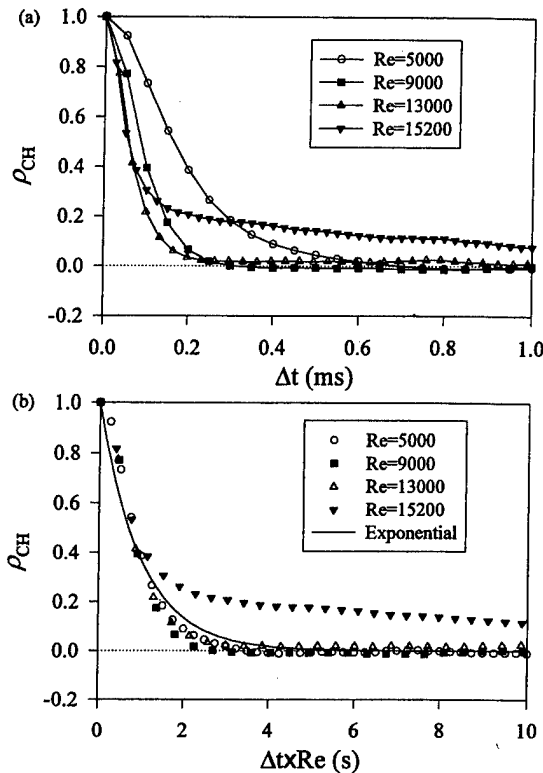


Fig. 4. Air-side CH autocorrelation functions for flames A2-A5 at the same locations as in Fig. 3: (a) as measured and (b) scaled by the Reynolds number. The normalized autocorrelation functions are compared to an exponential decay.

are essentially exponential and are indistinguishable from OH autocorrelation functions [9]. The $Re = 15,200$ air-side measurement closely resembles the fuel-side measurements of Fig. 5b, which are significantly different from an exponential decay. This discrepancy for the largest Reynolds number case will be discussed later in this section. For small time delays (high frequencies), the fuel-side CH autocorrelation functions are nearly exponential; however, a significant positive correlation exists for very large time delays (low frequencies), in contrast to the presumed exponential decay. This difference in the autocorrelation functions for large time delays is equivalent to the low-frequency difference in slope for the PSDs.

Since hydroxyl and mixture fraction (Z) autocorrelation functions collapse onto a single curve when normalized by the measured integral time scale, this single time scale is sufficient

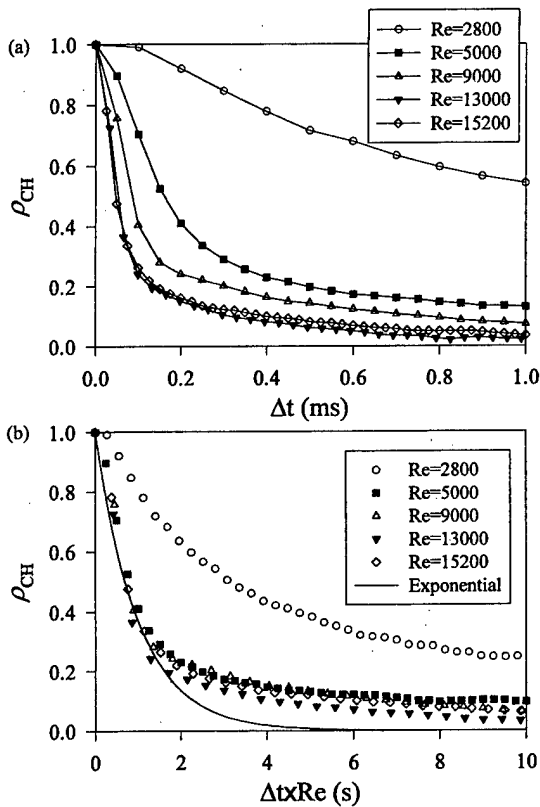


Fig. 5. Fuel-side CH autocorrelation functions for flames A1-A5 at the same locations as in Fig. 2: (a) as measured and (b) scaled by the Reynolds number. The normalized autocorrelation functions are compared to an exponential decay.

for describing the frequency content of the OH and Z fluctuations throughout the flame. In other words, given the integral time scale and its variation in the flame, the entire autocorrelation function is known. For CH, this collapse is not observed completely; in particular, a different form for the autocorrelation function shape and a second time scale would be required to describe the differences between the air- and fuel-side measurements. For this reason, the integral time scale alone is insufficient for normalization of the CH autocorrelation functions. On the fuel-side, where the autocorrelation function decays slowly for large time delays, the integral time scale is much larger than that for the air-side measurements. However, the behavior for small time delays is equivalent at the two measurement locations.

The PSDs and autocorrelation functions in

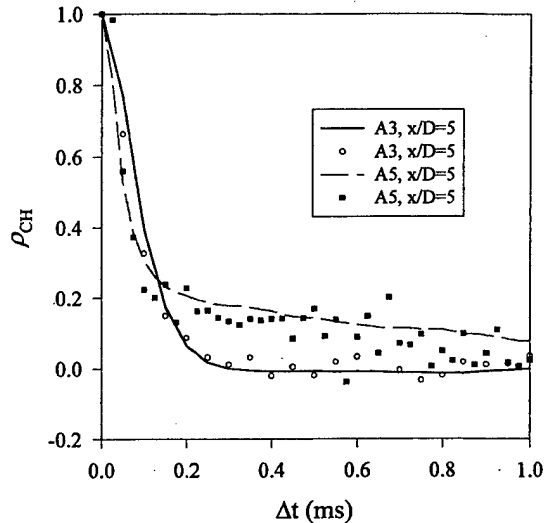


Fig. 6. Comparison of CH fluorescence (lines) and concentration (symbols) autocorrelation functions. The measurements were made ~ 0.5 mm toward the air side of the radial [CH] peak at $x/D = 5$.

Figs. 2-5 were computed from the CH fluorescence time series without correcting for lifetime fluctuations. This simplification provides much cleaner statistics which extend to much higher frequencies. As discussed previously, lifetime variations in these flames are very small and thus are not expected to contribute to the measured spectra. We have further verified this point by comparing lifetime-corrected and -uncorrected statistics at several locations in the flames where the corrected statistics are sufficiently resolved. Figure 6 shows CH fluorescence and CH concentration autocorrelation functions for air-side measurements at an axial height of $x/D = 5$ in flames A3 and A5. The $Re = 9000$ autocorrelation function is nearly exponential (Fig. 4), whereas the $Re = 15,200$ autocorrelation function extends to much longer time delays. In both cases, the lifetime-corrected concentration statistics show the same behavior. This comparison was made for many of the autocorrelation functions shown in Figs. 4 and 5, and in each case the fluorescence and concentration statistics were essentially the same. The lifetime correction procedure also corrects for flame emission background at every point in the time series. Thus, the differences in the autocorrelation functions from the fuel-side

to the air-side of the [CH] peak are real and not a result of lifetime or flame-emission variations.

The extended autocorrelation functions on the fuel side are indicative of fluctuations with a second and longer time scale as compared to the air side. Since the CH time series are highly intermittent (as discussed subsequently), the autocorrelation function is clearly most sensitive to the rates of flame front fluctuations across the fixed laser beam. However, this observation also applies to previous OH measurements, for which the extended autocorrelation function is not observed [8, 9]. The difference may be related to the fact that the CH radical exists farther into the fuel stream than does OH and thus lies closer to the shear layer and the associated region of intense mixture fraction fluctuations, as compared to the measurements made available by Meier [15]. This additional fluctuation mechanism on the fuel side of the [CH] peak may arise from fluctuations in the scalar dissipation rate, particularly since [CH] is sensitive to the local strain rate [19]. NO is also sensitive to the scalar dissipation rate [19, 20]; hence, future measurements of this scalar should permit a better examination of such differences in the autocorrelation function.

At $x/D = 1$ and $x/D = 2$, the CH autocorrelation functions also extend to large time delays on the fuel side of the [CH] peak, except for the two lowest Reynolds number cases (A1 and A2). At these very low axial heights, the flame resides at sufficiently large radial locations such that the local flow is largely unaffected by the turbulent fuel jet. This laminarization of the flame layer can impact the autocorrelation function, as observed for our previous OH measurements [9] and for the present CH measurements in flame A1 (Fig. 5).

At $x/D = 10$, the measured statistics closely follow those at $x/D = 5$. PSDs and autocorrelation functions are shown for the peak [CH] location at $x/D = 10$ in Figs. 7 and 8, respectively. At this height, the $Re = 15,200$ flame (A5) still displays an extended autocorrelation function compared to those at lower Reynolds numbers which are all nearly exponential. However, the difference is less pronounced at $x/D = 10$ than at $x/D = 5$, which may arise from the reduced fluctuations in mixture fraction that occur at larger axial distances [15].

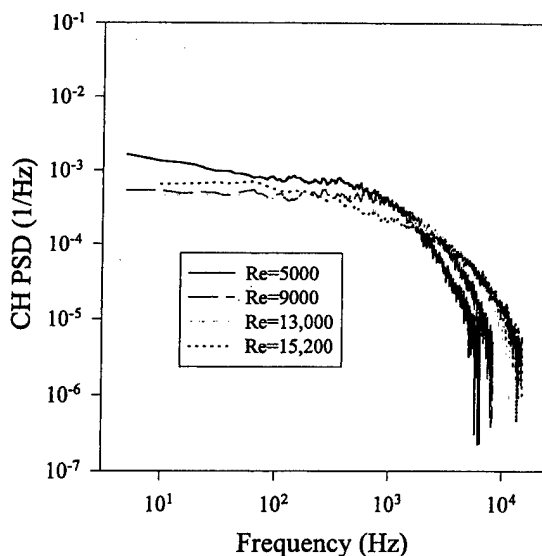


Fig. 7. PSDs at $x/D = 10$ in flames A2–A5. The measurements were taken at the peak [CH] location given in Table 2. The PSDs have been corrected for shot noise and have been filtered by a 5-point moving average.

Figure 9 shows the CH autocorrelation functions for the larger burner flames (D1 and D2) at $x/D = 5$. Comparing Figs. 9a and 4a, it is apparent that the integral time scale for flames D1 and D2 is larger than that for flames A3 and A5, as the autocorrelation function decays more slowly. Hence, simple scaling by only the Reynolds number does not collapse the large burner PSDs onto the small burner PSDs. This result is expected because the integral length scale is directly proportional to the size of the flow [21], in this case the burner diameter, and is also a factor in determining the integral time scale [9, 22]. In Fig. 9b, the autocorrelation functions for the large burner have been normalized by using the Reynolds number and also the ratio of burner diameters for flames A and D (3.4/7.8). This normalization is found to collapse the autocorrelation functions onto the same exponential as in Fig. 4. Moreover, the fuel-side measurements show the same large time-delay extension as in Fig. 5. Therefore, the only substantial effect of altering the burner diameter appears to be a modification of the integral time scale.

Table 3 lists the integral time scales measured at locations for which the autocorrelation function is exponential. As discussed previously, a

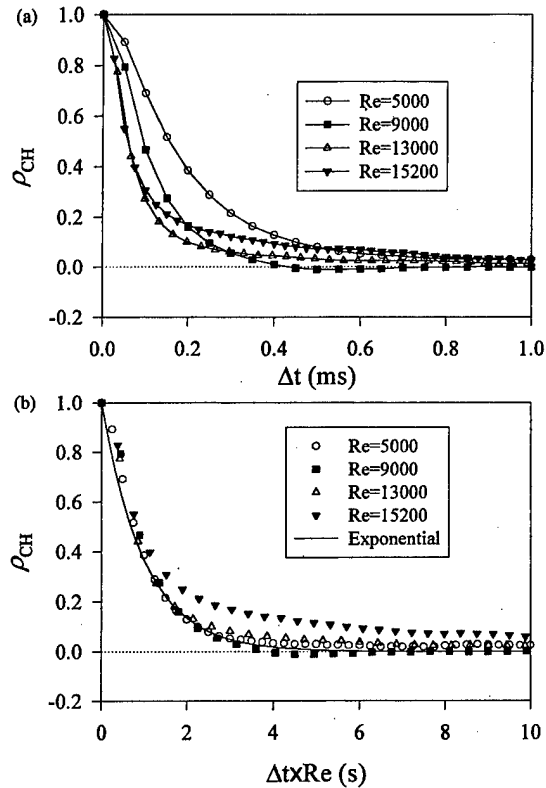


Fig. 8. CH autocorrelation functions for flames A2-A5 at the same locations as in Fig. 7: (a) as measured and (b) scaled by the Reynolds number. The normalized autocorrelation functions are compared to an exponential decay.

second time scale would be required to describe the autocorrelation shape at other locations; thus, the integral time scale alone cannot provide enough information about the scalar fluctuations. For the cases in Table 3, it is clear that the integral time scale decreases for larger Reynolds numbers or for smaller burner diameters. For the normalized autocorrelation functions of Figs. 4, 5, 8, and 9, the integral time scale was assumed to be proportional to $Re^{-1} \cdot D$. We are presently investigating these relationships more thoroughly via detailed hydroxyl measurements in the same series of flames.

The $Re = 15,200$ measurements from the 7.8-mm burner (D2) display an exponential autocorrelation function on the air-side of the [CH] peak (Fig. 9), whereas the air-side autocorrelation function from the 3.4-mm burner is extended for this Reynolds number (Fig. 4).

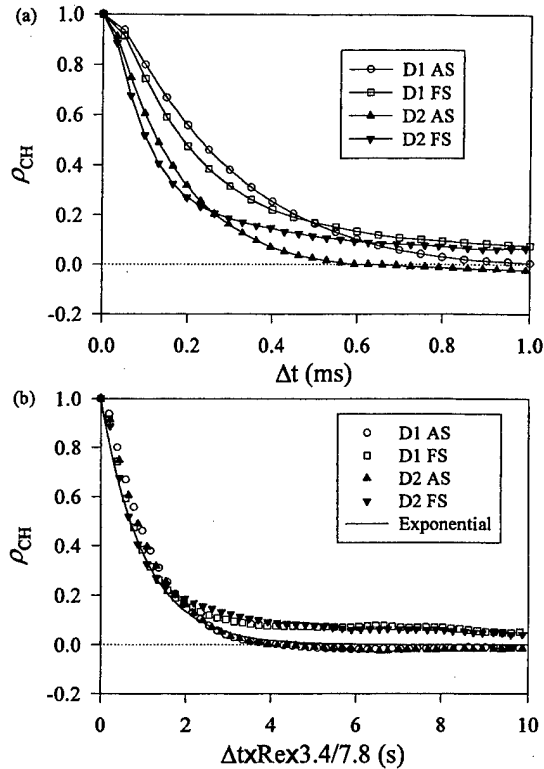


Fig. 9. CH autocorrelation functions for flames D1 and D2 at $x/D = 5$ on both the air-side (AS) and the fuel-side (FS) of the peak [CH] location: (a) as measured and (b) scaled by both the Reynolds number and the ratio of burner diameters (3.4/7.8). The normalized autocorrelation functions are compared to the same exponential decay as shown in Fig. 8.

This feature could also be a scalar dissipation rate effect, as the velocity for the smaller burner is much larger than that for the larger burner (Table 1); however, other possibilities for this difference require examination. Flame A5 is very close to the maximum Reynolds number achievable before the flame extinguishes at the base ($\sim 17,000$). For the 7.8-mm burner, the exit

TABLE 3

Measured Integral Time Scales (ms) at Each Location for Which the Autocorrelation Function Collapses to an Exponential Decay^a

Location	A2	A3	A4	D1	D2
$x/D = 5$ peak	0.22	0.16	0.09	0.25	0.15
$x/D = 5$ air side	0.20	0.09	0.10	0.28	0.13
$x/D = 10$ peak	0.30	0.13	0.11		

^a At other locations, a second time scale is needed to specify the full range of scalar fluctuation rates.

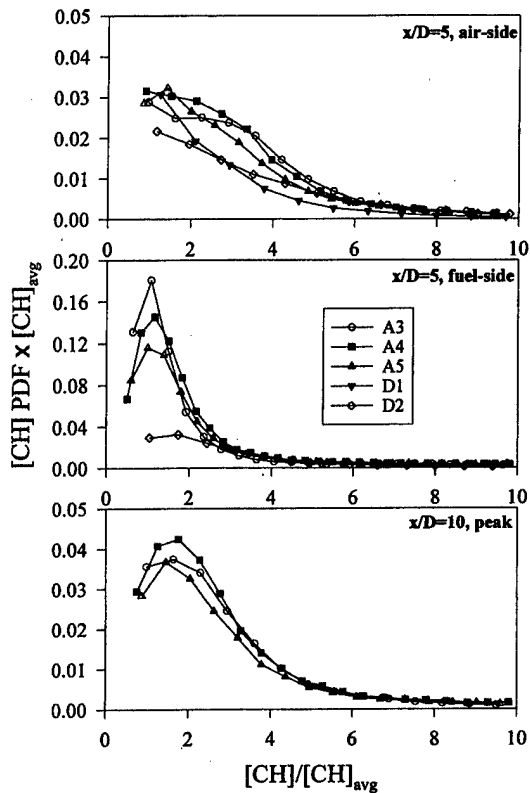


Fig. 10. CH concentration PDFs for flames A3–A5 and D1–D2 computed from the concentration time series at the same locations as the fluorescence autocorrelation functions of Figs. 4, 5, 8, and 9. The PDFs have been normalized by the mean concentrations in Table 2.

velocity at a Reynolds number of 15,200 is much less than that for flame A5, thus reducing the relative strain rate for flame D2. Measurements of other scalars in these flames, particularly OH and NO, which have varying degrees of sensitivity to strain rate, should permit a more thorough examination of the observed differences in these autocorrelation functions.

PDFs

Probability density functions for both the fuel- and air-side measurements at $x/D = 5$ and the peak measurements at $x/D = 10$ are shown in Fig. 10. These PDFs have been computed from the concentration time series and not from the fluorescence time series. The fluorescence time series have a nearly constant background originating from path-integrated flame emission and

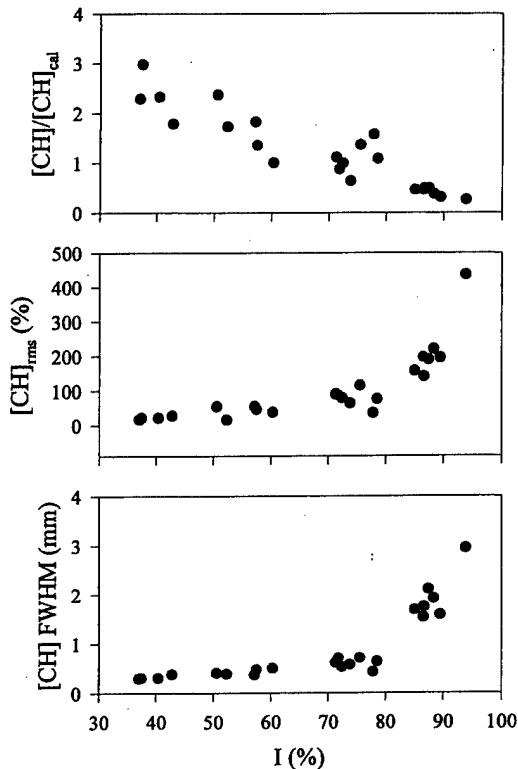


Fig. 11. CH concentration mean, rms, and profile width versus the PDF intermittency factor (I). Data are compiled from all measurements at the peak $[CH]$ location except for flame A1.

PMT dark noise. Although this background does not affect the PSD or autocorrelation function [8], it shifts the PDF and makes interpretation of $[CH] = 0$ difficult; thus the concentration time series are used here for simplicity. As a result, some of the PDFs computed from the concentration time series are dominated by shot noise. These have not been included in Fig. 10.

Each of the PDFs in Fig. 10 is clipped at $[CH] = 0$, where most of the time-series realizations occur. A clipping factor, I , was computed from these PDFs to quantify the resulting CH intermittency. This factor is given for each peak $[CH]$ location in Table 2, and is computed as the ratio of the PDF at $[CH] = 0$ to the sum of the PDF at all concentrations. This ratio represents the probability of measuring $[CH] = 0$ at any point in time within the probe volume.

In Fig. 11, the CH concentration time average, root-mean-square, and profile FWHM are

plotted against the CH clipping factor. Each of these time-averaged quantities shows a strong correlation with I . From Table 2, it appears that the peak [CH] is decreasing significantly with axial height in these flames; however, Fig. 11 shows that much of this decrease is simply due to a larger intermittency. In other words, the peak [CH] may be nearly constant, but since the peak is in the probe volume for less time, the time-averaged [CH] is reduced. Similarly, the increase in width of the time-averaged CH profiles for downstream locations may simply arise from larger fluctuations in absolute flame position. This interpretation of Fig. 11 is consistent with instantaneous CH-PLIF images in nonpremixed flames which show a nearly constant CH width at all axial heights [23]. Thus, the measured CH FWHM (and radial profile) is simply indicative of the PDF for flame-front location.

Although the clipping factor almost completely describes the time-averaged quantities, the shape of the PDF differs slightly from the air- to the fuel-side of the [CH] peak. The air-side PDFs at $x/D = 5$ and the peak PDFs at $x/D = 10$ are nearly identical (Fig. 10), but the fuel-side PDFs at $x/D = 5$ for the 3.4-mm burner contain a much larger percentage of low-[CH] realizations (note the change in scale). Fuel-side measurements in the larger burner are similar to the air-side measurements. Consequently, the clipping factors for the fuel-side measurements in the 3.4-mm burner are notably less than those for the air side (approximately 70% versus 85%). These additional low-[CH] measurements may be related to the low-frequency differences observed in the autocorrelation functions, but more work is needed to determine the origins of these differences.

CONCLUSIONS

CH concentration time-series measurements have been presented in a series of turbulent nonpremixed flames. As with previous hydroxyl measurements, the effects of lifetime fluctuations are minimal in altering time-series statistics such as the PSD, autocorrelation function, or PDF shape. Thus, CH fluorescence time-series statistics can be taken as representative of

[CH]. However, for accurate determination of time-averaged CH concentrations, the spatial variation in average lifetime must generally be considered. For the hydrogen/methane/nitrogen flames considered here, the CH fluorescence lifetimes are only a weak function of location within the flame and thus may be neglected even for the determination of mean [CH], with a resulting error of less than 20%. Comparisons of measured CH lifetimes to those predicted using major species concentrations, temperatures, and quenching cross-section data from the literature show a 30% overprediction by the model, in agreement with previous studies [18]. However, the lack of significant lifetime variations in our flames makes this comparison insensitive to potentially incorrect trends in the model.

Comparison of the present CH statistics to those reported for OH in hydrogen/argon nonpremixed turbulent jet flames shows nearly identical autocorrelation functions for regions away from the turbulent fuel jet (closer to the ambient air). Both OH and CH autocorrelation functions in these regions are nearly exponential for $Re > 3000$ and $x/D > 2$, in agreement with mixture fraction measurements from turbulent nonpremixed CO jet flames [13]. For lower Reynolds numbers or axial heights, the autocorrelation functions are more representative of laminar flow. The collapse of the measured autocorrelation functions onto a single curve for $Re > 3000$ and $x/D > 2$ implies that a single time scale is appropriate for describing minor-species concentration fluctuations in these regions. This time scale was found to vary directly with the burner diameter and inversely with the Reynolds number, although only a narrow range of conditions has been considered to date.

Radial profiles for CH extend much further into the fuel jet than do those for hydroxyl; thus, the CH radical exists closer to the shear layer and to the peak of mixture fraction fluctuations. In this region of the jet, CH autocorrelation functions were found to differ from both hydroxyl and mixture fraction statistics in the literature. It appears that a single time scale cannot capture all CH fluctuations throughout these flames. However, high-frequency fluctuations for CH were found to follow an exponen-

tial autocorrelation function even toward the fuel stream. Only the low-frequency behavior was altered in this region.

For both OH and CH, a significant percentage of time-series points indicates the absence of minor species (arising from the flame having fluctuated away from the fixed laser beam). For such high scalar intermittency, time-scale statistics are most sensitive to the rates of flame front fluctuations and relatively insensitive to the absolute fluctuations of OH or CH concentrations within the flame. However, if flame-front fluctuations were the only factor affecting the PSDs and autocorrelation functions, no differences would be observed between CH and OH measurements. Hence, the discrepancy between the CH and OH statistics in these flames could be a result of the increased sensitivity of [CH] to the local scalar dissipation rate and to the closer proximity of peak [CH] to the shear layer. However, other possible effects must be examined. We are presently applying the upgraded PITLIF technique to measurements of OH and NO, and are incorporating Rayleigh scattering for temperature time-series measurements, in the same $H_2/CH_4/N_2$ flames. Hence, comparisons among multiple scalars can be made more clearly in the future; in particular, differences in their statistics can be further examined so as to gain additional insight on chemistry-turbulence interactions in nonpremixed flames.

This research was supported by the Air Force Office of Scientific Research, with Julian Tishkoff serving as technical monitor, and by a Department of Defense Fellowship. We also acknowledge ongoing discussions with Professor Jay Gore (Purdue University) concerning data analysis and interpretation.

REFERENCES

1. Barlow, R. S., Dibble, R. W., Chen, J.-Y., and Lucht, R. P., *Combust. Flame* 82:235 (1990).
2. de Vries, J. E., van der Meer, T. H., and Hoogendoorn, C. J., *Chem. Eng. J.* 53:39 (1993).
3. Chen, Y.-C., and Mansour, M. S., *Twenty-Sixth Symposium (International) on Combustion*, The Combustion Institute, Pittsburgh, 1996, p. 97.
4. Renfro, M. W., Klassen, M. S., King, G. B., and Laurendeau, N. M., *Opt. Lett.* 22:175 (1997).
5. Renfro, M. W., Pack, S. D., King, G. B., and Laurendeau, N. M., *Combust. Flame* 115:443 (1998).
6. Pack, S. D., Renfro, M. W., King, G. B., and Laurendeau, N. M., *Opt. Lett.* 23:1215 (1998).
7. Pack, S. D., Renfro, M. W., King, G. B., and Laurendeau, N. M., *Combust. Sci. Technol.* 140:405 (1999).
8. Renfro, M. W., King, G. B., and Laurendeau, N. M., *Appl. Opt.* 38:4596 (1999).
9. Renfro, M. W., Gore, J. P., King, G. B., and Laurendeau, N. M., *AIAA J.*, in press.
10. Wygnanski, I., and Fiedler, H., *J. Fluid Mech.* 38:577 (1969).
11. Birch, A. D., Brown, D. R., Dodson, M. G., and Thomas, J. R., *J. Fluid Mech.* 88:431 (1978).
12. Becker, H. A., Hottel, H. C., and Williams, G. C., *J. Fluid Mech.* 30:285 (1967).
13. Kounalakis, M. E., Sivathanu, Y. R., and Faeth, G. M., *J. Heat Trans.* 113:437 (1991).
14. Bergmann, V., Meier, W., Wolff, D., and Stricker, W., *Appl. Phys. B* 66:489 (1998).
15. Meier, W., DLR Stuttgart, Experimental Data Archives, <http://www.st.dlr.de/EN-CV/flamedat/intro.htm> (1999).
16. Seitzman, J. M. (1991). Ph.D. thesis, Stanford University, Palo Alto, CA.
17. Renfro, M. W., Pack, S. D., King, G. B., and Laurendeau, N. M., *Appl. Phys. B* 69:137 (1999).
18. Tamura, M., Berg, P. A., Harrington, J. E., Luque, J., Jeffries, J. B., Smith, G. P., and Crosley, D. R., *Combust. Flame* 114:502 (1998).
19. Thomsen, D. D., Ravikrishna, R. V., Laurendeau, N. M., and Gore, J. P., *Proceedings of the Central States Section Meeting*, The Combustion Institute, Lexington, KY, 1998, p. 339.
20. Sanders, J. P. H., Chen, J.-Y., and Gökalp, I., *Combust. Flame* 111:1 (1997).
21. Tennekes, H., and Lumley, J. L., *A First Course in Turbulence*, The MIT Press, Cambridge, MA, 1972.
22. Magre, P., and Dibble, R., *Combust. Flame* 73:195 (1988).
23. Carter, C. D., Donbar, J. M., and Driscoll, J. F., *Appl. Phys. B* 66:129 (1998).

Received 26 July 1999; revised 28 January 2000; accepted 28 January 2000

Scalar Time-Series Measurements in Turbulent CH₄/H₂/N₂ Nonpremixed Flames: OH

MICHAEL W. RENFRO, WALTER A. GUTTENFELDER, GALEN B. KING, AND
NORMAND M. LAURENDEAU

School of Mechanical Engineering, Purdue University, West Lafayette, IN 47907, USA

Time-series measurements of OH concentrations are reported for simple jet diffusion flames using a fuel mixture of hydrogen, methane, and nitrogen. Five Reynolds numbers and two burner diameters are examined. Autocorrelation functions were computed from the time series and were used to calculate integral time scales for many axial and radial locations in each jet. The autocorrelation functions are found to collapse when normalized by the integral time scale, indicating that a single time scale adequately characterizes the full range of scalar fluctuations. The evolution of the integral time scales is assessed with respect to Reynolds number, axial height, radial location, and burner diameter. The time scales are found to decrease as $Re^{-1.4}$, which is in contrast to the usual Re^{-1} dependence for mixture fraction and velocity in nonreacting jets. The OH time scales are found to be complicated functions of radial location and do not follow the scaling expected from nonreacting flows. © 2000 by The Combustion Institute

INTRODUCTION

Measurements of minor-species concentrations in turbulent flames are of interest owing to their importance in pollutant chemistry and to their use as markers of instantaneous flame structure. Hydroxyl (OH), nitric oxide (NO), and methylidyne (CH) measurements have been reported by many researchers in a wide variety of flames; however, most of these studies have employed high-power, low-repetition-rate, pulsed lasers. With such instrumentation, two sequential measurements are further apart in time than most correlations arising from turbulent fluctuations. Thus, the measurements are temporally independent from one shot to the next and yield only single-time statistics, including the mean, variance, and probability density function (PDF). Accurate prediction of scalar PDFs (and in many cases just the mean) are sufficient for most engineering applications. However, current model closure assumptions and the resulting predictions are not yet adequate as design tools. Hence, turbulent combustion models will benefit from a better physical understanding of turbulent flames, including an understanding of the rates of flame-front fluctuations and the effects of turbulence-chemistry interactions.

Many diagnostic techniques have been developed to provide novel data that may better

address these issues. For example, multiscale measurements have provided conditional scalar statistics [1] and multipoint measurements have provided spatial-scale information [2,3] in turbulent jet flames. Time-scale information can be provided by scalar time series when measurement repetition rates are sufficiently fast to resolve turbulent fluctuations. This approach has been demonstrated for many scalars such as temperature [4] and, more recently, concentrations of CH [5] and OH [6]. These time series of minor-species concentrations are recovered by use of picosecond time-resolved laser-induced fluorescence (PITLIF), which directly accounts for potential variations in both the electronic quenching rate coefficient and the background flame emission.

In the present study, time-series measurements are utilized to determine temporal scales of [OH] fluctuations in a series of turbulent hydrogen/methane/nitrogen jet-diffusion flames. The chosen fuel mixture has been studied previously by Bergmann et al. [7] using low-repetition-rate diagnostics. These authors report conditional statistics for major-species concentrations and temperature and provide images of OH, CH, NO, and temperature. Much of this data is available via the internet [8]. The measurements reported here represent an ongoing effort to characterize scalar time series for these specific flames, which complements the data provided by Bergmann et al. [7].

Corresponding author. E-mail: renfro@ecn.purdue.edu

CH [5] measurements have already been reported as well as mixture fraction measurements from a nonreacting jet [9] using the same burner and fuel density as for the present measurements, but with no heat release. Temperature measurements are planned for the same flames in the near future.

As with our previous OH measurements in H_2/Ar flames [6], the OH fluorescence lifetime was simultaneously measured in the present $H_2/CH_4/N_2$ flames. While important for mean OH concentrations and quantitative PDFs, the lifetime measurements prove to be unimportant for determination of temporal statistics. Power spectral densities (PSDs), autocorrelation functions, and PDFs were computed from the concentration time series and are compared for many axial and radial locations in the jet, for five Reynolds numbers, and for two burner diameters.

Hydroxyl PSDs and autocorrelation functions have previously been found to collapse onto a single curve when normalized by the measured integral time scales in H_2/Ar flames [10]. This collapse indicates that the range of time scales for OH fluctuations at each measurement location can be fully characterized by a single representative time scale. A similar collapse is also observed for the present data, although here a larger range of conditions is studied so that the effects of Reynolds number and location within the jet can be better estimated. The range of conditions for which the measured PSDs and autocorrelation functions are statistically self similar is characterized and is found to closely follow the collapse of other time-averaged statistics. The OH time scales are also found to depart from traditional eddy-turn-over time scaling, which has been effectively demonstrated for velocity and passive scalars in nonreacting jets.

METHODS

The laser system used for the present hydroxyl measurements is identical to that employed by Renfro et al. [6]. Briefly, the IR output of an argon-ion pumped Ti:Sapphire laser was frequency tripled to produce an 80-MHz repetition rate, 18-ps FWHM pulse stream at 309.33 nm

(0.02-nm FWHM). The laser was focused over the burner and excited the $Q_1(8)$ transition within the (0,0) vibrational band of the $X^2\Pi-A^2\Sigma$ electronic system of OH. This wavelength was chosen to minimize the temperature dependence of the Boltzmann fraction. Based on full simulations of OH absorption using a code developed by Seitzman [11], this spectral location produces an absorption coefficient variation of only $\pm 5\%$ from 1500 to 2250 K.

The detection system used for the present study is also identical to that employed for our previous hydroxyl measurements [6]. Fluorescence photons were collected by a 0.25-m monochromator and a Hamamatsu HS5321, 700-ps risetime photomultiplier tube (PMT). The spatial resolution was $100 \times 100 \times 60 \mu m^3$ based on the beam diameter (e^{-2}) and the monochromator entrance slit width. The spectral resolution was 10 nm centered at 309 nm. Each pulse from the PMT (corresponding to a single photoelectron) was counted using the methodology of Pack et al. [12], which divides the signal into three 3.5-ns gated bins locked to the arrival time of the laser pulse. The photon counts in each bin were integrated for a period of time equal to the inverse of the sampling rate, which produced three separate but simultaneous time series. These time series were converted to two time series representing concentration and fluorescence lifetime by using a code developed by Renfro et al. [13].

The resulting OH concentration time series were calibrated against a premixed $CH_4/N_2/O_2$ flame ($\phi = 0.8$, $[N_2]/[O_2] = 3.1$) stabilized on a water-cooled McKenna burner. The calibration was performed at an axial height of 8 mm owing to the stability, repeatability, and relative spatial invariance at this location. The concentration at this point was computed by using the Sandia PREMIX flame code [14] and GRIMech 2.11 [15] and found to be 5.7×10^{-9} moles/cm³. We have verified this prediction (within 10%) via an arc-lamp absorption measurement. Fluorescence lifetimes for OH were calibrated against measurements in seven standard liquid solutions as described by Pack et al. [12].

Concentration measurements were made in seven jet diffusion flames with a fuel composition of 33.2% H_2 , 22.1% CH_4 , and 44.7% N_2 (by volume). The fuel issued from a circular nozzle

TABLE 1
Burner and Flow Parameters for the Seven Flames
Examined in This Study

Flame	Burner Diameter (mm)	\bar{V} (m/s)	Re	Sampling rate (Hz)
A1	3.4	16.3	2800	10,000
A2	3.4	29.0	5000	12,500
A3	3.4	52.3	9000	20,000
A4	3.4	75.5	13,000	27,027
A5	3.4	88.3	15,200	31,250
D1	7.8	22.8	9000	10,000
D2	7.8	38.5	15,200	20,000

The Reynolds number is computed from the average velocity and the cold-flow properties of the fuel mixture (33.2% hydrogen, 22.1% methane, 44.7% nitrogen). The sampling rates for the time-series measurements are also given for each flame.

into still air with cold-flow Reynolds numbers ranging from 2800 to 15,200. Two burners were examined with diameters of 3.4 and 7.8 mm. In both cases the burners were sufficiently long to provide fully developed turbulent flow at the tube exit. The tubes were not contoured and no coflow or pilot flame was provided. The seven flames studied are designated A1–A5 and D1–D2, as shown in Table 1. Radial profiles of time-averaged [OH] were obtained at $x/D = 1, 2, 5, 10, 20, 40,$ and 60 in each 3.4-mm flame and at $x/D = 1, 2, 5, 10,$ and 20 in each 7.8-mm flame by using a sampling rate of 10 Hz and an averaging time of 3 s. At each height, time-series measurements were obtained with sampling rates as given in Table 1 for three radial locations displaying significant OH signals (135 total locations).

Fifty time series of 4096 points each were collected to obtain clean statistics at each measurement location. PDFs, PSDs, autocorrelation functions, and integral time scales were computed from these time series in the same manner as reported by Renfro et al. [6, 10], including a correction for the measured contribution of shot noise. We have compared the integral time scales recovered at much lower signal-to-noise ratios (SNRs) by decreasing the laser power (6–8 mW versus 18–20 mW) and find no significant differences in the measured trends. The results agree within 20% on the average, which is within our estimated accuracy of $\pm 22\%$ (95% confidence interval) for these data [10].

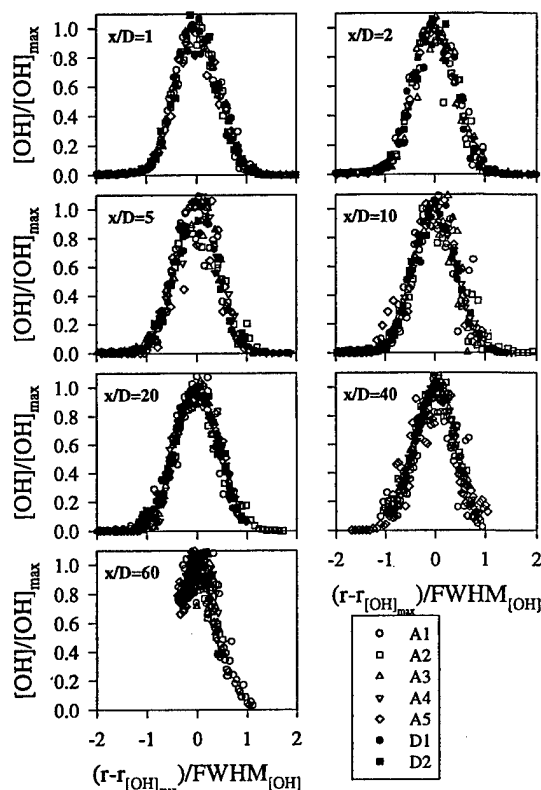


Fig. 1. Radial profiles of time-averaged [OH] at various heights in each flame. The profiles have been normalized by the peak concentration, the profile peak location, and the profile FWHM as listed in Table 2. Each profile is nearly Gaussian in shape.

RESULTS

Time-Averaged Profiles

Figure 1 shows the radial profiles measured for time-averaged [OH] at each height in all seven flames. For each individual radial profile measurement, a Gaussian function was fit to the data using a least-squares algorithm to determine the time-averaged [OH] peak, profile full-width at half-maximum (FWHM), and peak radial location. These values have been used to normalize the profiles of Fig. 1 to simplify the data presentation. Although this procedure is not meant to imply that a Gaussian shape is physically correct, we observe that every profile in each flame and at all heights can be accurately represented by this particular shape. The numerical values of the three normalization

TABLE 2
Hydroxyl Concentration and Fluorescence Lifetime Statistics for Radial Locations of
Peak [OH]

Flame	x/D	r/x	$[\text{OH}]_{\text{max}}$ (10^{-8} moles/cm ³)	$[\text{OH}]_{\text{rms}}$ (%)	FWHM (mm)	τ (ns)	I (%)
A1	1	1.18	5.31	3.8*	1.14	1.37	0.0
A1	2	0.68	4.83	5.9*	1.41	1.43	0.0
A1	5	0.31	4.08	6.5*	1.62	1.38	1.4
A1	10	0.18	3.59	29.4*	1.94	1.38	10.5
A1	20	0.10	2.85	36.1*	3.24	1.48	30.4
A1	40	0.06	1.68	46.3*	7.44	1.58	48.9
A1	60	0.02	1.98	57.9*	13.97	1.64	75.0
A2	1	1.08	7.28	9.0*	0.96	1.38	0.4
A2	2	0.61	6.78	7.0*	1.26	1.39	0.5
A2	5	0.27	5.59	4.3*	1.27	1.46	2.3
A2	10	0.16	4.60	26.1*	1.52	1.51	7.1
A2	20	0.11	3.37	42.0*	3.03	1.60	38.1
A2	40	0.08	2.28	55.2*	9.83	1.69	72.2
A2	60	0.02	2.15	75.9*	30.32	1.67	78.4
A3	1	0.93	7.30	10.7*	0.74	1.29	0.5
A3	2	0.50	7.89	0.5*	0.77	1.31	0.4
A3	5	0.24	6.43	20.8	0.85	1.34	4.3
A3	10	0.15	4.08	43.9	1.57	1.47	18.7
A3	20	0.11	2.06	78.6	3.59	1.62	47.4
A3	40	0.09	1.54	77.4	12.07	1.68	61.9
A3	60	0.04	1.40	60.3*	26.60	1.67	74.3
A4	1	0.83	7.22	18.6*	0.50	1.34	3.2
A4	2	0.45	7.68	17.1*	0.53	1.36	3.5
A4	5	0.22	5.04	36.8	0.79	1.51	17.7
A4	10	0.14	2.97	71.4	1.71	1.64	41.6
A4	20	0.11	1.96	88.8	3.80	1.73	54.4
A4	40	0.08	1.70	92.7	11.18	1.78	65.9
A4	60	0.04	1.66	68.0*	25.86	1.80	70.8
A5	1	0.80	8.33	15.5*	0.41	1.54	4.6
A5	2	0.43	6.10	24.4*	0.47	1.55	17.0
A5	5	0.21	3.50	60.4	0.77	1.71	49.2
A5	10	0.15	1.86	87.3	1.36	1.78	70.0
A5	20	0.11	1.81	94.1	3.37	1.79	67.8
A5	40	0.09	1.54	80.2	6.86	1.82	62.0
A5	60	0.07	1.56	51.1*	34.12	1.87	88.2
D1	1	0.84	7.19	7.6*	1.18	1.46	0.1
D1	2	0.43	7.87	6.5*	1.25	1.36	0.1
D1	5	0.21	5.46	29.5	1.89	1.38	12.3
D1	10	0.13	3.63	54.9	3.55	1.48	33.2
D1	20	0.08	2.05	81.0	10.78	1.64	61.3
D2	1	0.73	7.58	12.5*	0.78	1.40	3.2
D2	2	0.40	5.93	24.9*	0.90	1.51	3.7
D2	5	0.20	4.49	46.8	1.70	1.58	26.5
D2	10	0.13	2.69	76.2	4.46	1.69	55.6
D2	20	0.09	1.97	94.9	12.25	1.73	67.7

The radial location (r/x) and profile width (FWHM) were determined by fitting a Gaussian profile to the time-average radial profile measurements. $[\text{OH}]_{\text{max}}$, $[\text{OH}]_{\text{rms}}$, fluorescence lifetime (τ) and OH intermittency (I) were determined from time-series measurements at the peak location. Concentrations were calibrated against a measurement in a lean premixed flat flame.

* Uncertainty greater than 10% owing to excessive shot noise [6].

parameters are given in Table 2, along with the [OH] root-mean-square (rms), time-averaged fluorescence lifetime, and intermittency parameter (which is defined and discussed later).

The accuracy of these measurements has been partially assessed by repeating all radial profile and time-series measurements in flames A1, A2, A3, and A5 with much lower SNRs. For a single measurement, the peak [OH] location (r/x) is determined with a precision of $\pm 4.2\%$ (95% confidence interval) up to $x/D = 40$. The profile width (FWHM) is determined with a precision of $\pm 7.4\%$ up to $x/D = 40$. The peak [OH] accuracy is dominated by the repeatability of the calibration measurement, which involves replacing the turbulent tube burner with a McKenna burner and comparing OH signals obtained within a short period of time. This process was repeated several times and demonstrated a total uncertainty of 10.1% (95% confidence interval).

Except for $x/D = 60$, all heights display two separate OH peaks on either side of the jet centerline. At $x/D = 60$, the peak OH concentration occurs near the centerline such that some flames (particularly $Re = 2800-9000$) appear to have a unimodal OH distribution. At each height below $x/D = 60$, time-series measurements were acquired at the location of maximum [OH] and on both sides of the OH peak at those radial locations where the time-averaged [OH] was approximately half of its maximum value. At $x/D = 60$, a time-series measurement was made at the jet centerline, at the peak [OH] location, and at the half-concentration point on the air side of the OH peak.

Time-Series Statistics

Sample time series for flames A1, A3, A5, and D2 are shown in Fig. 2. These measurements were made at the radial location of peak [OH] at $x/D = 20$. The traces represent the first 20 ms of data collected at each location and were not selected to demonstrate any particular feature of the measurement. The primary goal of this research is to characterize the rates of scalar fluctuations in nonpremixed jet flames. From Fig. 2 it is clear that a range of fluctuation time scales is present, even at a single location in the flow, and that the fluctuation rates depend

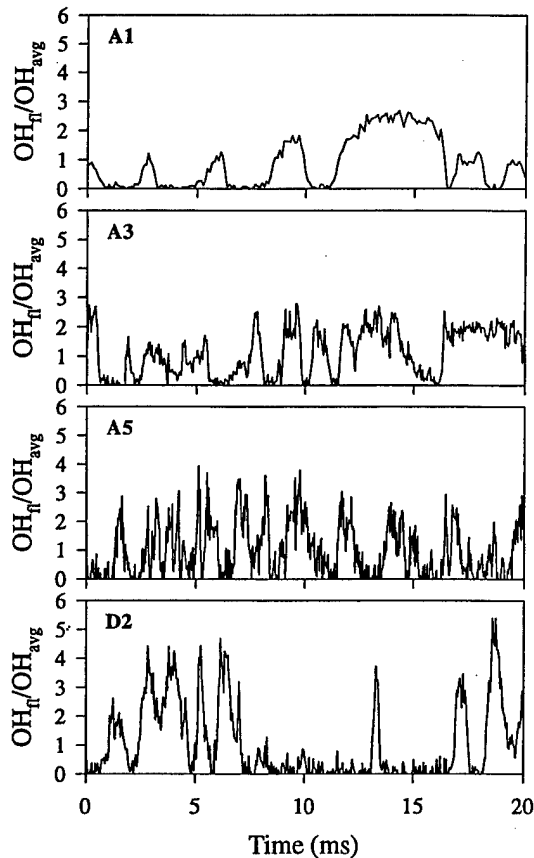


Fig. 2. Sample time series of OH fluorescence in flames A1, A3, A5, and D2. These time series were collected at the peak [OH] location for $x/D = 20$. The sampling rates for these measurements are given in Table 1. For each time trace, only the first 20 ms of data are presented.

strongly on the Reynolds number. In each flame, the OH concentration becomes zero many times as the OH layer fluctuates completely away from the fixed laser beam. These intermittent periods are typically longer in flame A1 than in flame A5. Likewise, periods for which measurable OH exists in the probe volume ($[OH] > 0$) display a longer duration at lower Re . Thus, these time series visually demonstrate that OH-fluorescence fluctuations occur more rapidly at higher Re . Flame D2 displays fluctuations that are more similar to flame A3 than to flame A5, indicating that the larger burner diameter serves to slow down the scalar fluctuations.

The fluctuation rate variations visible in Fig. 2 are quantifiable in terms of the power spectral

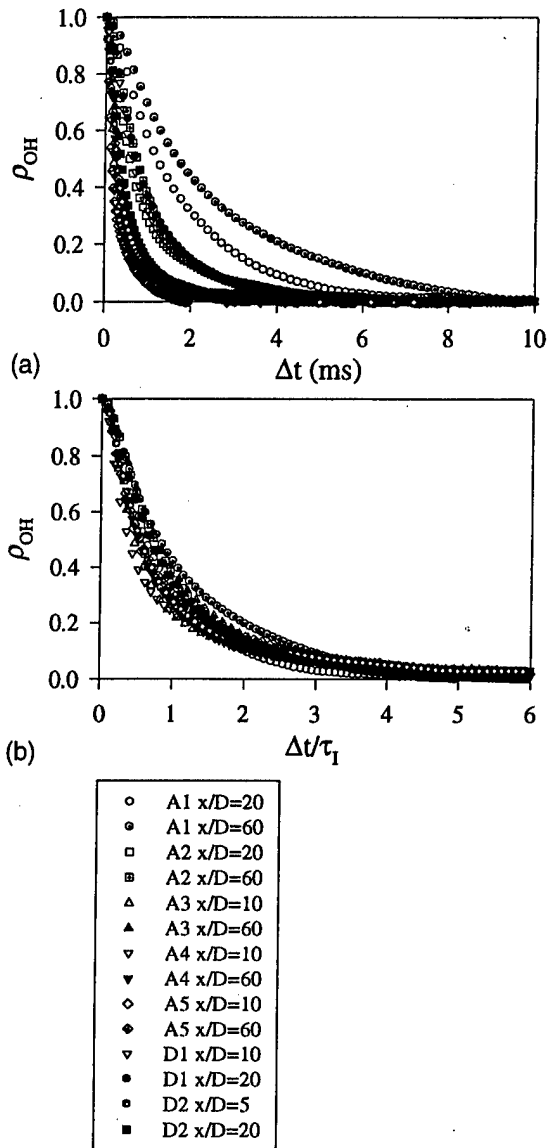


Fig. 3. Autocorrelation functions for the radial location of peak [OH] at various axial heights in each flame, (a) as measured and (b) upon normalization by the integral time scale.

density and the autocorrelation function. Figure 3a shows autocorrelation functions for the radial location of peak [OH] at two heights in each of the seven flames. Measurements in the near field of the jet have intentionally been removed from this plot and will be discussed subsequently. The downstream measurements presented in Fig. 3a display decays that are significantly different from one another. In par-

ticular, the autocorrelation functions for flames at higher Re are observed to decay much faster than for those at lower Re. This result is a manifestation of the faster fluctuations observed at greater Re in the time traces of Fig. 2. The integral time scale, τ_I , for each measurement location is useful in characterizing these differences and can be computed by numerically integrating its autocorrelation function. A previously developed technique utilizing the measured PSDs was employed to eliminate the effects of shot noise on the computed τ_I [10].

Figure 3b shows the same autocorrelation functions normalized by the derived integral time scales. The normalized functions collapse to essentially a single curve. Since the PSD is a Fourier transform pair to the autocorrelation function, the collapse is observed equally in the frequency-domain statistics. This feature of OH fluctuation time scales was first shown for measurements in H_2/Ar flames by Renfro et al. [10]. The collapse of a two-time statistic (either the autocorrelation function or PSD) implies that the relative distribution of fluctuation rates at a single point in a turbulent flow is the same as that at a different point (even in a different flow). Hence, the slowest fluctuations in flame A1 become faster in flame A5 at the exact same ratio as do the fastest fluctuations in these two flames (see Fig. 2). Thus, the integral time scale is a good representation of temporal variations in [OH] for the two cases. For these flames, the collapsed autocorrelation function is nearly exponential (although this shape cannot be physically correct near $\Delta t = 0$). This particular shape is consistent with OH measurements in hydrogen/argon flames [10], and also with CH measurements reported in these same hydrogen/methane/nitrogen flames [5].

The self similarity of the OH PSDs and autocorrelation functions is only valid sufficiently downstream of the jet exit. Note that data for $x/D = 1$ and $x/D = 2$ (and larger heights for lower Re) is not included in Fig. 3. Two sample autocorrelation functions for these two heights are shown in Fig. 4. These two functions were measured in flame A3 at the radial location of peak [OH]. At $x/D = 2$, the OH fluctuations remain correlated for long periods of time (> 50 ms), especially when compared to the downstream data that become uncorrelated

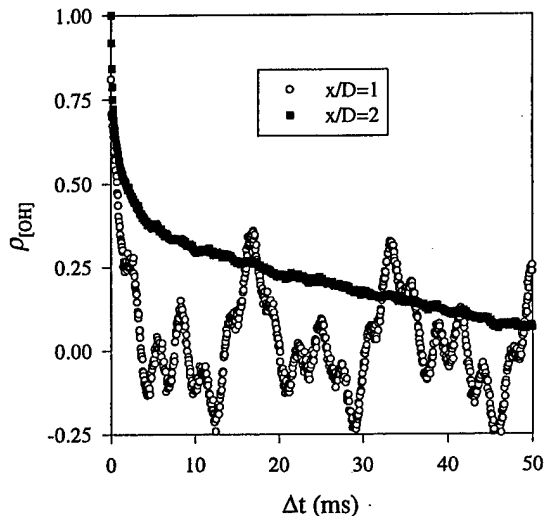


Fig. 4. Hydroxyl autocorrelation functions for the radial location of peak [OH] at $x/D = 1$ and $x/D = 2$ in flame A3. The measurements do not collapse to an exponential function and are more representative of an unsteady laminar flow.

by $\Delta t > 10$ ms even for the lowest Re flow. Hence, the fluctuations at $x/D = 2$ are much slower (lower frequencies) than those incorporated into Fig. 3. At $x/D = 1$, the autocorrelation function is periodic, which is indicative of a periodic time series. Both autocorrelation functions can arise from nearly laminar but unsteady flow.

This feature is consistent with images of the reaction zone in the near field of jet diffusion flames. Clemens and Paul [16], for example, present simultaneous, instantaneous images of OH and fuel (via acetone seeding) in several hydrogen/nitrogen flames. Even at $Re = 50,000$, the OH layer lies far from the fuel core at heights below $x/D = 2.5$ and is barely contorted by the fuel turbulence. The peak [OH] locations in Table 2 also show that the OH layer is at a much larger value of r/x for axial heights below $x/D = 10$ than for the downstream locations. We find that our data collapses to an exponential autocorrelation function for any measurement made at a radial location $r/x < 0.16$ (close to the fuel core), and is different (as in Fig. 4) for measurements at $r/x > 0.16$. For all flames, the nonexponential measurements are limited to axial heights below $x/D = 20$. Thus, it appears that laminarization of the OH layer in the near

field is a feature of turbulent flames, which must be addressed separately. In the present work, we focus on the statistics of only those downstream regions where the time-scale statistics are self similar.

Integral Time Scales

If an integral time scale is specified, a normalized exponential autocorrelation function can be used to approximate the entire distribution of OH fluctuation time scales for locations sufficiently far downstream. Thus, the task of describing OH fluctuations throughout the various jet flames is reduced to describing only the integral time scales. However, even in the case of self-similar jets, τ_I is a function of the Reynolds number, axial height, radial location, and jet diameter. In particular, Renfro et al. [10] found that τ_I increases for OH as the axial height or radial location increases and as the Reynolds number decreases for their hydrogen/argon flames. Simple eddy-turn-over time scaling and the Taylor hypothesis can be used to capture these trends by assuming that the integral time scale for scalars is proportional to the jet width divided by the local mean velocity. For a fixed diameter jet, these assumptions lead to [10]

$$\tau_I \sim \left(\frac{1}{Re}\right) \left(\frac{x}{D}\right)^2 \left(\frac{U_{CL}(x/D)}{U(r/x)}\right) \quad (1)$$

where $U(r/x)$ is the local mean velocity and U_{CL} is the mean velocity on the jet centerline. Although this scaling was qualitatively consistent with previous hydrogen/argon flame data, measurements were only obtained up to $x/D = 20$ at five Reynolds numbers and the radial dependence could not be adequately separated from the axial dependence. These relationships can now be examined in more detail.

Figure 5 shows OH integral time scales measured at $x/D = 40$ in the five 3.4 mm diameter flames. A power-law fit to the data demonstrates that $\tau_I \sim Re^{-1.51 \pm 0.23}$ best represents the Reynolds number dependence. In contrast, velocity and mixture fraction statistics from the literature display a Re^{-1} dependence for non-reacting jets [17–19]. However, to our knowledge, no study has systematically examined mix-

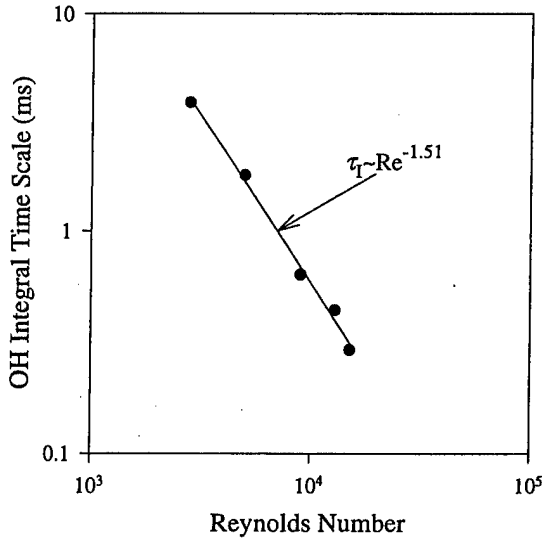


Fig. 5. Hydroxyl integral time scales at $x/D = 40$ as a function of Reynolds number for flames A1-A5. All measurements were made near $r = 11.5$ mm. The integral time scales have been corrected for the effects of shot noise as discussed by Renfro et al. [10].

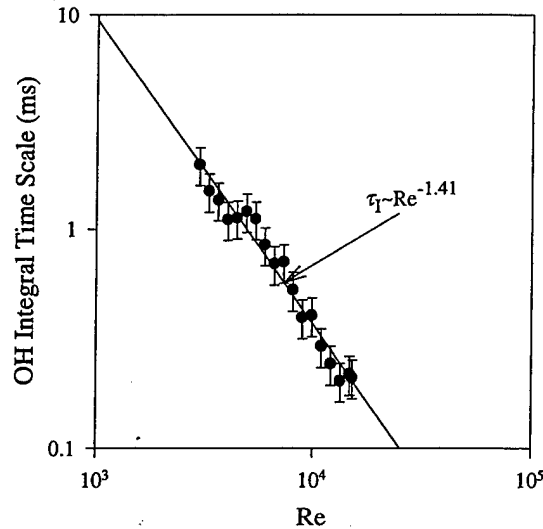


Fig. 6. Hydroxyl integral time scales at $x/D = 20$ as a function of Reynolds number for eighteen different flames. All measurements were made at $r = 5.1$ mm.

ture fraction time scales in flames, although some sparse data exists [20].

To better resolve the cursory relationship shown in Fig. 5, a series of measurements were made in the 3.4 mm burner of hydrogen/methane/nitrogen flames by fixing the laser beam at a single radial position at $x/D = 20$ for eighteen Reynolds numbers ranging from 2980 to 15,200. This height was chosen since the OH peak locations (Table 2) do not vary much with Re; consequently, the fixed laser beam was at the same relative location on each [OH] profile. Figure 6 shows the integral time scales determined from these eighteen flames. In each case, the autocorrelation function was found to collapse to an exponential function as effectively as those shown in Fig. 3. Measurements were extended to much lower Reynolds numbers through transition, even including some flickering laminar flames (down to $Re = 330$). These autocorrelation functions are significantly different (as in Fig. 4) and the integral time scales from these measurements are not included in Fig. 6.

For the range $Re = 2980-15,200$, the integral time scales are proportional to $Re^{-1.41 \pm 0.15}$ at the 95% confidence interval. It is interesting to note that if one assumes a Re^{-1} dependence

and plots τ_I versus $1/Re$ to confirm the linear relationship, a wide range of Re exponents will display correlation coefficients greater than 0.95 unless the least-squares fit is through the origin. For our previous OH measurements in hydrogen/argon flames, we demonstrated a Re^{-1} dependence on the integral time scale by using this approach. A reexamination of this data finds $\tau_I \sim Re^{-1.15 \pm 0.24}$. The increased uncertainty in the H_2/Ar data and the data of Fig. 5 arises from having only five Reynolds numbers. Thus, while the previous data might still be proportional to $1/Re$, the current data cannot and it appears most likely that both sets of OH integral time scales are decreasing with Reynolds number faster than Re^{-1} .

The faster decrease of OH integral time scales with Re as compared to mixture fraction is somewhat surprising since OH is reasonably well described by the laminar flamelet approximation. On the other hand, since these measurements are made at a fixed axial height, any shift in the virtual origin with Reynolds number could cause an enhanced change in the integral time scale. We are currently examining this potential artifact through other scalar measurements in the same flames. However, the dependence on Re may also arise because Eq. 1 is simply invalid for reacting jets. The OH mea-

measurements alone are not sufficient to fully resolve these issues.

The OH integral time scales also change as a function of x/D and r/x in the nonpremixed jet flames. Renfro et al. [10] found their OH time scales to be consistent with the radial scaling provided by Eq. 1 based on a velocity profile given by [21],

$$U/U_{CL} = (1 + (0.644r/r_{1/2})^2)^{-2}. \quad (2)$$

If all of the data from flames A1–A5 are normalized to account for the observed Reynolds number dependence and plotted versus r/x , the results are also found to be consistent with Eqs. 1 and 2. However, in both the present and previous work, only three measurements were obtained at each axial height because of the large time required for data reduction [13]. As a more stringent test of the radial scaling provided by Eqs. 1 and 2, a series of integral time scale measurements were made at 11 or 12 radial locations for axial heights of $x/D = 10, 20, 40,$ and 60 in Flame A3. These measurements are shown in Fig. 7, where the shape of the OH integral time scale versus radial position is clearly not a smooth function, particularly at lower axial heights. The curves in Fig. 7 represent the assumed scaling of Eqs. 1 and 2, where the spread rate ($r_{1/2}/x$) and the centerline integral time scale have been determined by fitting to all of the data for flames A1–A5.

The high-density, time-scale measurements displayed in Fig. 7 reveal several surprising features of the OH fluctuations. Each of the lower height measurements displays a local minimum in τ_I just to the fuel side of the $[\text{OH}]_{\text{max}}$ location and then a maximum very near the $[\text{OH}]_{\text{max}}$ location. It is not presently known whether this a feature of only OH fluctuations or if it also reflects mixture fraction and other scalar fluctuations. Another interesting feature of these curves is the behavior of OH fluctuation rates at large radial locations (on the air side of the $[\text{OH}]_{\text{max}}$ location). Here, the time scales are nearly constant or even begin to decrease ($x/D = 10$), i.e., the OH fluctuations are getting faster for locations farther away from the flame. This result could arise from increased intermittency at these locations, which has been observed to cause faster fluctu-

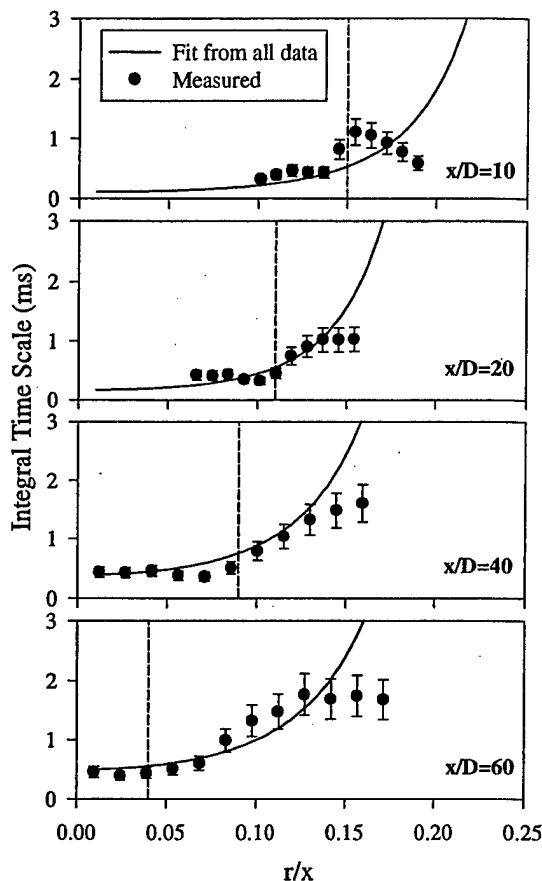


Fig. 7. Measurements of OH integral time scale in flame A3 at various radial locations. The comparison to the assumed form of Eqs. 1 and 2, when fit to all data in flames A1–A5, demonstrates that scaling by the local velocity does not capture the detailed structure in the measurements. The dashed vertical lines show the location of peak $[\text{OH}]$ at each height.

ations [22]. We are presently examining these relationships via improved simulations of our OH time series.

The measurements of Fig. 7 extend over the full range of radial locations for which enough OH signal exists to determine an OH fluctuation time scale. Unfortunately, changes in OH time scales with x/D can not be adequately determined from this data since measurements are not available at the same radial location at each height. This dependency may need to be examined from other scalars (such as temperature). An effective centerline time scale can be extrapolated from the curve fits shown in Fig. 7 for all of the flame data. While no OH exists on

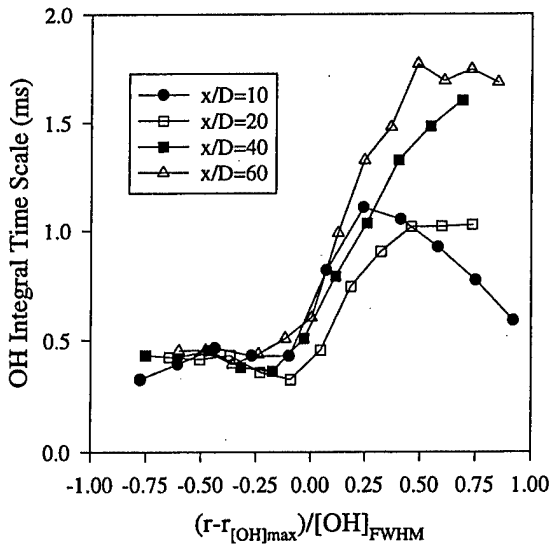


Fig. 8. Measurements of OH integral time scale in flame A3 at various radial locations normalized in the same manner as in Fig. 1.

the centerline at these heights, this extrapolation may indicate the centerline trends expected for other scalars, such as mixture fraction. This procedure suggests a growth rate of $\tau_{I[OH]} \sim (x/D)^{0.9}$, which is in contrast to the expected dependence on $(x/D)^2$ from Eq. 1. However, measurements of other scalars should be used to confirm this result since the curve fits are marginal at low axial heights.

Figure 8 shows the integral time scale measurements from Fig. 7 normalized in the same manner as the time-averaged concentration measurements of Fig. 1. The shapes of the integral time scale profiles are observed to be very similar except for large radial positions. For $(r - r_{[OH]_{max}}) / [OH]_{FWHM} > 0.5$, the mean velocities are very low and this region of the flow may be susceptible to the effects of buoyancy. Only the radial positions for the measurements have been normalized in Fig. 8; hence, the collapse of the time scales on the fuel side of the OH peak at each height indicates that the integral time scale for OH at the location of peak [OH] is constant in these jets. Note that in Fig. 7, the integral time scale appears to increase with rising x/D for a fixed value of r/x , but at each height the flame sits at a different radial location. Because the OH integral time scales are constant at the [OH] peak, the increase in

integral time scale that occurs for larger x/D appears to be almost exactly compensated for by the decrease of the integral time scale that occurs for smaller r/x . In other words, at each axial height, the flame sits at a radial location for which the scalar fluctuation rate is nearly constant (compared to other axial heights).

A similar result was recently reported by Han and Mungal [23] who observed a nearly constant axial velocity (versus x/D) when conditioned on the flame front. If the OH time scales correlate with this constant conditional velocity (instead of the average velocity given by Eq. 1, then the constant integral time scale at the [OH] peaks would imply that the relevant length scales are also constant. In these flames the instantaneous OH layer thickness does not vary much with axial height [7], so this thickness may be a more appropriate scaling parameter for OH than the jet width assumed in Eq. 1. However, this scaling (conditional velocity and OH layer width) does not explain the complicated variation of OH time scale with radial position.

The OH integral time scales in flames D1 and D2 are larger than those in the smaller burner flames. However, the complex shape of the radial profiles for τ_I prohibits a quantitative comparison between these results since it is not clear where, axially or radially, the comparison should be made. The time scales for the 7.8 mm flames are about a factor of 2.5–3.0 times slower than for the 3.4 mm flames at the same x/D and r/x values. The ratio of burner diameters is 2.3 and thus the scaling may simply be $\tau_I \sim D$, but more work is needed to examine this relationship.

However the OH integral time scales are changing with x/D and D , it is clear that the OH fluctuation rates are not simply described by Eq. 1. Measurements of scalar time scales have confirmed that Eq. 1 holds reasonably well in nonreacting jets [17–19,24]. Hence, it appears that the differences we are observing for OH either result from clipping of the OH time series [22] or from the effects of heat release and possibly turbulence/chemistry interactions on the mixture fraction fluctuations themselves.

Probability Density Functions

Although the PDF is not a unique feature of PITLIF measurements, an examination of these

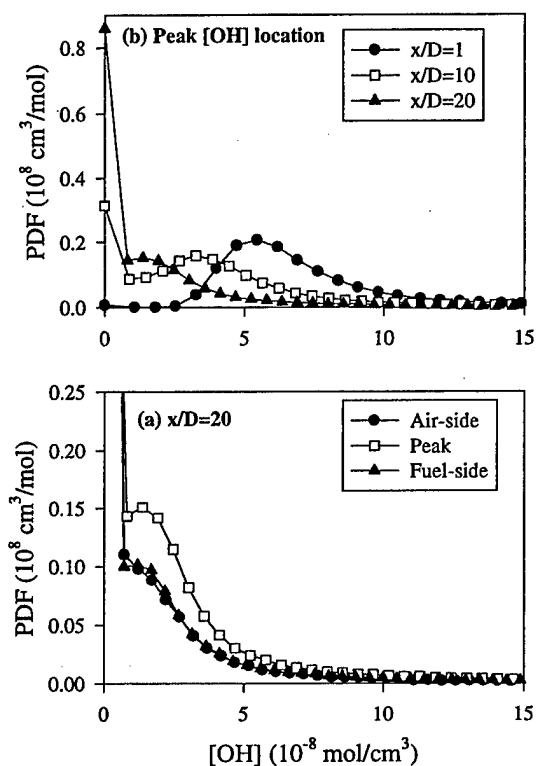


Fig. 9. Probability density functions for flame A3. The PDFs indicate that the maximum instantaneous $[\text{OH}]$ is independent of radial location at a given height (a), but significantly increases in the near-field of the flame where laminarization of the OH layer occurs (b).

statistics can assist in interpreting the time-series data. Figure 9 shows PDFs for flame A3 at the peak $[\text{OH}]$ location for heights of $x/D = 1, 10,$ and 20 , and for three radial locations at $x/D = 20$. Several features of these PDFs are of interest. Note that at $x/D = 20$, the three measured PDFs contain the same range of instantaneous $[\text{OH}]$ values, so that the instantaneous maximum concentration is independent of radial location. However, the measurements from $x/D = 1$ to 20 show considerable changes in the maximum concentration. At low heights, the OH layer is nearly laminarized and lies in a low-velocity region of the flow field. Thus, at these heights, the effects of differential diffusion are likely more important than at downstream locations. Moreover, the slow rate of three-body recombination reactions may cause a peak in the maximum OH concentration at low heights where insufficient residence time

exists for OH equilibrium [1]. The implication is that if the laminar flamelet approximation is invoked to model OH time-series statistics, the state relationship used must depend on axial height.

Since the maximum instantaneous OH concentration does not depend on radial location, a time-averaged OH measurement is simply a convoluted measure of the probability of the flame front intersecting the laser beam. This feature can be quantified by calculating an intermittency parameter from the hydroxyl PDFs. For this purpose, the value of the PDF at $[\text{OH}] = 0$ can be divided by the integral of the PDF over all other concentrations to yield the probability of having no OH at the measurement location. This parameter, I , is not equivalent to the normal definition of intermittency since the probe volume can encompass fully turbulent flow but no measurable OH (as occurs for extinction or fuel-rich mixtures).

These OH intermittency factors are listed in Table 2. Low in the flames, I is close to zero indicating that the PDF is not clipped and OH almost always exists in the probe volume. These regions are characterized by low amplitude fluctuations, which provide further evidence for laminar behavior in this portion of the flow. Moving downstream, the PDFs become increasingly clipped at $[\text{OH}] = 0$. At the same time, the time-averaged OH concentration decreases, the $[\text{OH}]_{\text{rms}}$ increases, and the FWHM of the OH profile rises. Each of these time-averaged parameters are significantly correlated with the intermittency factor, I .

At $x/D = 60$, a measurable OH concentration only exists in the probe volume for about 30% of the time. This suggests that the width of the instantaneous OH profile is narrow (as compared to the mixture fraction fluctuations) even at this large axial height since a broad profile would lead to much smaller values of I . This result is consistent with single-shot PLIF images from a flame similar to D2, as measured by Bergmann et al. [7] at $x/D < 20$. Since the probability of $[\text{OH}] = 0$ is so large, it is likely that the time-series statistics are dominated by the frequency at which the flame crosses the laser beam. In other words, the PSDs and autocorrelation functions may be insensitive to fluctuations in the OH concentration within the

thin flame sheet. If so, the results presented here should be accurately predicted by a laminar flamelet model, even if the peak OH concentration is changing as a function of time.

CONCLUSIONS

Measurements of [OH] time series have been obtained in seven hydrogen/methane/nitrogen nonpremixed jet flames. Time-averaged radial profiles of OH concentration and fluorescence lifetime were obtained over the entire flame length for five Reynolds numbers and two burner diameters. At each axial height, high-repetition-rate time-series measurements were made at three radial locations. These measurements extend over a much broader range of conditions than previously reported for hydrogen/argon flames [6, 10]. The primary conclusions of this study are summarized below.

The time-averaged OH concentrations were found to be nearly Gaussian functions of the radial coordinate. The only parameters necessary to specify the full profile shape are the peak OH concentration, the radial location corresponding to the peak concentration, and the profile FWHM.

The autocorrelation function (or the PSD) collapses to a single function for most measurement locations when normalized by the integral time scale. This result implies that the relative distribution of OH time scales at a single point in the flame is independent of Reynolds number, axial height (above $x/D = 5$), or radial location. The scalar fluctuations are thus accurately characterized by just the integral time scale.

The OH integral time scales are found to increase for (i) decreasing Reynolds number, (ii) increasing axial height, and (iii) increasing radial location. Scaling laws that relate the integral time scale to an eddy turn over time (jet width divided by local mean velocity) can not predict the correct time scale variations in the present flames ($Re < 15,200$). In particular, the OH integral time scale varies as approximately $Re^{-1.4}$ in contrast to the expected Re^{-1} . Likewise, radial profiles of OH time scales are significantly more complex than would be predicted from a smooth velocity profile. The de-

pendence of time scales on axial height is still uncertain since OH measurements can not be made along the jet centerline. Moreover, the prediction of time scales for reactive scalars using nonreactive jet scaling may be inappropriate because of the effects of heat release, the limited range of conditions studied thus far, and the fact that reactive scalars (such as OH) do not completely mimic conserved scalar fluctuations, even under the laminar-flamelet approximation [22].

In the near field of each of the turbulent jets, the autocorrelation functions for OH appear to be nearly laminar owing to the extreme radial locations for the OH layer. The laminarization of the flame in this region is consistent with previous images of the reaction zone in hydrogen flames up to $Re = 50,000$ [16]. Thus, detailed models of turbulent reacting jets may require a separate approach for this region of the flow.

Time-averaged quantities, such as the [OH] mean and rms, appear to be highly correlated to the level of intermittency in the OH time series. Such parameters may only be a measure of the probability with which a fluctuating thin flame sheet intersects the fixed laser beam. Thus, the measured autocorrelation functions and PSDs may only be sensitive to flame-front fluctuations and insensitive to any fluctuations of the OH concentration within the reaction zone.

The present measurements only consider Reynolds numbers below 15,200. While the self similarity of the time-scale statistics implies that the jets are turbulent and not transitional, it is certainly possible that different quantitative or even qualitative results would be obtained at much higher Reynolds numbers. On the other hand, our highest Reynolds number flame is just below the extinction limit for this fuel and is therefore clearly the maximum Reynolds number of interest for this jet diameter and fuel mixture.

This work is supported by the Air Force Office of Scientific Research, with Dr. Julian Tishkoff as technical monitor. We appreciate the ongoing assistance of Professor Jay Gore (Purdue) in many aspects of this study.

REFERENCES

1. Barlow, R. S., Dibble, R. W., Chen, J.-Y., and Lucht, R. P., *Combust. Flame* 82:235 (1990).
2. de Vries, J. E., van der Meer, T. H., and Hoogendoorn, C. J., *Chem. Eng. J.* 53:39 (1993).
3. Chen, Y.-C., and Mansour, M. S., *Proc. Combust. Inst.* 26:97 (1996).
1. McQuay, M. Q., and Cannon, S. M., *Combust. Sci. Technol.* 119:13 (1996).
5. Renfro, M. W., King, G. B., and Laurendeau, N. M., *Combust. Flame*, 122:139 (2000).
6. Renfro, M. W., King, G. B., and Laurendeau, N. M., *Appl. Opt.* 38:4596 (1999).
7. Bergmann, V., Meier, W., Wolff, D., and Stricker, W., *Appl. Phys. B* 66:489 (1998).
8. Meier, W. DLR Stuttgart: Experimental Data Archives. Available at://www.st.dlr.de/EN-CV/flamedat/intro.htm (1999).
9. Lakshmanarao, A., Renfro, M. W., King, G. B., and Laurendeau, N. M., *Exp. Fluids*, in review.
10. Renfro, M. W., Gore, J. P., King, G. B., and Laurendeau, N. M., *AIAA J.* 38:1230 (2000).
11. Seitzman, J. M. (1991). Ph.D. thesis, "Quantitative Applications of Fluorescence Imaging in Combustion," Stanford University, Palo Alto, CA.
12. Pack, S. D., Renfro, M. W., King, G. B., and Laurendeau, N. M., *Combust. Sci. Technol.* 140:405 (1998).
13. Renfro, M. W., Pack, S. D., King, G. B., and Laurendeau, N. M., *Appl. Phys. B* 69:137 (1999).
14. Kee, R. J., Grcar, J. F., Smooke, M. D., and Miller, J. A. (1985). Sandia Report SAND85-8240, Sandia National Laboratory, Livermore, CA.
15. Bowman, C. T., Hanson, R. K., Davidson, D. F., Gardiner, W. C., Jr., Lissianski, V., Smith, G. P., Golden, D. M., Frenklach, M., and Goldenberg, M., GRI-Mech Homepage. Available at://www.me.berkeley.edu/gri-mech/ (1995).
16. Clemens, N. T., and Paul, P. H., *Combust. Flame* 102:271 (1995).
17. Dowling, D. R., and Dimotakis, P. E., *J. Fluid Mech.* 218:109 (1990).
18. Miller, P. L., and Dimotakis, P. E., *J. Fluid Mech.* 308:129 (1996).
19. Dai, Z., Tseng, L. K., and Faeth, G. M., *J. Heat Trans.* 117:138 (1995).
20. Kounalakis, M. E., Sivathanu, Y. R., and Faeth, G. M., *J. Heat Trans.* 113:437 (1991).
21. Schlichting, H., *Boundary-Layer Theory*, McGraw-Hill, New York, 1979, pp. 747-750.
22. Renfro, M. W., Sivathanu, Y. R., Gore, J. P., King, G. B., and Laurendeau, N. M., *Proc. Combust. Inst.* 27:1015 (1998).
23. Han, D., and Mungal, M. G., *Proc. Combust. Inst.*, 28: in press.
24. Lockwood, F. C., and Moneib, H. A., *Combust. Sci. Technol.* 22:63 (1980).

Received 22 December 1999, revised 31 May 2000, accepted 20 June 2000

Self-Similarity of Hydroxyl-Concentration Temporal Statistics in Turbulent Nonpremixed Jet Flames

M. W. Renfro, J. P. Gore, G. B. King,
N. M. Laurendeau

Reprinted from

AIAA Journal

Volume 38, Number 7, Pages 1230-1236



A publication of the
American Institute of Aeronautics and Astronautics, Inc.
1801 Alexander Bell Drive, Suite 500
Reston, VA 20191-4344

Self-Similarity of Hydroxyl-Concentration Temporal Statistics in Turbulent Nonpremixed Jet Flames

Michael W. Renfro,* Jay P. Gore,[†] Galen B. King,[‡] and Normand M. Laurendeau[§]
Purdue University, West Lafayette, Indiana 47907-1288

Temporal statistics for hydroxyl concentrations in turbulent nonpremixed hydrogen/argon flames have recently been reported in the form of power spectral densities for a range of Reynolds numbers (2.8×10^3 – 1.7×10^4) and axial locations ($x/D = 1$ – 20). In the present investigation these data are examined further, and the two-time statistics are shown to collapse when scaled by the measured integral timescale. The resulting autocorrelation function is shown to be closely approximated by an exponential decay, as previously reported for mixture fraction. The measured integral timescales vary with Reynolds number and position within the reacting jet in accordance with a simple similarity scaling. The implications of this unexpected statistical similarity are examined with respect to the simulation of scalar fluctuations in turbulent nonpremixed flames.

Introduction

SELF-SIMILARITY in velocity and scalar cross-stream profiles for nonreacting turbulent jets was established many years ago. These profiles provide a useful representation of mean velocity and scalar fields because, significantly downstream of the jet exit, the cross-stream variations are found to depend only on a single length scale and a single velocity scale. The appropriate scaling parameters, such as the centerline velocity and jet width, display characteristic decay and growth rates that are consistent with fundamental dimensional relationships. The existence of self-similarity for higher-order statistics, such as the variance, has also been observed sufficiently downstream of the jet exit.^{1,2} However, these profiles may still depend on some details of the jet.¹

Time-series measurements of velocity and mixture fraction in nonreacting jets have also displayed self-similar behavior in terms of the power spectral density (PSD) and the autocorrelation function.^{2,3} In particular, these two-time statistics appear to collapse onto a single curve when normalized by a single timescale, such as the integral timescale. However, as the jet Reynolds number increases, the energy bearing and dissipative scales become further separated.⁴ Thus, a single timescale cannot truly be adequate in describing fluctuations at all frequencies, and the observed collapse of two-time statistics when normalizing by the integral time scale is actually limited to fluctuations sufficiently above the Kolmogorov frequency. Alternatively, a second parameter, such as another timescale or the Reynolds number, can be used to collapse the full spectrum.⁵

The existence of self-similarity for scalars in reacting flows is less clear owing both to the effects of source terms and to the interaction between heat release and turbulence. Kounalakis et al.⁶ found self-similar autocorrelation functions for mixture fraction and path-integrated radiation in hydrogen jet flames, but their results should not hold for the mean concentration profiles of those reacting scalars that depend strongly on detailed chemical kinetics. For example, hydroxyl concentrations in turbulent jet flames achieve maximum values several times larger than those predicted by chemical equilibrium low in the flames and decay with increasing height owing to the relatively slow three-body recombination reactions responsible for OH destruction.⁷ For this case the change in OH concentration through the jet represents much more than a simple mixing process. On the other hand, some reactive scalars, including OH,

display strong correlations with the local mixture fraction despite their departure from a simple laminar flamelet description.⁷ Thus, at a given location, instantaneous OH fluctuations may exhibit a strong dependence on the instantaneous mixture fraction fluctuations.

In the present investigation recently compiled OH data are examined for self-similarity with respect to relevant two-time statistics. The time-series measurements of OH concentrations were made by Renfro et al.⁸ via a gated-photon counting technique, termed picosecond time-resolved laser-induced fluorescence (PITLIF). All data were obtained in a 78% H₂/22% Ar (by volume) turbulent jet flame in still air. The flame was stabilized on a straight tube burner with an exit diameter of 5.5 mm with no coflow. The laser and detection system provided a spatial resolution of less than 100 μm in all three directions. Time-series measurements of OH were made at 3–5 radial locations across the OH peak at axial locations of $x/D = 1, 2, 5, 10,$ and 20 for Reynolds numbers of $Re = 2.8 \times 10^3, 5 \times 10^3, 9 \times 10^3, 1.3 \times 10^4,$ and 1.7×10^4 , based on the cold-flow average velocity at the jet exit.

Nearly identical flames have been studied experimentally by several other groups.^{7,9–11} For example, simultaneous OH concentration and mixture fraction measurements were reported for the same fuel (5.2-mm burner) by Barlow et al.⁷ at Reynolds numbers of 8.5×10^3 and 1.7×10^4 . These single-shot measurements permitted determination of probability density functions (PDFs). Employing the same fuel, Chen and Mansour¹¹ obtained simultaneous, multipoint OH concentration and mixture fraction measurements, thus allowing examination of radial scalar dissipation rates in a 4.8-mm jet at Reynolds numbers of 8.8×10^3 and 1.76×10^4 . Many experiments in other hydrogen jet flames have also examined hydroxyl concentrations. However, the measurements of Renfro et al.⁸ provide the only data that permit investigation of timescales for hydroxyl concentration fluctuations.

In the following section a suitable correction is derived to account for the effects of shot noise in PITLIF measurements of the autocorrelation function. From the resulting quantitative correlations the hydroxyl integral timescales are computed. Normalization using these scales is shown to collapse the measured temporal correlations for OH throughout each of the flames studied. This result implies that a single timescale is sufficient to describe the measured OH fluctuations, which is unexpected for reactive scalars owing to the uncertain impact of those scalar fluctuations related to chemical production and destruction. Finally, the evolution of the measured OH integral timescales is examined for the present reacting jets and compared to predictions of timescales for mixture fraction fluctuations in both reacting and nonreacting jets.

Data Reduction

Significant complications arise when attempting time-series measurements of minor-species concentrations. The details concerning

Received 15 May 1999; revision received 29 September 1999; accepted for publication 11 October 1999. Copyright © 2000 by the American Institute of Aeronautics and Astronautics, Inc. All rights reserved.

*Research Assistant, School of Mechanical Engineering.

[†]Professor, School of Mechanical Engineering. Member AIAA.

[‡]Associate Professor, School of Mechanical Engineering.

[§]Reilly Professor of Combustion Engineering, School of Mechanical Engineering.

the measurement technique and the procedures by which it is made quantitative are fully discussed by Renfro et al.⁸ At each measurement location in the flames investigated, 50 separate time series of 4000 samples were taken at a sampling rate of 4000 Hz. Renfro et al.⁸ present PSDs and PDFs computed from these time series. In addition to these statistics, the present investigation makes use of the autocorrelation function.

The autocorrelation function ρ and the PSD are formally defined by¹²

$$\rho_m(\Delta t) = \frac{\overline{[\text{OH}]'(t)[\text{OH}]'(t + \Delta t)}}{([\text{OH}]'_{\text{rms}})^2} \quad (1)$$

$$\text{PSD}_m(f) = \frac{|\mathfrak{F}\{[\text{OH}]'(t)\}|^2}{([\text{OH}]'_{\text{rms}})^2} = \mathfrak{F}\{\rho_m(\Delta t)\} \quad (2)$$

where $[\text{OH}]' = [\text{OH}] - \overline{[\text{OH}]}$ is the fluctuating part of the time series $[\text{OH}]'_{\text{rms}} = \sqrt{\overline{[\text{OH}]'^2}}$ and \mathfrak{F} represents a Fourier transform. Both Eqs. (1) and (2) are strictly defined for an infinite amount of continuous data. Because the measured OH time series represents a finite amount of discrete data, a working definition for the autocorrelation function must be used, i.e.,¹²

$$\rho_m(\Delta t_i) = \frac{\sum_{j=0}^{N-i} [\text{OH}]'_j [\text{OH}]'_{j+i}}{\sum_{j=0}^N ([\text{OH}]'_j)^2} \quad (3)$$

where the discrete time series of N hydroxyl concentration measurements is represented by $[\text{OH}]_j$ for the j th sample time t_j .

The subscript m in Eqs. (1–3) indicates that these are computed directly from the measurements. However, in our measured time series, signal fluctuations occur from both real hydroxyl concentration fluctuations and from shot noise in the photon counting system. The autocorrelation function is affected by both fluctuation sources. Fortunately, Gaskey et al.¹³ have found that, because shot-noise fluctuations are uncorrelated with concentration fluctuations, any measured power spectrum is a weighted sum of the contributions from both fluctuation sources considered separately. Furthermore, the shot-noise fluctuations are uncorrelated with themselves so that the shot-noise PSD is uniform over all frequencies. Thus, a shot-noise corrected PSD can be computed from the measured PSD by⁸

$$\text{PSD}_{\text{OH}}(f) = \frac{\text{PSD}_m(f) - C^2/f_c}{1 - C^2} \quad (4)$$

where $C = \sigma_{\text{SN}}/\sigma$ is the shot-noise fluctuation intensity normalized by the total fluctuation intensity (rms) and f_c is the high-frequency cutoff in the PSD, which is equal to half the sampling rate. The fraction C can be found by averaging the PSD at high frequencies where shot noise is dominant.⁸ The preceding PSD correction was found to work well for the present OH measurements by Renfro et al.⁸ Because the autocorrelation function is the inverse Fourier transform of the PSD, the shot-noise corrected autocorrelation function becomes

$$\begin{aligned} \rho_{[\text{OH}]}(\Delta t_i) &= \frac{\mathfrak{F}^{-1}\{\text{PSD}_m(f)\}}{1 - C^2} - \frac{C^2}{(1 - C^2)} \mathfrak{F}^{-1}\left\{\frac{1}{f_c}\right\} \\ &= \frac{\rho_m(\Delta t_i)}{1 - C^2} - \frac{C^2}{1 - C^2} \delta_{\Delta t_i, 0} \end{aligned} \quad (5)$$

Equation (5) shows that the autocorrelation function for the shot-noise contribution is a delta function at zero. This feature is expected because shot noise is uncorrelated for all nonzero time delays. The factor f_c in the second Fourier transform is a result of the data being discrete, i.e., the delta function is finite in width.

Figure 1a shows the autocorrelation functions for OH fluorescence and concentration as measured in the $Re = 9 \times 10^3$ flame at $x/D = 20$, 2 mm to the fuel side of the maximum [OH]. As determined from the PSDs, the shot-noise factor is $C = 0.30$ for the fluorescence measurement and $C = 0.81$ for the concentration measurement at this location. As discussed by Renfro et al.,⁸ the effects of shot noise are worse for concentration, which must be corrected for fluorescence lifetime variations, as compared to the fluorescence

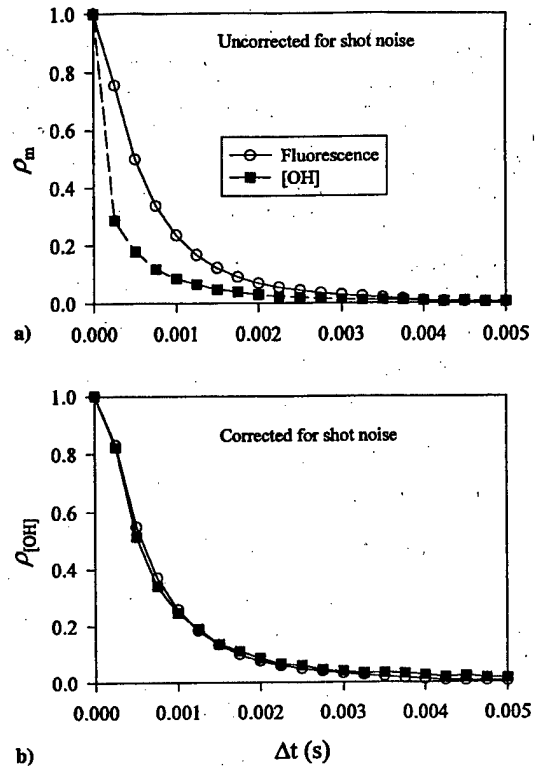


Fig. 1 Hydroxyl concentration and fluorescence autocorrelation functions measured 2 mm to the fuel side of the [OH] peak at $x/D = 20$ in the $Re = 9 \times 10^3$ flame. The shot-noise corrected autocorrelation functions ($\rho_{[\text{OH}]}$) are computed from the measured functions (ρ_m) via Eq. (5).

signal, which is directly measured. The uncorrected concentration correlation (ρ_m) drops off much faster than that for fluorescence owing to the shot-noise delta function at zero. Without correcting for shot noise, the correlation functions for concentration and fluorescence differ. In comparison, Fig. 1b shows the autocorrelation functions for concentration and fluorescence after correction for shot noise ($\rho_{[\text{OH}]}$). These are nearly identical, consistent with the PSDs already reported.

The accuracy of the noise correction is affected by both the measurement of C^2 and the signal-to-noise ratio. For each of the measurements reported here, C^2 is determined with an uncertainty of only $\pm 4\%$ (95% confidence interval)⁸ owing to the large amount of data (50 independent series) collected at each location. The signal-to-noise ratio (SNR) for both the PSD and autocorrelation function is simply the ratio of the intensity of fluctuations arising from concentration to those arising from shot noise. From rearrangement of Eq. (4), the SNR is found to be equal to $1/C^2 - 1$. For each of the present measurements, the SNR is always greater than 3 and is often as large as 20.

In the next section the integral timescale τ_I for these measurements is examined. The integral timescale represents approximately the largest time over which fluctuations are correlated and is defined by

$$\tau_I = \int_0^{\infty} \rho_{[\text{OH}]}(\Delta t) d\Delta t \quad (6)$$

As for the autocorrelation function, Eq. (6) is defined for an infinite and continuous time record; thus, τ_I can only be estimated from the discrete autocorrelation function by using a numerical integration. However, for the relatively long time series considered here, the discrete representation for τ_I is close to that defined in Eq. (6).¹² Without correcting for shot noise, the measured integral timescales will be systematically reduced by a factor of roughly $1 - C^2$. The impact of this correction can be observed by comparing Figs. 1a and 1b for which the areas under the concentration autocorrelation functions are notably different. Hence, the preceding shot-noise correction has been applied to each of the statistics reported in the remainder of this paper.

Renfro et al.⁸ have also used this shot-noise correction to determine relative [OH] rms values with an uncertainty of $\pm 10\%$ (95% confidence interval). The relative [OH]_{rms} values are normalized by the mean [OH] values, which have a $\pm 18.5\%$ uncertainty (95% confidence interval) arising from the fluorescence calibration procedure.⁸ We have further examined the accuracy of this noise correction by repeating the integral timescale measurements nine times over seven days, each with a different level of noise. The uncertainty in the integral timescale was found to be $\pm 22.2\%$ (95% confidence interval).

Results

Figure 2a shows the autocorrelation function for each flame at the radial location of peak [OH] for $x/D = 5, 10,$ and 20 . The exact location for each of these measurements is tabulated by Renfro et al.⁸ The integral timescale decreases significantly with increasing Reynolds number. As a result, the autocorrelation functions show significant variations in width. However, Fig. 2b shows the same data normalized by the measured integral timescale. The normalized autocorrelation function is the same for each measurement, independent of the Reynolds number and axial height. The autocorrelation functions for $x/D < 20$ in the $Re = 2.8 \times 10^3$ flame are not shown in Fig. 2. At these locations significant periodic fluctuations are present, similar to those reported previously in the near field of diffusion flames.¹⁴ These fluctuations manifest themselves as a strong frequency in the PSD⁸ and equivalently as a sinusoid in the autocorrelation trace. These PSDs do not collapse with the others, but this behavior is, of course, not unexpected as the statistics for large-scale oscillations are not represented by a purely turbulent autocorrelation function.

When autocorrelation functions for $x/D = 1$ and 2 are considered in addition to those in Fig. 2, the collapse is still observed, but significantly more scatter is present. For example, Fig. 3a shows OH concentration autocorrelation functions for three radial locations at each axial height in the $Re = 9 \times 10^3$ flame. Near the burner exit the autocorrelation functions show considerable correlation for large time delays (large-scale, low-frequency fluctuations). Nevertheless, for small time delays (small-scale, high-frequency fluctuations), the

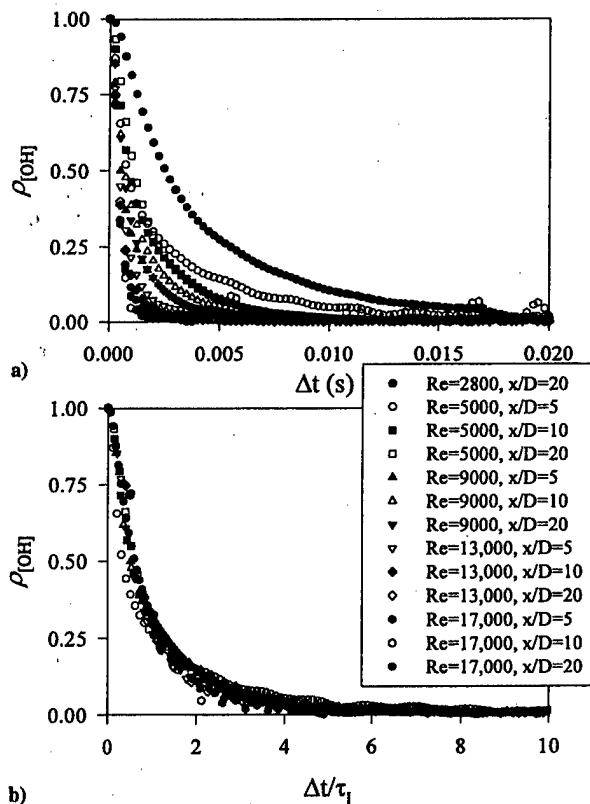


Fig. 2 Autocorrelation functions for [OH] at the radial location of peak OH concentration in each flame.

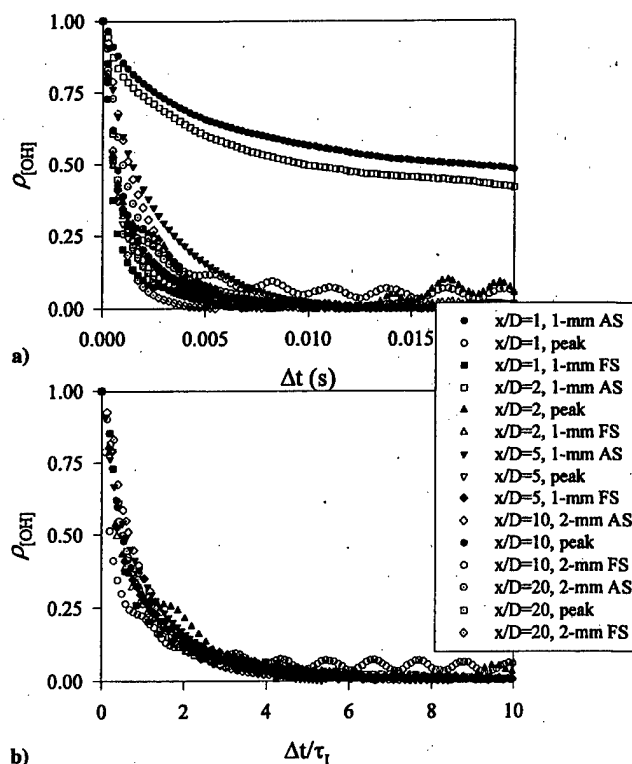


Fig. 3 Autocorrelation functions for [OH] in the $Re = 9 \times 10^3$ flame. Measurements are reported for the radial location of peak [OH] and for locations relative to the peak on both the air side (AS) and the fuel side (FS).

autocorrelation functions for $x/D = 1$ and 2 are quite close to those for the downstream locations. However, the measurements toward the air side of the peak concentrations at $x/D = 1$ and 2 show integral timescales significantly larger than any of the other measurements. At these low heights the hydroxyl peaks are located outside of the turbulent flow and may undergo significant laminarization.^{15,16} Hence, these autocorrelation functions are more representative of a laminar flow for which all time delays are perfectly correlated. Figure 3b shows the scaled autocorrelation functions. The two near-laminar measurement locations are not shown in Fig. 3b as they do not collapse with the remaining measurements. It may be possible to account for laminar flow effects by including an intermittency parameter, but this is beyond the scope of the present investigation.

The scatter in the normalized autocorrelation functions in Fig. 3b is worse than that in Fig. 2b. Several measurement locations (e.g., the peak [OH] location at $x/D = 1$ and 2) display a noticeable sinusoidal fluctuation in the autocorrelation function. This is indicative of a single-frequency oscillation, as with buoyancy; however, these fluctuations are at ~ 360 Hz, which is far too large to be a buoyancy-induced oscillation.¹⁷ The PSDs from these locations also show a strong component at ~ 360 Hz (e.g., Renfro et al.,⁸ Fig. 7); however, the width of this peak in the PSD is very narrow so that the intensity of the [OH] fluctuations resulting from this oscillation is quite small. Hence, this feature is likely either a noise artifact or a large-scale periodic fluctuation,¹⁴ which is apparent at these locations because of the reduced [OH] fluctuations. Away from the peak concentration and further downstream, the OH concentration fluctuations are several times larger than those at the peak concentration at $x/D = 1$ and 2 (Ref. 8), such that this small artifact is no longer visible.

An autocorrelation function can be computed free of the 360-Hz oscillation by taking the inverse Fourier transform of the PSD with the value at 360 Hz set equal to the average of that at 359 and 361 Hz. For the measurements at $x/D = 1$, this procedure still does not cause the autocorrelation functions to collapse as $\rho_{[OH]}$ is significantly above zero for large time delays. Thus, the larger scatter observed for the normalized autocorrelation functions of Fig. 3b appears to be a result of both small single-frequency components and the location of the OH layer in a laminar regime at these heights.¹⁶ Figure 4 shows the same autocorrelation functions as Fig. 3 except

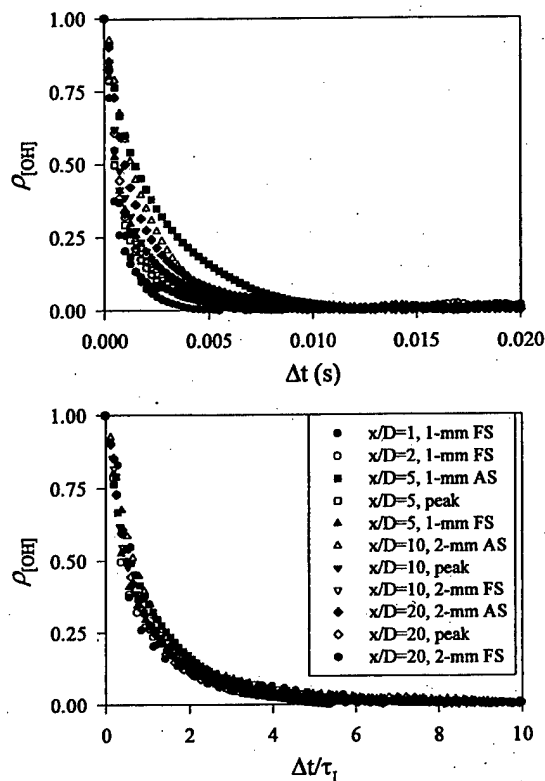


Fig. 4 Same data as Fig. 3 without air side and peak measurements at $x/D = 1$ and 2.

with the air side and peak data removed at $x/D = 1$ and 2. The collapse of all remaining measurements is observed to be equivalent to that in Fig. 2. Hence, the autocorrelation function shape is independent of Reynolds number, axial height, and radial location in these jet flames for all locations except those very low in the flames where the OH profile resides outside of the turbulent flow. This result is remarkable because the Damköhler number varies by two orders of magnitude over the conditions $x/D = 5$ –20 and $Re = 2.8 \times 10^3$ – 1.7×10^4 (Ref. 7). Thus, whereas the relative timescale for chemical reactions changes significantly, the normalized autocorrelation function remains the same.

Because the PSD and autocorrelation function are Fourier transform pairs, a similar collapse of the measured PSDs is expected when scaled by the integral timescale. This collapse is shown in Fig. 5 for measurements at the [OH] peak for $x/D = 20$ in each flame. The same integral timescales as computed from Fig. 2 are effective in collapsing the PSDs. Because each measurement was taken at a sampling rate of 4 kHz, the highest dimensional frequency resolved in the PSDs is 2 kHz. However, the integral timescale decreases as the Reynolds number rises such that the measurements in the higher-Reynolds-number flames resolve lower nondimensional frequencies.

The increased frequency of the OH fluctuations at higher Reynolds numbers can also be shown directly from the measured time series. Figure 6 displays 0.1 s of OH data from the $Re = 2.8 \times 10^3$, 9×10^3 , and 1.7×10^4 measurements used to compile Fig. 5. These time series were selected randomly and are typical of the full 50 s of data collected at each location. Each of these time series has been normalized by the appropriate mean [OH] values, which are tabulated by Renfro et al.⁸ All three time series in Fig. 6 display a similar behavior about the mean despite the large change in fluctuation timescales.

Because the frequencies of the OH fluctuations increase at higher Reynolds numbers, the sampling rate should obviously be increased as the Reynolds number rises. Unfortunately, this is only possible up to the point at which shot-noise fluctuations become dominant. For each of the measurements reported here, the PSD begins to flatten at high frequencies as a result of shot noise (e.g., Renfro et al.,⁸ Fig. 3). It is unlikely that higher frequencies can be directly

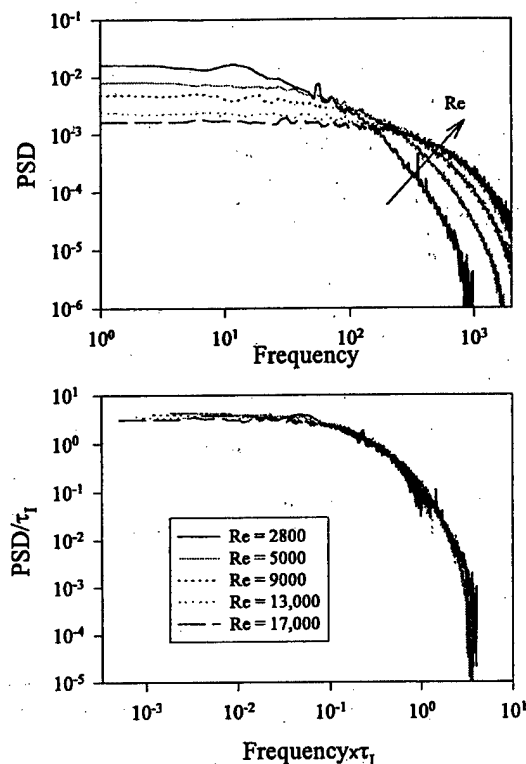


Fig. 5 Power spectral densities measured at the location of peak [OH] at $x/D = 20$ in each flame. Integral timescales used to normalized the PSDs were computed from the autocorrelation functions of Fig. 2.

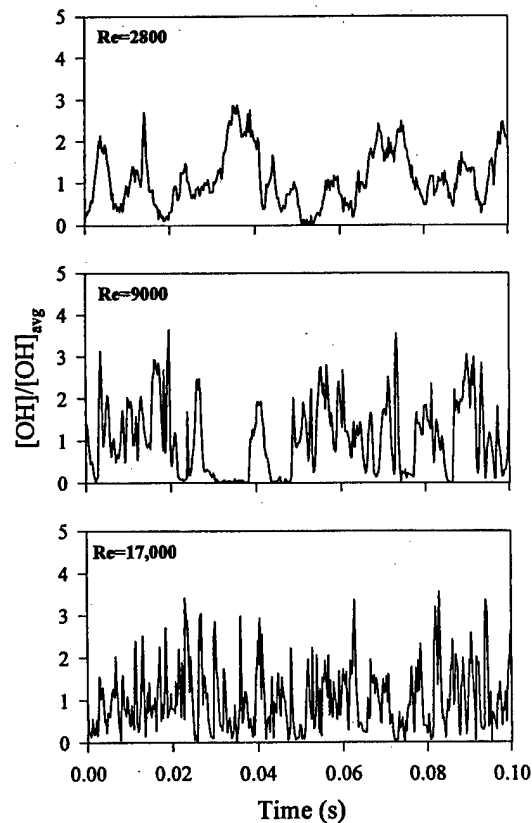


Fig. 6 Sample time series measured at the peak [OH] location for $x/D = 20$ in the $Re = 2.8 \times 10^3$, 9×10^3 , and 1.7×10^4 flames. These time series represent the first 0.1 s of measurements used to compile Fig. 5. These time series were selected randomly and are typical of the full 50 s of data collected at each location and are representative of the full 50 s.

resolved in these flames without a significant increase in signal, say by improved laser technology or by reduced spatial resolution. On the other hand, the good collapse of the measured autocorrelation functions and PSDs in these flames suggest that the measurements at lower Reynolds numbers can be extended to the flames at higher Reynolds numbers. In other words, because the dimensionless $Re = 1.7 \times 10^4$ PSD matches that at lower Reynolds numbers up to a frequency of $\sim 1/\tau_I$, the low-Reynolds-number PSD could be assumed to be valid up to higher frequencies, effectively increasing the temporal resolution of the $Re = 1.7 \times 10^4$ PSD. However, this approach can cause problems because use of the integral timescale for collapse of the PSDs does not consider the separation between τ_I and the Kolmogorov timescale (or Batchelor timescale for scalars) as a function of Reynolds number.⁴ In other words, the normalized spectrum that appears to describe adequately each of the PSDs of Fig. 5 is valid only up to timescales for which dissipation becomes significant, and this will occur at different normalized frequencies for each Reynolds number.⁵

In summary, each measured OH time series for $x/D = 5-20$ and $Re = 2.8 \times 10^3 - 1.7 \times 10^4$ is observed to collapse onto the same normalized autocorrelation function, or equivalently PSD, at least up to the frequencies resolved by these measurements. These nondimensional curves are shown in Fig. 7a for the autocorrelation function and Fig. 7b for the PSD. Also shown for comparison is an exponential autocorrelation function and its power spectral density. Mixture fraction fluctuations in both nonreacting jets³ and jet diffusion flames⁶ have been found to be closely approximated by an exponential autocorrelation function. The agreement here is very similar to that noted by Kounalakis et al.⁶ for mixture-fraction measurements in turbulent CO/H₂ flames. In particular, the exponential function is adequate for low frequencies (large time delays) and captures the general shape of the PSD. However, the exponential autocorrelation function does not capture the correct curvature near $\Delta t = 0$, where the first derivative should be zero because the autocorrelation function is even and infinitely differentiable.⁴ Thus, for very small time delays the exponential decays too quickly as compared to the measured [OH] correlation. At intermediate time delays ($0.5\tau_I < \Delta t < 2.0\tau_I$) all of the measured data are less correlated than predicted by an exponential decay. Both of these observations

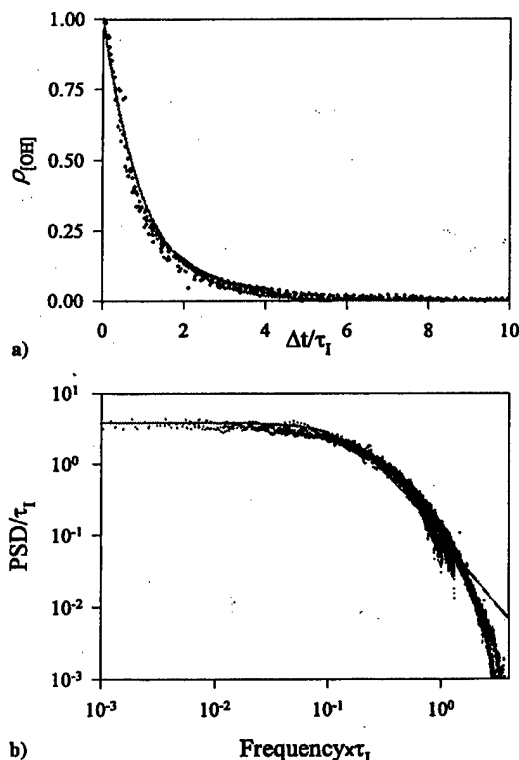


Fig. 7 Comparison of collapsed statistics with those of an exponential autocorrelation function. The individual data points represent each of the measurements from Figs. 2, 4, and 5.

are consistent with the mixture fraction correlations of Kounalakis et al.⁶

For the PSD the measured data decay with a much steeper slope than that predicted by the exponential autocorrelation function at large frequencies. On the other hand, the data available for $f > 1/\tau_I$ are limited to the two lowest Reynolds-number flames. This steepening of the power spectra could be a result of the effects of dissipation near the Batchelor scale. As just mentioned, use of the integral timescale for collapse of the PSDs should not extend to the dissipation range of the spectra.

Having demonstrated the effectiveness of the integral timescale in collapsing the measured autocorrelation functions and PSDs at low to moderate frequencies, we now examine the evolution of τ_I as a function of Re , x , and r in these flames. The integral timescale is proportional to some relevant length scale divided by some relevant velocity scale. Taking the local velocity and jet width as the appropriate scales, the velocity integral timescale would be expected to follow

$$\begin{aligned} \tau_I &\sim \frac{L}{U(x, r)} \sim \left(\frac{1}{U_e}\right) \left(\frac{LU_e}{U_{cl}(x)}\right) \left(\frac{U_{cl}(x)}{U(x, r)}\right) \\ &\sim \left(\frac{1}{Re}\right) \left(\frac{x}{D}\right)^2 f\left(\frac{r}{x}\right) \end{aligned} \quad (7)$$

where L is the integral length scale, which grows linearly with axial distance,⁴ $U(x, r)$ is the local velocity, U_e is the average velocity at the burner exit ($\sim Re$), $U_{cl}(x)$ is the centerline velocity ($\sim U_e/x$), and $f(r/x)$ is some function of the normalized radial coordinate. This scaling procedure is also discussed by Magre and Dibble.¹⁰ For nonreacting jets, where the mixture fraction develops similar to velocity, the integral timescale for mixture fraction should also scale as in Eq. (7). This scaling has indeed been observed.^{3, 18} Figure 8 shows τ_I for OH fluctuations at $x/D = 20$ in each flame (as a function of only Reynolds number). Somewhat surprisingly, the hydroxyl timescales have the same linear dependence on $1/Re$ as the velocity and mixture fraction timescales.

Unfortunately, the OH profile does not reside at the same radial location (r/x) at all axial heights, particularly low in these flames.⁸ Thus, the axial scaling of Eq. (7) cannot be simply separated from any radial dependence of τ_I as reflected by $f(r/x)$. Figure 9 shows all of the integral timescales of this study scaled for Reynolds number and axial location (assuming $\tau_I \sim x^2$) as a function of relative radial location (r/x). The collapse of τ_I to nearly a single curve indicates that the assumed axial scaling is reasonably valid. On the other hand, there is over a four order-of-magnitude variation in these normalized timescales, and the comparison in log coordinates does not provide a sensitive measure of the exact axial variation, i.e., an assumed dependence of $x^{1.75}$ to $x^{2.25}$ would visually look just as good.

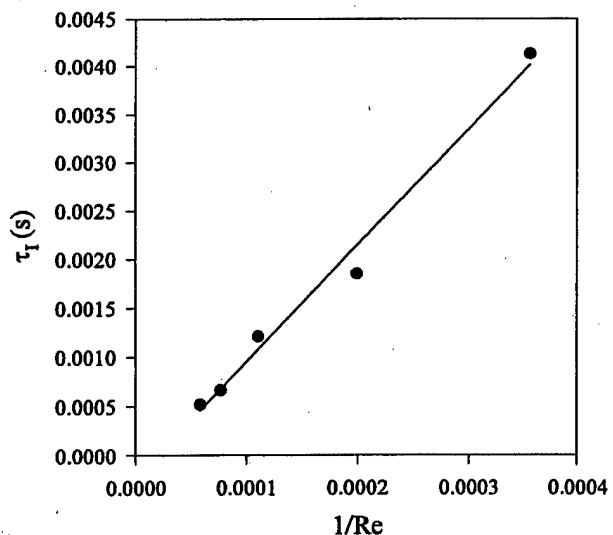


Fig. 8 Integral timescales computed from the autocorrelation functions of Fig. 2 for the locations of peak [OH] at $x/D = 20$ in each flame.

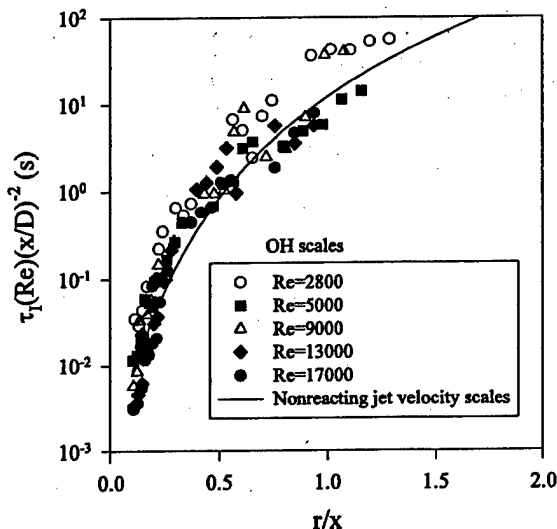


Fig. 9 Normalized integral timescale computed for every time series of the present flames. The expected integral timescales based on the nonreacting-jet velocity correlation of Schlichting¹⁹ are also shown.

Similarly, Kounalakis et al.⁶ find that their mixture-fraction integral timescales collapse when normalized by only x . These authors provide data for only a few axial locations (as with our measurements) and use a virtual origin in their normalization such that the sensitivity of the collapse to the exponent of x^n is also weak. For nonreacting jets a scaling of x^2 for mixture fraction appears to be correct,^{3,18} but improved measurements of mixture fraction in reacting jets are needed to resolve this scaling issue in turbulent flames.

Figure 9 also shows a comparison of the measured timescales with those predicted based on a self-similar radial profile for velocity in nonreacting jets.¹⁹ Once again, the OH timescales appear to reasonably follow temporal statistics that are similar to those for velocity in nonreacting jets.

Discussion

The self-similarity of OH PSDs for flames with Reynolds numbers as low as 2.8×10^3 is somewhat surprising in view of previous work.^{15,16} Seitzman et al.¹⁵ measured OH spatial distributions in hydrogen jet flames at $x/D = 2.5-40$ and found that OH exists in a nearly laminar layer at $Re = 2.3 \times 10^3$. Likewise, Clemens and Paul¹⁶ measured the OH structure in the near field ($x/D < 2.5$) of hydrogen/nitrogen flames and found completely laminarized thin OH layers that were not perturbed by the fuel-stream turbulence. However, in pure hydrogen flames, Clemens and Paul¹⁶ found that the OH distribution was thin below $x/D = 2.5$ but slightly perturbed by the fuel stream as a result of the lower fuel density. At higher Reynolds numbers and further downstream ($x/D = 2.5-40$), Seitzman et al.¹⁵ showed that the structure of the OH distribution changes from thin filaments to both thin and diffuse distributions. However, these higher-Reynolds-number flames were lifted, and it is likely that their OH structure is inherently different than for attached flames. For all of our hydrogen/argon flames, with a fuel density between the hydrogen and hydrogen/nitrogen cases of Clemens and Paul,¹⁶ it is likely that OH exists in only a thin region.

The discrepancy that we see in our autocorrelation functions at $x/D < 5$ is probably a result of the laminarized near-field behavior of these turbulent diffusion flames.¹⁶ Nevertheless, farther downstream, the perturbations of the thin OH layer caused by fuel-stream turbulence are apparently sufficient to be measured by the time-series technique and to yield a turbulence spectrum. At $Re = 70$ the PITLIF technique gives flat PSDs²⁰ arising from purely laminar flows. Hence, the unexpected collapse of the $Re = 2.8 \times 10^3$ case at $x/D = 20$ is not a measurement artifact, but is most likely a result of thin OH flamelets that exist over the entire range from $Re = 2.8 \times 10^3$ to 1.7×10^4 . An additional complication is that our flames are significantly affected by buoyancy,²¹ which can increase the momentum flux at downstream locations for lower Reynolds

numbers and may thus contribute to the collapse of the time-series statistics. Thus, the interpretation of our results is presently limited to moderate Reynolds numbers. Whether the observed self-similarity will hold for higher-Reynolds-number flames and for higher frequencies than those resolved in the present experiments are interesting questions for future work.

Nevertheless, for the range $Re = 2.8 \times 10^3-1.7 \times 10^4$, which is common to many laboratory experiments and practical flows, the self-similarity of OH temporal statistics at sufficiently high x/D is certainly intriguing. Transient models of turbulent combustion can be evaluated effectively based on their ability to predict such results. In addition, the measured hydroxyl fluctuations are found to follow approximately an exponential autocorrelation function. However, the present measurements were limited to a sampling frequency of 4 kHz. For larger frequencies for which dissipation is significant, the autocorrelation functions should not collapse when scaled by the integral timescale.

Because local OH fluctuations in these flames appear to follow the same temporal statistics as local mixture fraction fluctuations, a simple one-dimensional laminar flamelet approach to modeling of OH PSDs may yield good agreement with measurements.²² On the other hand, peak OH concentrations as a function of axial height in similar flames have been shown to depend strongly on the Damköhler number owing to the existence of superequilibrium OH concentrations,⁷ which also affects the flame temperature.¹⁰ Thus, matching the measured variation in peak OH concentration via flamelet modeling may require different state relationships for each height (or perhaps two-dimensional state relationships).

This apparent discrepancy arises because the collapse of the temporal statistics does not require a collapse of the associated PDFs, which display various shapes in different regions of the present flames.⁸ Renfro et al.²² simulated minor-species PSDs for these flames using laminar flamelet state relationships and found that the simulations were sensitive to the mixture fraction statistics and concentration profile width, but were fairly insensitive to the exact profile shape and peak concentration. In contrast, the PDF depends strongly on the profile shape and the peak concentration. PDFs and PSDs describe separate information about the scalar fluctuations. Although these statistics are computed from the same time series, it appears that they are nearly independent of one another. We are presently investigating means of incorporating realistic PDF and PSD behavior into mixture fraction time-series simulations so that critical comparisons can be made between predictions of different combustion models, including the laminar flamelet model.

Conclusions

Recent hydroxyl time-series measurements obtained by Renfro et al.⁸ have been examined for statistical similarity with respect to autocorrelation functions and PSDs. By normalizing these two-time statistics by the measured OH integral timescale, a single normalized autocorrelation function (and PSD) was found to describe all of the data in the investigated flames for $Re = 2.8 \times 10^3-1.7 \times 10^4$ and $x/D = 5-20$. The collapse of the measured statistics for measurements at $x/D = 1$ and 2 is worse than for measurements further downstream. At these lower heights, measurements made toward the ambient air side were found to display large variations, most probably as a result of the nearly laminar flow in these regions.

The observed collapse of the autocorrelation functions demonstrates that hydroxyl fluctuations are adequately described by a single timescale and thus a single normalized autocorrelation function. This is not an expected result for reactive scalars because both turbulent mixing and chemical reaction can affect [OH] fluctuations, and the timescales for these two processes are not the same. Moreover, multiple chemical timescales exist for species such as OH so that Damköhler numbers both greater than and less than unity are present in these flames.⁷

Acknowledgments

This research was supported by the U.S. Air Force Office of Scientific Research, with Julian Tishkoff serving as technical monitor, and by a Department of Defense fellowship. We appreciate the very helpful comments made by one reviewer of the original manuscript.

References

- ¹Hussein, J. H., Capp, S. P., and George, W. K., "Velocity Measurements in a High-Reynolds-Number, Momentum-Conserving, Axisymmetric, Turbulent Jet," *Journal of Fluid Mechanics*, Vol. 258, 1994, pp. 31-75.
- ²Wyganski, I., and Fiedler, H., "Some Measurements in the Self-Preserving Jet," *Journal of Fluid Mechanics*, Vol. 38, Pt. 3, 1969, pp. 577-612.
- ³Birch, A. D., Brown, D. R., Dodson, M. G., and Thomas, J. R., "The Turbulent Concentration Field of a Methane Jet," *Journal of Fluid Mechanics*, Vol. 88, Pt. 3, 1978, pp. 431-449.
- ⁴Tennekes, H., and Lumley, J. L., *A First Course in Turbulence*, MIT Press, Cambridge, MA, 1972.
- ⁵Uberoi, M. S., and Freymuth, P., "Spectra of Turbulence in Wakes Behind Circular Cylinders," *Physics of Fluids*, Vol. 12, No. 7, 1969, pp. 1359-1363.
- ⁶Kounalakis, M. E., Sivathanu, Y. R., and Faeth, G. M., "Infrared Radiation Statistics of Nonluminous Turbulent Diffusion Flames," *Journal of Heat Transfer*, Vol. 113, May 1991, pp. 437-445.
- ⁷Barlow, R. S., Dibble, R. W., Chen, J.-Y., and Lucht, R. P., "Effect of Damköhler Number on Superequilibrium OH Concentration in Turbulent Nonpremixed Jet Flames," *Combustion and Flame*, Vol. 82, 1990, pp. 235-251.
- ⁸Renfro, M. W., King, G. B., and Laurendeau, N. M., "Quantitative Hydroxyl-Concentration Time-Series Measurements in Turbulent Nonpremixed Flames," *Applied Optics*, Vol. 38, No. 21, 1999, pp. 4596-4608.
- ⁹Driscoll, J. F., Schefer, R. W., and Dibble, R. W., "Mass Fluxes $\overline{\rho'u}$ and $\overline{\rho'v}$ Measured in a Turbulent Nonpremixed Flame," *Nineteenth Symposium (International) on Combustion*, Combustion Inst., Pittsburgh, PA, 1982, pp. 477-485.
- ¹⁰Magre, P., and Dibble, R., "Finite Chemical Kinetics Effects in a Subsonic Turbulent Hydrogen Flame," *Combustion and Flame*, Vol. 73, 1988, pp. 195-206.
- ¹¹Chen, Y.-C., and Mansour, M. S., "Measurements of the Detailed Flame Structure in Turbulent H₂-Ar Jet Diffusion Flames with Line-Raman/Rayleigh/LIPF-OH Technique," *Twenty-Sixth Symposium (International) on Combustion*, Combustion Inst., Pittsburgh, PA, 1996, pp. 97-103.
- ¹²Box, G. E. P., Jenkins, G. M., and Reinsel, G. C., *Time Series Analysis*, 3rd ed., Prentice-Hall, Upper Saddle River, NJ, 1994.
- ¹³Gaskey, S., Vacus, P., David, R., Villermaux, J., and André, J. C., "A Method for the Study of Turbulent Mixing Using Fluorescence Spectroscopy," *Experiments in Fluids*, Vol. 9, 1990, pp. 137-147.
- ¹⁴Savas, Ö., and Gollahalli, S. R., "Flow Structures in Near-Nozzle Region of Gas Jet Flames," *AIAA Journal*, Vol. 24, 1986, pp. 1137-1140.
- ¹⁵Seitzman, J. M., Üngüt, A., Paul, P. H., and Hanson, R. K., "Imaging and Characterization of OH Structure in a Turbulent Nonpremixed Flame," *Twenty-Third Symposium (International) on Combustion*, Combustion Inst., Pittsburgh, PA, 1990, pp. 637-644.
- ¹⁶Clemens, N. T., and Paul, P. H., "Effects of Heat Release on the Near Field Flow Structure of Hydrogen Jet Diffusion Flames," *Combustion and Flame*, Vol. 102, 1995, pp. 271-284.
- ¹⁷Chen, L.-D., Seaba, J. P., Roquemore, W. M., and Goss, L. P., "Buoyant Diffusion Flames," *Twenty-Second Symposium (International) on Combustion*, Combustion Inst., Pittsburgh, PA, 1988, pp. 677-684.
- ¹⁸Becker, H. A., Hottel, H. C., and Williams, G. C., "The Nozzle-Fluid Concentration Field of the Round, Turbulent, Free Jet," *Journal of Fluid Mechanics*, Vol. 30, Pt. 2, 1967, pp. 285-303.
- ¹⁹Schlichting, H., *Boundary-Layer Theory*, McGraw-Hill, New York, 1979, pp. 747-750.
- ²⁰Renfro, M. W., Pack, S. D., King, G. B., and Laurendeau, N. M., "Hydroxyl Time-Series Measurements in Laminar and Moderately Turbulent Methane/Air Diffusion Flames," *Combustion and Flame*, Vol. 115, 1998, pp. 443-455.
- ²¹Becker, H. A., and Yamazaki, S., "Entrainment, Momentum Flux and Temperature in Vertical Free Turbulent Diffusion Flames," *Combustion and Flame*, Vol. 33, 1978, pp. 123-149.
- ²²Renfro, M. W., Sivathanu, Y. R., Gore, J. P., King, G. B., and Laurendeau, N. M., "Time-Series Analysis and Measurements of Intermediate Species Concentration Spectra in Turbulent Nonpremixed Flames," *Twenty-Seventh Symposium (International) on Combustion*, Combustion Inst., Pittsburgh, PA, 1998, pp. 1015-1022.

R. P. Lucht
Associate Editor